

# **Weather Corrections for a Point Source Search at the Pierre Auger Observatory**

DISSERTATION  
zur Erlangung des akademischen Grades eines  
Doktors der Naturwissenschaften

vorgelegt von  
**Diplom-Physiker Thomas Bäcker,**  
geboren am 5. Juni 1972 in Karl-Marx-Stadt,

genehmigt vom Fachbereich Physik  
der Universität Siegen

Siegen  
Juli 2010

Gutachter der Dissertation: Univ.-Prof. Dr. I. Fleck  
Univ.-Prof. Dr. M. Risse

Datum der Disputation: 9. August 2010

gedruckt auf alterungsbeständigem holz- und säurefreiem Papier

## **Abstract**

At energies up to some 100 TeV, cosmic radiation can be detected by means of particle detectors installed aboard a balloon or a satellite. At higher particle energies, the flux of the radiation drops significantly and large detection volumes are inevitable to acquire a sufficiently large amount of cosmic ray data in a short period of time. Extensive air shower experiments are exploiting the atmosphere above the actual experimental setup as a detector volume. Therefore, they are capable of recording cosmic ray data even at the highest energies. The properties of the primordial particle, however, can only be inferred from the extensive air showers, i.e. the cascades of secondary particles, that are measured by the detector setup at ground level. The performance of such experiments is thus subject to variations caused by, among other things, the instantaneous state of the atmosphere. In this thesis, a method for partly compensating the impact of these variations on the distribution of the arrival directions of cosmic rays is presented and its application to small scale anisotropy studies is investigated.

## **Zusammenfassung**

Bis zu Energien von einigen 100 TeV können Teilchendetektoren, die von Ballons oder Satelliten getragen werden, zur Erfassung kosmischer Strahlung herangezogen werden. Zu höheren Teilchenenergien hin nimmt der Strahlungsfluß stark ab und große Detektorvolumina sind notwendig, um in kurzer Zeit eine große Anzahl von kosmischen Teilchen vermessen zu können. Experimente, die ausgedehnte Luftschauber vermessen, nutzen die Atmosphäre über dem eigentlichen Experimentaufbau als ihr Detektorvolumen. Sie sind damit in der Lage, selbst bei den höchsten Energien noch Daten kosmischer Teilchen zu erfassen. Die Bestimmung der Eigenschaften der kosmischen Teilchen erfolgt hier aber über eine Messung der ausgedehnten Luftschauber, d.h. der Kaskaden von Sekundärteilchen, durch den experimentellen Aufbau am Boden. Die Funktion solcher Experimente ist daher unter anderem vom gegenwärtigen Zustand der Atmosphäre abhängig. In dieser Arbeit wird eine Methode vorgestellt, die Auswirkungen auf die Verteilung der Ankunftsrichtungen kosmischer Teilchen zu kompensieren und ihre Anwendung auf Studien kleinräumiger Anisotropie wird untersucht.



# Table of Contents

<b>1. Introduction</b>	<b>1</b>
<b>2. Ultra–High Energy Cosmic Radiation</b>	<b>3</b>
2.1. Elemental Composition of Cosmic Rays . . . . .	4
2.2. Extensive Air Showers . . . . .	5
2.3. Cosmic Ray Propagation and Particle Acceleration . . . . .	9
2.4. Astroparticle Sources . . . . .	10
2.5. Cosmic Ray Energy Spectrum . . . . .	11
2.5.1. Knee Feature . . . . .	12
2.5.2. Second Knee . . . . .	14
2.5.3. Ankle Feature . . . . .	15
2.5.4. GZK Suppression . . . . .	16
2.6. Detection Techniques . . . . .	17
<b>3. Pierre Auger Observatory</b>	<b>19</b>
3.1. Southern Observatory Site . . . . .	19
3.1.1. Surface Detector (SD) . . . . .	20
3.1.2. Fluorescence Detector . . . . .	24
3.1.3. Enhancements for the Southern Site . . . . .	27
3.2. Northern Observatory Site . . . . .	29
<b>4. Sources of Weather Data</b>	<b>31</b>
4.1. Climatic Site Characteristics . . . . .	32
4.2. Weather Stations . . . . .	32
4.3. Deviations of Weather Station Data . . . . .	35
4.3.1. Temperature Gradient . . . . .	37
4.3.2. Air Pressure Gradient . . . . .	40
4.4. Ideal Gas Approximation . . . . .	40
4.5. Temperature Information from SD Stations . . . . .	42
4.5.1. Precision of Temperature Sensors . . . . .	43
4.5.2. Deconvolution of SD Station Temperatures . . . . .	44
4.5.3. Construction of the Convolution Kernel . . . . .	45
4.5.4. Residual Temperature Uncertainty . . . . .	46
4.6. Summary . . . . .	47

<b>5. Weather Corrections</b>	<b>49</b>
5.1. Atmospheric Effects on EAS . . . . .	49
5.1.1. Sensitivity of the SD (Surface Detector) . . . . .	50
5.1.2. Variations of the Atmospheric Pressure . . . . .	51
5.1.3. Variations of the Atmospheric Density . . . . .	53
5.1.4. Impact on $S_{1000}$ . . . . .	54
5.1.5. Impact on the Event Rate . . . . .	56
5.1.6. Determination of the Parameters $\xi$ , $\alpha$ and $\beta$ . . . . .	56
5.2. Impact on Zenith Angle Distributions . . . . .	57
5.2.1. Dataset . . . . .	58
5.2.2. Lowest Energy Cut . . . . .	58
5.2.3. Selection of a Subsample Cut Parameter . . . . .	58
5.2.4. $\chi^2$ Maximisation . . . . .	59
5.2.5. Ansatz for a Compensation . . . . .	61
5.2.6. Parameter Estimation for $\mathbf{p_E}$ . . . . .	63
5.2.7. Estimation of the Parameter Uncertainty . . . . .	63
5.2.8. Results . . . . .	64
5.2.9. Side Effects of the Compensation . . . . .	65
5.3. Summary . . . . .	67
<b>6. Application to the Search for Point Sources</b>	<b>71</b>
6.1. Galactic Centre . . . . .	71
6.2. Field of View . . . . .	72
6.3. On–Off Method . . . . .	73
6.4. Aperture Weighting . . . . .	74
6.5. Application to Isotropic Datasets . . . . .	76
6.5.1. Generating Isotropic Datasets . . . . .	76
6.5.2. Li–Ma Significance of Isotropic Datasets . . . . .	77
6.5.3. Li–Ma Significance of Isotropic Datasets, Corrections Applied . . . . .	77
6.6. Application to Anisotropic Datasets . . . . .	78
6.7. Application to Data Taken by the SD Array . . . . .	78
6.8. Summary . . . . .	81
<b>7. Summary</b>	<b>85</b>
<b>A. GZK Horizon for Protons</b>	<b>87</b>
A.1. Proton Tracking . . . . .	87
A.2. Results . . . . .	89
<b>B. Weather Databases</b>	<b>91</b>
B.1. Balloon Data & Monthly Layer Profiles . . . . .	91
B.2. Weather Station Data . . . . .	92

B.3. Surface Detector Monitoring Data . . . . .	92
<b>C. Data from Weather Stations</b>	<b>93</b>
<b>D. Zenith Angle Uncertainties</b>	<b>103</b>
<b>E. Zenith Angle Distributions</b>	<b>115</b>
<b>F. Li–Ma Significance</b>	<b>121</b>
<b>List of Figures</b>	<b>123</b>
<b>List of Tables</b>	<b>125</b>
<b>List of Acronyms</b>	<b>127</b>
<b>Bibliography</b>	<b>131</b>





# Chapter 1

## Introduction

The Pierre Auger Observatory is reliably taking data since January 2004. In 2008, its construction was finished. It is the largest extensive air shower experiment so far, covering an area of  $3000\text{km}^2$  in all.

The Pierre Auger Observatory has been designed to explore cosmic radiation in the EeV regime. Although its surface detector array is fully efficient at a primary particle energy in excess of  $3\text{EeV}$ , only about 3% of all air shower events recorded by the detector meet this energy requirement.

The discovery of a point source candidate relies on the acquisition of a large number of events to overcome the statistical fluctuations of a small excess signal and a noisy background.

At energies lower than the threshold energy for fully efficient detection, however, the trigger efficiency is subject to variations of the detector setup at ground level as well as to variations of the atmosphere above the experiment, which is used as a detector volume. To be able to exploit the air shower events at primary cosmic ray energies below  $3\text{EeV}$ , these variations need to be estimated and compensated for. The thesis at hand aims at contributing to this effort.

After a brief overview of the theory of ultra-high energy cosmic radiation in Chap. 2, the Pierre Auger Observatory is briefly described in Chap. 3. A survey of the climatic site characteristics and weather stations of the southern part of the Pierre Auger Observatory is presented in Chap. 4, followed by Chap. 5 dealing with procedures for the compensation of weather related variations of the detector properties. In Chap. 6, the procedures are applied to the search for point sources. Finally, the results of the analysis are summarised in Chap. 7.



# Chapter 2

## Ultra–High Energy Cosmic Radiation

The term *cosmic radiation* (or *cosmic rays*) usually refers to those charged particles, which are constantly emitted by sites in our galaxy or somewhere in the extragalactic space, or which originate from interactions of their emissions with the interstellar matter. They include stable nuclei, from protons (the nucleus of hydrogen) to iron, as well as light elementary particles like positrons and electrons. In interactions of these particles with nuclei of the Earth’s atmosphere, extensive air showers are initiated, eventually giving rise to cascades of secondary particles.

In the sense that they as well can be considered messengers from sources and interaction processes in our galaxy and beyond, neutrinos and photons, although uncharged, could also be called cosmic ray particles. Photons may even initiate mainly electromagnetic cascades of secondary particles in the upper layers of the Earth’s atmosphere just in the same way as electrons/positrons do. However, these particle types are commonly not termed as cosmic ray particles.

Although this chapter also aims at providing an overview on cosmic radiation in general, it will nevertheless put the focus on ultra–high energy cosmic rays (UHECR) as the analysis presented in the thesis at hand is using data recorded by the **Pierre Auger Observatory**, which is designed to take data representing cosmic rays primarily in the EeV range.

The first evidence for the existence of cosmic rays was found by Viktor Hess in 1912 during balloon flights when he noticed that the level of radiation detected by an electroscope increased with the altitude of the balloon after it at first had dropped as the balloon started to ascend from the Earth’s surface [Hes12]. Viktor Hess concluded that the increase of radiation at higher altitudes must be due to radiation coming in from outer space, whereas the radiation at ground is mainly emitted by the Earth itself.

Long before man–made accelerator facilities were invented to study particle interactions at the highest energies, systematic studies of cosmic rays led to important discoveries in the field of elementary particle physics. Particles like e.g. the positron, the muon and the pion (“Yukawa’s particle”) were first found this way. Still, in spite of the technological

progress achieved in accelerator physics throughout the years, cosmic radiation continues to be the only particle source capable of providing particles at energies up to some 100 EeV as they have been discovered already as early as in the year 1963 [Lin63a]. Hitherto, however, no source candidate has clearly been identified as being powerful enough to expel particles at such enormous, macroscopic energies; the type of the corresponding particles could not yet be determined either.

Other fundamental questions associated with astroparticle physics remain unanswered as well. For instance, our knowledge of the elemental composition of cosmic radiation at energies exceeding some 100 TeV, where direct detection methods fail to provide sufficient statistics, is limited by the accuracy of extrapolations for particle interactions far beyond those centre of mass energies being directly accessible to accelerator experiments [ICR07]. Another topic, which is still lacking a decisive result, concerns the mechanisms enabling the cosmic ray particles to enter the UHECR regime in terms of their momentum, either directly through processes in the source itself or by some site interacting with the incoming primordial particles, thereby feeding them with additional energy.

## 2.1. Elemental Composition of Cosmic Rays

Only up to some 100 TeV, the chemical composition of the cosmic radiation is well known. In this energy range, direct measurements using balloon-borne or satellite-borne instruments are available. At higher energies, only extensive air shower experiments are capable of overcoming the low cosmic ray flux, since they can be scaled in size and running time. In this case, composition data results from a reconstruction procedure. However, the precision of this reconstruction is usually depending on interaction models, which become unreliable as the energy increases.

In Fig. 2.1, the composition according to current experimental results is shown; it is compared to the elemental abundances in the solar system. Largely, both datasets are in good agreement, which suggests that nucleosynthesis is the predominant production mechanism in sources of cosmic radiation as it is in the sun. However, Fig. 2.1 also shows some disagreement regarding several elemental groups.

Hydrogen and helium are less frequently found in cosmic radiation than in the solar system. The energy required for stripping the valence electrons off these atoms is relatively high. Since most acceleration scenarios only act upon charged particles, a considerable fraction of the hydrogen and helium atoms is not undergoing any acceleration process and, therefore, it does not show up in the elemental composition of cosmic rays.

Several elements with a small nuclear charge number  $Z$  (specifically B, Be, Li) are much more abundant in the cosmic radiation than in our solar system. Only a small fraction of the particles produced by nucleosynthesis belongs to this group of elements. The excessive abundance in cosmic rays results from nuclear spallation caused by collisions of nuclei in the CNO element group with interstellar matter. Similarly, the spallation of nuclei in the iron group leads to the production of heavy nuclei (Cr, Mn, Sc, Ti, V),

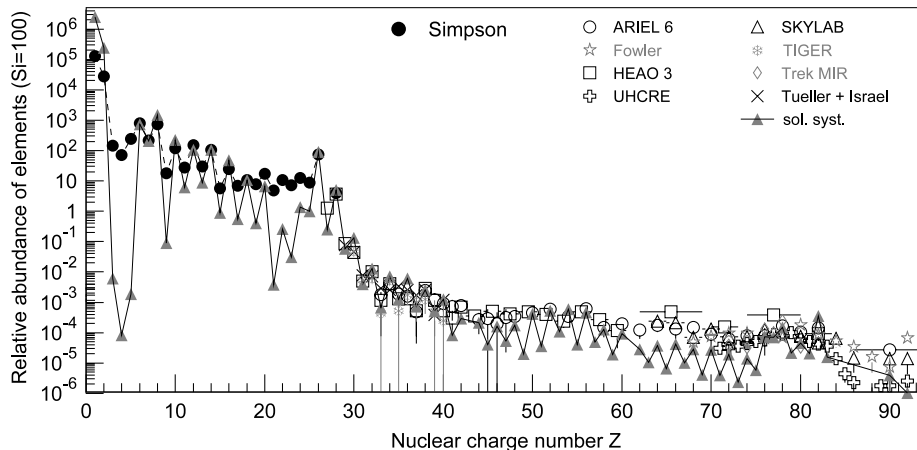


**Figure 2.1.:** Chemical composition of the cosmic radiation (taken from [Blü09]). The abundance is shown versus the atomic number  $Z$ , relative to the abundance of silicon ( $Z = 14$ , corresponding to a value of 100 on the ordinate); data for  $Z \leq 28$  according to [Sim83]; for a list of references regarding abundances beyond  $Z = 28$  see the references listed in [Blü09]. In comparison to the results from cosmic rays, the elemental abundance in the solar system is shown [Lod03].

thereby enriching the cosmic ray composition for higher values of the atomic number  $Z$ .

## 2.2. Extensive Air Showers

Astroparticle physics experiments, which make use of the atmosphere as a calorimeter volume [Wie09], are actually based on the work of Pierre Auger, who in 1939 discovered that in many cases particles were almost simultaneously detected by several detector stations at different locations on the ground [Aug39]. The conclusion was that cascades of secondary particles, initiated by primary cosmic ray particles, were hitting the detector stations. These particle cascades are called *extensive air showers*, they emerge from inelastic scattering of the primary particle in the upper atmosphere and, subsequently, of the secondary particles in lower atmosphere layers.

At extreme energies, i.e. energies exceeding some 100 TeV, earthbound extensive air shower experiments are the only viable experimental method for acquiring a large amount of cosmic ray data despite the low flux of the primary cosmic radiation; they are easily scalable in size and they can be operated during extended periods of time. At lower energies, i.e. up to some TeV, direct detection of primary cosmic particles is feasible due to the high flux; here, the type of the incoming particles can be identified directly, whereas this cannot be done in a direct manner using extensive air shower experiments. The direct detection methods make use of particle detectors, installed onboard a balloon or a satellite. Since their sizes and payloads are limited, they run out of statistics for energies in the PeV regime and beyond [Gru05].

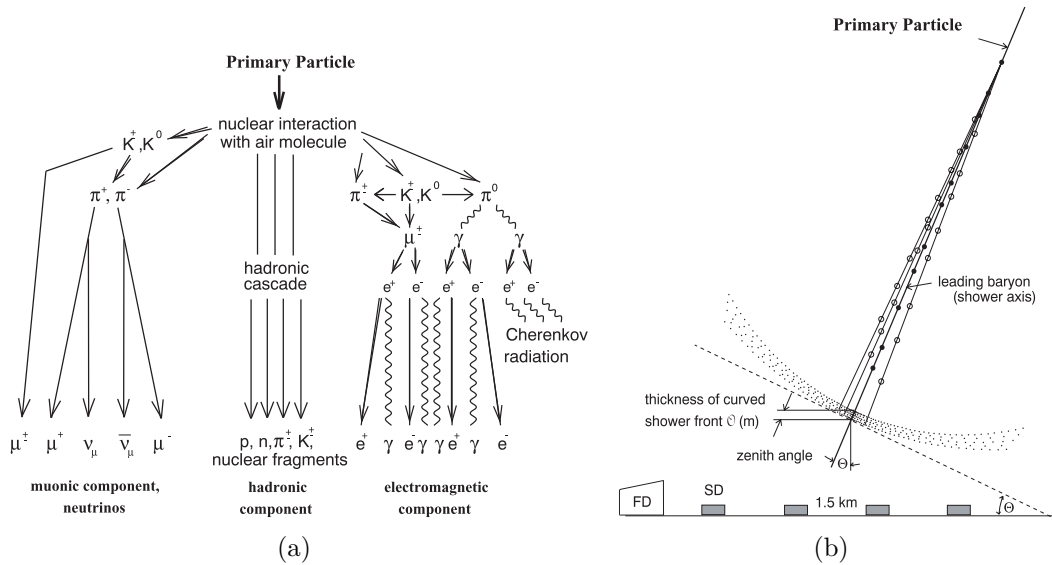


**Figure 2.2.:** In (a), the main processes taking place in extensive air showers are denoted. Specifically, the muonic, the hadron and the neutrino component as well as the electromagnetic component are indicated. In (b), the profile of a typical air shower is shown; the shower axis and the shower front are sketched in the figure. Taken from [Kei03].

An extensive air shower is initiated when the primary cosmic ray particle for the first time interacts with a nucleus of the air. The probability for this interaction depends on the inelastic cross-section for the corresponding process, which in turn varies with the energy of the primary particle. For a given atmospheric density, the interaction probability defines the mean free path length that the primary particle can travel in the atmosphere without initiating an interaction. Thus, the height above ground of the first interaction is distributed according to the underlying interaction probability distribution for the particular process.

Since not only the primary particle interaction initiates a particle cascade, but the same can happen in interactions of the secondary particles with atoms of the air, an extensive air shower is actually a superposition of the primary and secondary cascades. The cascades are implying particle production processes as well as particle decays. Many different types of particles are involved in the evolution of an air shower (see Fig. 2.2 for an illustration), most of which can be subsumed in three categories:

### Hadron component

Although only a small fraction of the particles, that are forming an extensive air shower, are hadrons (around 1%), their involvement is in fact crucial as they can feed the other shower components. The first generation of secondary hadrons is produced in a strong interaction process of the primary particle with a nucleus of the air. Further generations of secondary particles may be created in subsequent interactions with nuclei of the

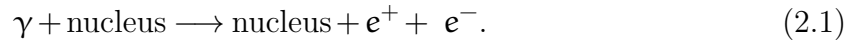
atmosphere, provided the mean lifetime of the particle is long enough and its energy still suffices. Thus, a hadron cascade evolves as the extensive air shower propagates through the atmosphere. Eventually, the number of hadrons reaches a maximum number, then it decreases again, because it becomes more likely for the particles to decay than to interact again as the energy per particle reduces. The probability for a hadronic primary cosmic ray particle to reach ground level is very small since for vertical particle incidence the atmosphere corresponds to 11 hadronic interactions.

Most of the secondary hadrons are charged and neutral pions; kaons, protons, and neutrons contribute a smaller fraction. On average, secondary hadrons only carry a transverse momentum of about 400 MeV/c, which is negligible compared to their overall momentum except for primary particle energies in the GeV regime and below. Thus, the hadron component forms a narrow shower core with a maximum distance from the shower axis, the extension of the trajectory of the primary cosmic ray particle (see Fig. 2.2(b) for a schematic view), of about 20 m.

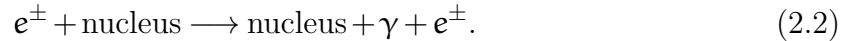
Decays of secondary hadrons also supply the other shower components with particles. When neutral pions decay into a pair of photons, they feed the electromagnetic shower component. Similarly, the muon component obtains particles from decays of charged mesons.

### Electromagnetic component

A photon originating from a decay in the hadron component, may interact with an air nuclei to produce pairs of electrons and positrons:



In bremsstrahlung processes, these electrons/positrons may, in turn, cause photons to be produced:



Photon production in bremsstrahlung processes and electron/positron pair production are taking place alternately, thus perpetuating the electromagnetic cascade. Since neutral pions are produced all along the path of the hadronic cascades, the number of particles in the electromagnetic component actually results from a superposition of the subcascades initiated by the individual neutral pions. In this way, the electromagnetic cascade rapidly becomes the most predominant one with respect to the number of particles involved. For a photon-induced electromagnetic shower, the total number of particles (defining the longitudinal profile) can be approximated [Gre56] by

$$N_{e/\gamma}(E_0, t) = \sqrt{\frac{1}{10\beta_0}} \cdot e^{(2-3\ln s)\frac{t}{2}}, \quad (2.3)$$

where

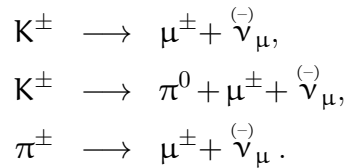
$$t = \frac{X}{X_0}, \quad \beta_0 = \ln \frac{E_0}{E_{\text{crit}}}, \quad s = \frac{3t}{t + 2\beta_0}.$$

Here,  $E_0$  is the energy of the photon initiating the shower,  $t$  the atmospheric depth in units of the *radiation length*  $X_0$  (with  $X_0 = 37.1 \text{ g/cm}^2$  in air). The *age parameter*  $s$  describes the longitudinal shower development. For  $s = 0$  the shower has just been created, it reaches its maximum particle content for  $s = 1$ , and for  $s > 1$  the shower dies out again, i.e. the number of particles decreases. The *critical energy*  $E_{\text{crit}}$  defines the point where the energy loss due to ionisation equals the loss caused by bremsstrahlung processes; for electromagnetic cascades in air, it averages to about 84.2 MeV.

The lateral spread of the electromagnetic component results from Coulomb scattering, it can be described by the *NKG function* [Gre56, Kam58]. Strictly speaking, this function only provides a valid description for the lateral spread for a purely  $e/\gamma$ -induced shower. In hadron-induced extensive air showers, however, the electromagnetic component is actually a superposition of air showers originating from the decay of neutral pions into photons. Nevertheless, it is still possible to estimate the number of  $e/\gamma$  particles even in this case using the NKG function; this is possible by adjusting its parameters appropriately.

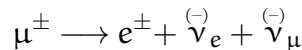
### Muon component

In a typical hadron-induced extensive air shower, muons comprise about 5% of all particles, they are mainly produced in decays of secondary mesons, e.g. as follows:



High in the atmosphere, the density of the air is still low. Therefore, the mean free path length for the hadron interaction is large as compared to the mean free decay length of the mesons. As a consequence, most mesons produced as secondary particles are decaying in the early stage of the hadron shower development, thereby feeding the muonic air shower component. For that reason, the production of muons basically takes place in the upper atmosphere, only a small fraction stems from decays at later stages of the hadronic cascade.

For low energy muons, decaying via



is not improbable, since in this case the muon lifetime (2.2  $\mu\text{s}$  at rest [Ams08]) is nearly unaffected by relativistic time dilatation. Hence, these muons might also end up feeding the electromagnetic air shower component.

The lateral spread in the electromagnetic component is by far larger than for the muon component. The contributions for the latter with respect to multiple Coulomb scattering and bremsstrahlung scale proportional to  $m_e^2/m_\mu^2$ . Thus, the lateral development of the



muonic air shower component is governed by the transverse momenta of the mesons producing the muons. Furthermore, muons are not affected by strong interactions and only loose minor amounts of energy by ionisation. Their lateral distribution can be approximated by semi-empirical formulas [Lin63b, Arm74]. Since muons nearly do not suffer any deflection, their trajectories are pointing back to their places of origin.

Unlike the electromagnetic component, the muon cascades do not exhibit a pronounced maximum of its longitudinal profile. The number of particles does not grow rapidly, and on the other hand, only a negligible percentage of the muons disappears in decays after reaching the maximum. Therefore, the number of muons remains nearly constant until they reach ground level. Because it only weakly depends on the type of primary particle, but rather strongly on its energy, the maximum number of muons can also be considered a reliable estimator of the primary particle energy.

## 2.3. Cosmic Ray Propagation and Particle Acceleration

On their way from the production sites to the Earth, the charged cosmic radiation undergoes deflections by various regular and irregular galactic magnetic fields. Thus, only the trajectories of particles at the highest rigidities will still point back to their place of origin, whereas at lower rigidities the directional information is completely lost. The fact, that cosmic radiation is found to be largely isotropic, supports the assumption of a diffusive propagation of the cosmic rays. Furthermore, the energy of the primordial particles changes in collisions with interstellar matter, or due to ionisation and particle decay. The probability for a particle to escape from its confinement within the galactic disk is also depending on the energy. The change of the spectral index of the primordial cosmic radiation ( $\gamma \approx 2.0$ ) to the spectral index measured by experiments on Earth ( $\gamma \gtrsim 2.7$ ) is an immediate consequence of these effects.

Basically, there are three established categories of models suggesting possible acceleration scenarios. From a valid model, it has to be possible to infer the general characteristics of cosmic radiation, e.g. the power law shape of the energy spectrum or the energy density observed. In the following, the categories of models are briefly discussed.

### Top-down models

In these models, the origin of ultra-high energy cosmic radiation is attributed to some yet unknown mechanism [Sig03], capable of providing tremendous energies without the need for prior acceleration. In this sense, exotic ultra-heavy particles are commonly considered a possible explanation. Here, the decay of such a particle results in the production of UHECR particles. In general, top-down models predict cosmic radiation at energies in excess of  $10 \cdot 10^{15}$  eV.

### Direct (non-stochastic) acceleration

Here, an inevitable requirement is the presence of strong magnetic and electric fields. Active Galactic Nuclei (AGN) are promising sites, that may fulfill these preconditions

in the relativistic particle jets expelled by them [Rac93]. Another environment, that may be compatible, can be found in the polar caps of rapidly spinning pulsars [Che86]. Interactions of low energy cosmic radiation with highly relativistic particle jets could also serve as a possible explanation. Supernovae may be capable of supplying a stream of matter to form jets consistent with this hypothesis [Dar08].

### Stochastic acceleration

The fundamental concept, the stochastic acceleration is based upon, is called *first-order Fermi acceleration* [Fer49]. Rather than in a one-shot process, particles attain their final energy in this model in numerous interactions, each of which causes only a small rise in energy. The actual energy increase takes place in shock waves by diffusive acceleration. At the shock front, the compression of the medium creates two different magnetic field topologies and diffusive scattering of the particles at either side leads to multiple cycles of the acceleration process. In each cycle, an energy increase proportional to the speed of the shock front can occur. The total gain depends on the number of acceleration cycles, which in turn is limited by the lifetime of the shock wave. An intrinsic property of the first-order Fermi acceleration lies in its prediction of a primordial energy spectrum with a spectral index of  $\gamma \approx 2.0$ , nearly independent of the actual shape of the shock front. A more in-depth discussion of the diffusive shock acceleration scenario can be found in [Dru83].

Shock fronts, as they are essential for this type of acceleration scenario, are likely to originate from supernova explosions. On average, three of those explosions take place in the Milky Way in each century, releasing a power of about  $3 \cdot 10^{35}$  J/s. Provided the efficiency for the energy conversion into cosmic radiation reaches a level of a few percent, the energy density of cosmic rays observed ( $\approx 1 \text{ eV/cm}^3$ ) could be caused by this mechanism alone. Other sources of shock fronts may be found in termination shocks of stellar or galactic winds. The energies, that particles of cosmic radiation can attain in interactions with shock fronts coming from sites of these types, are expected to be limited to some  $10^{16}$  eV.

## 2.4. Astroparticle Sources

As can be seen from Fig. 2.3, only a few astronomical sites are satisfying the preconditions for the acceleration up to the highest energies ever measured by extensive air shower experiments. Either large magnetic field strengths or very extensive acceleration regions are necessary. As of writing this thesis, no astronomical object has positively been identified as being a source of cosmic radiation in the EeV regime. In the following, the major characteristics of some of those candidate sites are listed:

### Galactic clusters

In [Ptu09], galactic clusters are considered a promising site for the acceleration of cosmic ray particles up to energies in the order of magnitude of 100 EeV. Here, the typical

magnetic field strength of  $\approx 5 \mu\text{G}$ , in combination with the size of such a region of  $\approx 1.5 \cdot 10^6 \text{ly}$ , makes the confinement of UHECR particles within the cluster possible. However, since cosmic rays in the galaxy cluster are travelling over long distances, their interaction probability with photons of the cosmic microwave background radiation must not be neglected. Thus, the maximum energy for particles eventually originating from such a kind of source does not exceed some 10 EeV.

### Hot spots of radio galaxies

FR-II radio galaxies come into existence by collisions of relativistic particle jets, emitted by black holes, with interstellar matter, thereby creating radio lobes and localized regions of intense synchrotron radiation (sometimes called *hot spots*); see e.g. [Rac93] for a detailed discussion. Typically, the size of the active region is in the order of 3 ly in this case, whereas the confining magnetic field amounts to about  $300 \mu\text{G}$ , limiting the maximum attainable energy to some 100 EeV.

### Gamma ray bursts (GRBs)

The cause for the emission of gamma ray bursts may lie in the merging of neutron stars or black holes. It may as well be connected to collapses of massive stars. The  $\gamma$  rays (at energies in the GeV regime) are produced by relativistic electrons as synchrotron radiation or via inverse Compton scattering processes. Considering the energy release of typical GRBs of up to  $10^{46} \text{J}$  within a few seconds, the luminosity probably suffices for light nuclei and electrons to attain energies of up to 10 EeV in subsequent acceleration processes (see e.g. [Mil07]). However, because objects of this kind are relatively rare and most of them are far apart, gamma ray bursts are unlikely to contribute a considerable fraction of the cosmic rays detected.

### Neutron stars, pulsars

For cosmic ray emissions from compact rotating sources, like e.g. neutron stars or pulsars, the maximum particle energy depends on the radius of the object, its angular velocity, and the magnetic field strength at the surface. For instance, the Crab Pulsar, the central neutron star of the Crab Nebula, is expected to reach an estimated maximum energy in the order of magnitude of a few EeV (see e.g. [Sch28]).

### Active galactic nuclei (AGNs)

As already mentioned in Section 2.3, AGNs are commonly agreed upon candidates for the place of origin of ultra-high energy cosmic rays. Magnetic field strengths of typically 0.5 mT enable active galactic nuclei to confine e.g. protons at energies of up to some 100 EeV within a relatively compact area (about  $5 \cdot 10^{-2} \text{ly}$  in diameter).

## 2.5. Cosmic Ray Energy Spectrum

The integrated flux of particles arriving at the outer layer of the atmosphere amounts to around  $1000 \text{s}^{-1} \text{sr}^{-1} \text{m}^{-2}$  [Gai91]. It is mainly caused by protons in the GeV regime ( $\approx 85\%$ ),

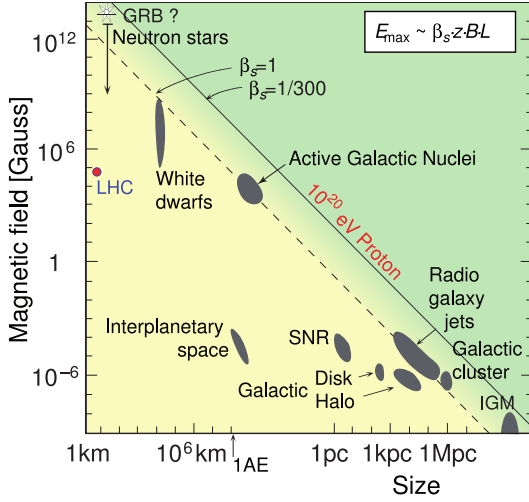


**Figure 2.3.:** Hillas plot (taken from the preprint of [Blü09]). Astronomical objects are arranged according to their typical magnetic field strengths and sizes. Sites situated below the diagonal lines are not capable of accelerating the primordial particles to the corresponding maximum energy. For comparison, the LHC has also been incorporated into the diagram.

$\alpha$  particles comprise another 12%, heavier nuclei about 1%; the electron component contributes about 2% of the particles. At PeV energies, the flux reduces to about  $1 \text{ yr}^{-1} \text{ sr}^{-1} \text{ m}^{-2}$  and, finally, to only  $1 \text{ yr}^{-1} \text{ sr}^{-1} \text{ km}^{-2}$  at some  $10^{20} \text{ eV}$ . The energy range of the incoming cosmic ray particles covers about eleven orders of magnitude, whereas the flux drops by about three orders of magnitude per energy decade, thus even spanning thirty orders of magnitude in total. The differential flux can be approximated by a power law

$$\frac{d\Phi}{dE} \propto E^{-\gamma}, \quad (2.4)$$

where the spectral index  $\gamma$ , as can be seen from Fig. 2.4, is piecewise approximately constant [Blü09, Hau04]. Up to an energy of about  $E_{\text{knee}} \approx 4 \cdot 10^{15} \text{ eV}$ , the all-particle flux of the primary cosmic rays drops at a rate corresponding to  $\gamma \approx 2.7$ , then the spectral index rises by a value of  $\approx 0.4$ . The transition point at  $E \approx E_{\text{knee}}$  is called the *knee* of the spectrum. A further steepening of the energy spectrum ( $\gamma \approx 3.3$ ) seems to occur at the *second knee*, at about  $E = 4 \cdot 10^{17} \text{ eV}$ . At about  $E_{\text{ankle}} \approx 4 \cdot 10^{18} \text{ eV}$  the spectrum flattens again, the spectral index returns to a value of  $\gamma \approx 2.7$ ; this feature is often referred to as the *ankle* of the energy spectrum of cosmic radiation. Finally, a suppression of the cosmic ray particle flux is expected to occur for  $E \gtrsim 6 \cdot 10^{19} \text{ eV}$  due to the so-called *GZK suppression*. The major spectral features mentioned above are still subject to intense scientific research, they will briefly be treated of in the following sections.

### 2.5.1. Knee Feature

There are two main classes of models attempting to provide explanations for the knee feature found in the energy spectrum as it is recorded by extensive air shower experiments.

Theories, in which the shower development in the atmosphere volume is inducing the sudden change of the spectral index at  $E_{\text{knee}}$ , postulate an, as of yet unknown, interaction.

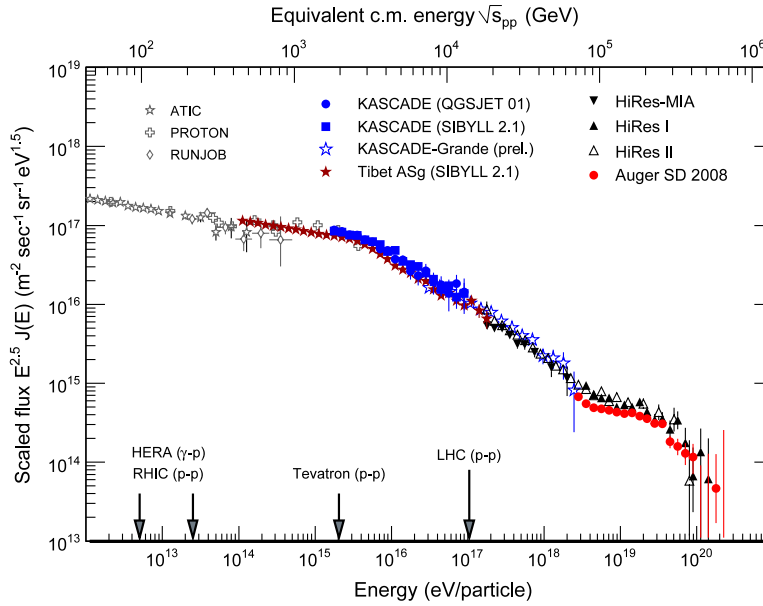


**Figure 2.4.:** Energy spectrum for all particles as a result of direct flux measurements (by ATIC [ICR03], PROTON [Gri70] and RUNJOB [Der05]) and extensive air shower measurements by earthbound detectors (KASCADE [Ant05], KASCADE-Grande [AV09] (preliminary), Tibet AS $\gamma$  [Ame08], HiRes-MIA [AZ01], HiRes I and HiRes II [Abb08] and the Pierre Auger Observatory [Abr08]), respectively. The flux has been multiplied by the reconstructed energy  $E_0$  to the power of 2.5 to unveil the features of the spectrum despite the large ranges covered by both the energy  $E_0$  and the flux  $\Phi$ . The lower abscissa corresponds to the energy of a cosmic ray particle. The values for collider experiments, marked by arrows, indicate the equivalent energy of a cosmic ray particle required to reach the corresponding centre of mass energy of these experiments (upper abscissa). Taken from [Blü09], see there for more references.

The momentum of incoming cosmic ray particles is then partly transferred to some exotic secondary EAS component [Kaz01] if the primary energy is exceeding a threshold energy, which is in the order of magnitude of  $E_{\text{knee}}$ . If this secondary air shower component does not show up in the signals detected by the experiments, the air shower reconstruction procedure consequently underestimates the primary energy and cosmic ray flux in this case. In this way, the knee feature is erroneously induced as part of the detection process, whereas the primordial spectrum does not exhibit this feature.

Recent results from air shower experiments suggest that the knee feature is caused by a reduced abundance of light nuclei in the cosmic radiation [Ant05, Kam04]. Theories which attribute the knee feature of the spectrum to actually intrinsic properties of the cosmic rays can be subsumed under the second class of models. This class includes the following proposed scenarios:

### Limited confinement in the accelerating region

The maximum particle energy that can be reached in the acceleration region is limited by its capability to confine the matter to be accelerated. In the presence of magnetic fields, which are an inevitable prerequisite for the particle acceleration in diffusive shock fronts, the Larmor radii  $R_L$  of particles are increasing with the reciprocal of the charge  $Z$  of the particle, i.e.  $R_L \propto 1/Z$ . Since for smaller Larmor radii a particle will cross the shock front more often than for larger radii, and as the gain in energy is depending on the number of crossings, the mean energy attainable in a particular acceleration region is limited by the nuclear charge of the particle to be accelerated. This dependence on the charge  $Z$  leads to a depletion of light constituents of the cosmic radiation. Thus, the position of the knee with respect to the primary particle energy is varying with the type of the particle, i.e. its charge. This scenario predicts sources in our galaxy and maximum particle energies in the PeV regime [Ber99, Sta93, Kob02].

### Limited confinement in the propagation area

Whilst a charged particle is travelling through the galaxy, there is a certain probability that it will escape from it. The galactic magnetic field, being a superposition of a regular field and a random and irregular component, confines the particles on their way through space. However, the random field component causes a drift of the primary cosmic rays, which is proportional to the energy of the particle and to the reciprocal of its charge, i.e.  $\propto E/Z$ . For energies exceeding some 3 PeV, the probability for escaping the confinement rapidly increases, leading to a depletion of light components (small nuclear charge  $Z$ ). Hence, the position of the knee is predicted to show a dependence on the charge of the particle according to this scenario [Can02, Ptu93].

### Local single source

Here, the featureless cosmic background radiation is superimposed by the primordial cosmic radiation emitted by a local and relatively young supernova remnant [Er197]. The particles which are contributed by the supernova remnant are accelerated by the shock waves expelled by it. Therefore, the knee feature in the energy spectrum measured by the experiments is actually due to the maximum energy attainable by the CNO group in the acceleration process.

## 2.5.2. Second Knee

A phenomenological model, the *poly-gonato model*, is modeling the overall cosmic ray flux as a superposition of the flux components for each single type of constituent. The flux contributions of heavier nuclei start to decrease at higher energies compared to those of light nuclei [Hör03]. In this context, the change of the spectral index at 0.4 EeV corresponds to the point where the heaviest stable nuclei do no longer significantly contribute to the overall flux, whereas the (first) knee would be associated with the fading flux of the lightest elements. This model seems to describe the data well; for the

time being the chemical composition is not well known at the highest energies, though, and more data in this regime is required for a final conclusion.

Other explanations rely on exotic particle interactions. For instance, the second knee may be caused by interactions with relic particles as they are predicted by the big bang models. Provided electron neutrinos are massive particles with a rest mass exceeding  $0.4\text{eV}/c^2$ , the kink in the energy spectrum around  $0.4\text{EeV}$  could be due to interactions of primordial  $\alpha$  particles with relic background neutrinos [Wig00]. The dissociation process may take place according to:



The primary particle energy required for dissociating  $\alpha$  particles in this manner amounts to  $\approx 0.3\text{EeV}$ , which is in good agreement with the spectral feature observed.

A similar process may also provide an explanation for the knee feature of the energy spectrum of cosmic radiation (in addition to the mechanisms discussed in Section 2.5.1). In this case, instead of primordial  $\alpha$  particles, protons may interact with relic background neutrinos according to  $\text{p} + \bar{\nu}_e \rightarrow \text{n} + e^+$ . In both cases, the destruction process causes the steepening in the respective part of the spectrum.

### 2.5.3. Ankle Feature

Since no site in the Milky Way is known to be powerful enough to accelerate particles up to energies of  $4\text{EeV}$  and beyond, and yet to confine them sufficiently, it stands to reason that the production and acceleration takes place in extragalactic sites. At sufficiently high energies, their emissions may predominate the cosmic ray flux measured in extensive air shower experiments in spite of their sparse population. The spectrum of these sources, however, may be considerably harder, thereby marking the transition from a galactic iron-enriched composition to an extragalactic proton predomination. Here, the transition is causing the ankle kink in the overall cosmic ray all-particle energy spectrum as it is observed in this energy regime (see e.g. [Ste99]).

Another explanation for the ankle feature, the *dip model*, postulates the transition from galactic to extragalactic origin already at  $\approx 1\text{EeV}$  [Ber07]. On its way to the extensive air shower detector, extragalactic cosmic radiation then suffers energy losses due to electron/positron pair productions in interactions with intergalactic photons of the cosmic microwave background radiation:



According to this model, the pair production dip causes the flattening of the spectrum, it takes effect in the energy range  $1\text{EeV} \lesssim E \lesssim 40\text{EeV}$ .

### 2.5.4. GZK Suppression

Independently of each other, Greisen [Gre66] and Zatsepin & Kuz'min [Zat66] predicted already in 1966, that the cosmic ray flux is expected to be suppressed at the highest energies, i.e. for  $E_{\text{GZK}} \gtrsim 60 \text{ EeV}$ . This so-called *GZK suppression* (or *GZK cutoff*) is the result of interactions of protons (or heavier nuclei) of the cosmic radiation with photons of the cosmic microwave background (CMB) radiation field. If the energy of an incoming cosmic ray particle is higher than  $E_{\text{GZK}}$ , then the energy in the centre-of-mass system of the photon and the primary particle suffices for photo-pion production in processes like



via an intermediate resonance state ( $\Delta(1232)^+$ ), eventually leading to the flux suppression for particles covering a distance in the order of magnitude of 100 Mpc. In Fig. 2.5, the energy of a cosmic ray proton, as it propagates through the CMB radiation field, is plotted. The prediction of a GZK suppression has recently been confirmed by the **Pierre Auger Collaboration** [Abr08] as well as by **HiRes** [Abb08] and **Fly's Eye** [Bir94]. However, the data taken by **AGASA** seem to contradict these findings since the number of extensive air shower events recorded in the energy range above  $E_{\text{GZK}}$  is not compatible with the prediction of a flux suppression according to the GZK mechanism. Nevertheless, the systematic uncertainties associated with the energy reconstruction by **AGASA** suggest that the contradiction is merely due to experimental effects, not due to the properties of the cosmic ray spectrum alone (see [Blü09] for a list of references).

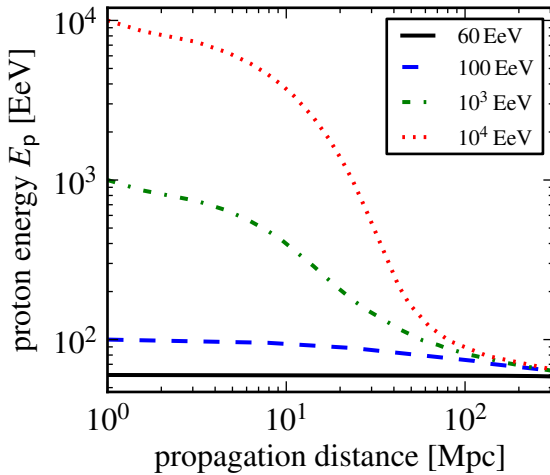


**Figure 2.5.:** GZK horizon for protons. For different values of the injection energy, the proton energy is plotted as a function of the propagation distance covered; see App. A for details. At distances larger than the GZK horizon ( $D_{\text{GZK}} \approx 100 \text{ Mpc}$ ) and injection energies  $E_p^0 \gg 100 \text{ EeV}$ , a large percentage of the initial energy is dissipated in interactions with photons of the CMB, e.g. approximately 99% for  $E_p^0$  in the order of magnitude of  $10^4 \text{ EeV}$  (cf. Fig. A.1).



## 2.6. Detection Techniques

Several experimental techniques are available to measure extensive air shower observables and to reconstruct cosmic ray properties, that are not accessible otherwise, by indirect means. The detection methods differ with respect to the air shower properties exploited to gather the relevant information [Blü09]. A brief overview of various detector types will be given in this section.

### Array detectors

Scintillation detectors, arranged as an array of stations, can be used to detect charged particles (mainly the  $e/\gamma$  component). In a similar way, arrays of water Čerenkov detector stations are suitable for detecting secondary particles. Since the latter type provides a thicker detection medium, its efficiency with respect to inclined air showers is noticeably higher than for the scintillator equipped one.

In both cases, combining the data obtained from the various detector stations, it renders possible the sampling of the lateral distribution. From this information, the core position of the extensive air shower can be deduced as well as the estimated number of particles contained in it. In addition, by determining the arrival times at the stations, the arrival direction of the primary cosmic ray particle can be estimated, provided the time resolution is high as compared to the flight time skew. Installing detector stations only sparsely is usually sufficient because of the large number of secondary particles, especially at the highest primary energies. Typically, a coverage of the total area in the order of magnitude of 1% or less suffices [Blü09] for experiments operating in the PEV regime; at higher energies, even smaller percentages allow proper sampling of the secondary particles.

### Čerenkov detectors

Most of the charged particles travelling through the Earth's atmosphere do so at relativistic velocities. About 30% of them are emitting Čerenkov radiation in their forward direction, sharply focused with an aperture angle of  $1.3^\circ$  (at sea level). Since most of the charged particles in extensive air showers are actually electrons, and since their Čerenkov threshold amounts to about 21 MeV at sea level, they contribute the largest fraction of the light.

Čerenkov detectors (as well as fluorescence telescopes) are reliant on a sufficiently dark background and a clear sky to operate properly. Therefore, their duty cycle is restricted to 10% due to the moon phases and weather conditions. In general, there are two types of Čerenkov detectors (see [Blü09] for a review). *Integrating detector setups* are usually consisting of an array of stations. As a whole, they are sampling the lateral distribution of Čerenkov photons in the field of view of the array. Both the energy and  $X_{\max}$ , the atmospheric depth of the shower maximum, can be determined from its measurements of the light distribution. On the other hand, *imaging Čerenkov detectors* are analysing the image (in terms of the Čerenkov light in its focal plane) caused by cosmic ray events. From the image, the direction as well as the intensity can be inferred. Almost without any model-specific assumption, the shower size as a function of the atmospheric depth

can be derived from the intensity measured. Thus, estimating the location of the air shower maximum  $X_{\max}$  becomes possible.

### Fluorescence telescopes

Here, the fluorescence light technique is used to directly record the longitudinal profile of extensive air showers. At very high energies ( $\gtrsim 100$  PeV), a considerable amount of light is emitted by nitrogen molecules of the air, caused by interactions with charged secondary air shower particles as they are traversing the atmosphere. The *fluorescence yield*, i.e. the number of photons per deposited energy unit radiated from the nitrogen, depends on the atmospheric conditions and the composition of the air. Therefore, fluorescence telescopes provide reliable data only if operated in combination with a system of atmospheric monitoring facilities (see e.g. [ICR09a]). Since there is no evidence for a dependence of the fluorescence yield on the energy of the exciting charged particle, calorimetric measurements of the energy deposit in the atmosphere is possible. The level of precision is limited by the predictions of the yield, model dependent effects introduce only a minor energy uncertainty. Geometric shower observables, i.e. the arrival direction of the primary cosmic ray, can be determined from the image of the light track recorded. For monocular observations, the angular uncertainty with respect to the orientation of the shower plane is in the order of magnitude of  $1^\circ$ ; the resolution for the direction of the shower axis is much worse (up to  $15^\circ$ ). By combining the observation of two telescopes, a considerable improvement can be achieved. The angular resolution in this case is better than  $1^\circ$ . Unfortunately, the duty cycle of fluorescence telescopes is comparable to that of Čerenkov detectors (i.e. about 10% only), because both techniques rely on the observation of light in the atmosphere.

### Radio detectors

The electromagnetic waves in the radio-frequency range, as they are emitted by extensive air showers, are exploited for this type of detector. The predominant effect in this case is commonly referred to as the *geosynchrotron mechanism*. The radio emissions are caused by the acceleration of charged secondary air shower particles in the Earth's magnetic field. Another effect, the *Askaryan effect* [Ask65], which becomes relevant for extensive air showers propagating in dense media, is caused by the coherent superposition of Čerenkov radiation originating from the charge excess of the charged secondary particles. For energies exceeding some 100 PeV, radio detectors might complement the available detection methods, once the technological and theoretical challenges have been overcome.

# Chapter 3

## Pierre Auger Observatory

The major challenge concerning the detection of cosmic radiation in the energy regime of several 100 TeV and beyond consists in the low flux of the radiation. The restrictions in terms of the detector volumes balloon-borne and satellite-borne experimental setups are able to provide render the acquisition of a considerable amount of data in a reasonable period of time impossible.

For energies in the EeV regime, the situation gets even worse as the rate of cosmic ray particles drops down to a value in the order of magnitude of a few particles per century and square kilometer. Medium-sized experiments at ground level of the Earth, exploiting the development of extensive air showers within the atmosphere above their setups, do no longer suffice as long as their active area does not exceed a few square kilometers.

The only solution to this problem lies in enlarging the active detection area to such an extent that the acquisition of a considerable amount of cosmic ray data becomes feasible. The Pierre Auger Observatory will finally end up at a total active area in excess of 20,000 km<sup>2</sup> for the joint operation of its northern and southern sites. At primary particle energies in the order of magnitude of 100 EeV, it will then be capable of recording about 200 extensive air showers per year. Moreover, it will record cosmic rays from the whole sky. The Pierre Auger Observatory combines two detection methods to form a *hybrid detector*, which (among other things) allows measurements of unprecedented accuracy. Another advantage of hybrid measurements consists in the possibility of a cross-calibration of the detector components.

As of writing this, only the southern site of the observatory is completely deployed and operational. Unless otherwise noted, it is therefore that site the term *Pierre Auger Observatory* refers to in the thesis at hand.

### 3.1. Southern Observatory Site

The southern site is located in the Pampa Amarilla, near Malargüe in the province of Mendoza, Argentina (35° S, 69° W). It covers an area of 3000 km<sup>2</sup>, hosting about 1600

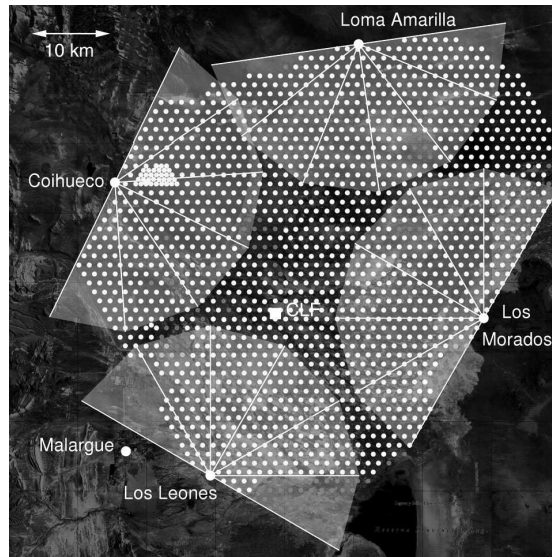


**Figure 3.1.:** Map of the southern observatory site (taken from [Abr10a]). An area of  $3000\text{km}^2$  is covered by about 1600 surface detector (SD) stations (indicated by dots). The fluorescence light in the atmosphere above the array is observed by four fluorescence detector (FD) stations, each one located at the borders of the array. Each FD station consists of six telescopes (or bays). Their fields of view of  $30^\circ \times 30^\circ$  each (indicated by lines) add up to a total of  $180^\circ \times 30^\circ$  for each of the FD stations.

surface detector (SD) stations and four fluorescence detector (FD) stations. The altitudes are ranging from 1300 m up to 1500 m [Blü10].

### 3.1.1. Surface Detector (SD)

Since 2008, the surface detector of the southern Pierre Auger Observatory site is completely deployed. The surface detector stations are arranged on a triangular grid with a spacing of 1.5 km. The SD component reaches a duty cycle of nearly 100% [Abr09a] and therefore it records the largest fraction of the cosmic ray data acquired by the observatory. However, it only observes the lateral air shower profile. The reconstruction of the cosmic ray properties is thus associated with large uncertainties due to the limited knowledge of the cross sections of inelastic hadronic interactions.

Full trigger efficiency is reached for primary particle energies in excess of 3 EeV for the full zenith angle range. For energies ranging from 0.7 EeV to 1 EeV about 50% of all cosmic ray particles are detected [Blü10], depending on the zenith angle and the type of the primary particle.

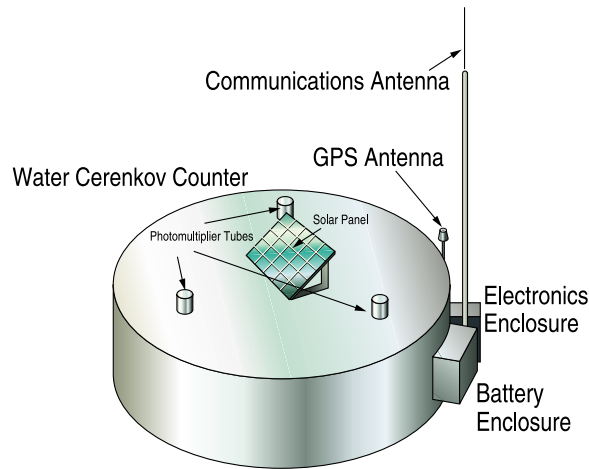


**Figure 3.2.:** Schematic view of an SD station (adapted from [Cro96]). The main components, i.e. the photomultiplier tubes (PMTs), the antennas, the batteries and the electronics box as well as the solar panel, are shown.

### Detector Station

A schematic view of an SD station is shown in Fig. 3.2. The configuration of the station resembles that of the detectors used for the Haverah Park experiment [Law91], where this type of setup proved to work reliably for a long period of time with low requirements for maintenance.

The Čerenkov effect is exploited to detect charged secondary air shower particles. A volume of  $12\text{m}^3$  of purified water is used as the detection medium. The water is filled into a reflective Tyvek<sup>TM</sup> liner inside a cylindrical polyethylene tank [All08a]. The water reaches a level of 1.2m. Three identical photomultiplier tubes, each one 8 inch in diameter, are optically coupled to the water to detect the photons on passage of the charged particles. The PMTs provide signals at their anodes and at the last dynode to obtain the signals for two different amplification factors. The PMTs reach an amplification in the order of magnitude of  $10^5$ . The three low-gain and the three high-gain signals are processed by the data acquisition system in each station. The signals are digitised at a rate of 40 million samples per second, using FADCs (Flash Analogue to Digital Converters). The channels with a low gain and those with a high gain are overlapping in such a way that the total signal resolution amounts to 15 bits. Typically, pulses caused on passage of a charged particle decay after  $\approx 60\text{ns}$ . The PMT signal traces recorded are stored for a period of time of ten seconds so they can be sent to the CDAS (Central Data Acquisition System) on demand. In addition to the PMT signals, monitoring data, regarding temperatures, voltages etc., is taken to record the instantaneous state of the station. The detector stations of the Pierre Auger Observatory are operating stand-alone. They are battery-powered, with the batteries being charged using a solar panel system. The total power dissipation does not exceed 10W. Data

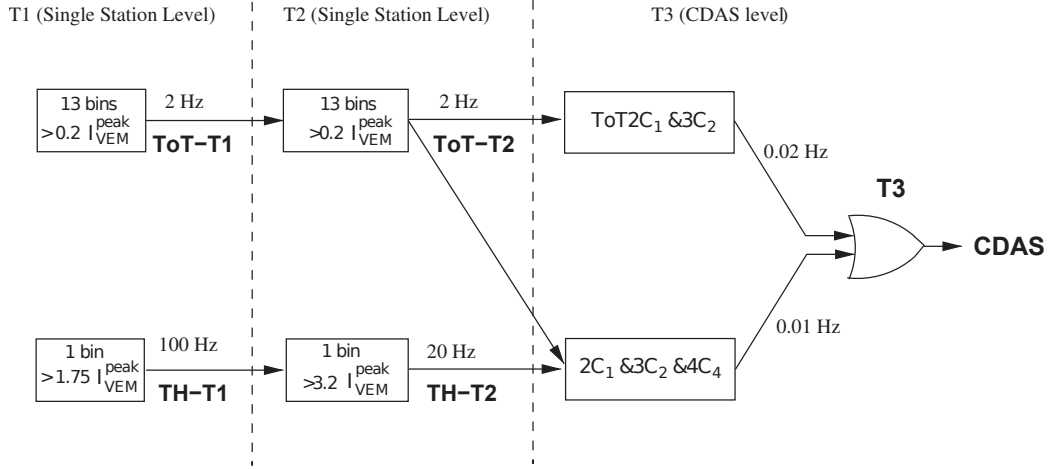


**Figure 3.3.:** Schematic view of the hierarchy of the SD trigger system (taken from [Abr09a]).

transmission to the CDAS (Central Data Acquisition System) is accomplished using wireless transmission via the nearest communication beacon. A GPS (Global Positioning System) unit is used as a time base for synchronising the SD stations and the CDAS. The uncertainty of the GPS time ( $\approx 8$  ns) and the uncertainty of the determination of the PMT pulse start ( $\approx 7$  ns) add up to a total uncertainty of  $\approx 10$  ns.

### Hierarchy of the SD Trigger System

The hierarchy of the trigger system for the SD (Surface Detector) component is described in detail in [Abr09a], its schematic view is shown in Fig. 3.3.

On the station level, the local trigger types T1 and T2 are formed. The T1 trigger type actually comprises two modes. Firstly, a pure threshold trigger with a coincidence in all PMTs. It is mainly sensitive to large signals which are compact in time. This is the case for very inclined extensive air showers, for which the electromagnetic air shower component has nearly died out completely, whereas the muon component still reaches the detector stations. This trigger condition is approximately fulfilled a hundred times per second, corresponding to about 3% of the total rate of atmospheric muons. The second variant of the T1 trigger aims at detecting less inclined extensive air showers, with the core of the air showers closer to a surface detector station. Due to the dispersion of the electromagnetic air shower component, the signals recorded by the SD stations are spread in time, but they do not exhibit a pronounced maximum value. Thus, this T1 variant triggers if a TOT (Time-Over-Threshold) condition is fulfilled during a time period of  $3 \mu\text{s}$ . The trigger rate of this type of T1 trigger is in order of magnitude of 2 Hz only due to the fact that signals caused by atmospheric muons are too short in time to fulfill the TOT (Time-Over-Threshold) condition.

The T1 triggers to be reported to the CDAS (Central Data Acquisition System) are

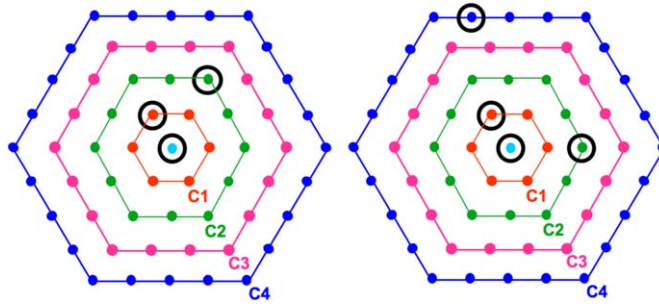


**Figure 3.4.:** T3 trigger configurations (taken from [Abr09a]). *Left:* Compact type of a T3 condition. At least three detector stations, reporting a T2 trigger, in a compact spatial configuration. *Right:* Less compact type of a T3 condition. At least four detector stations, reporting a T2 trigger, in a less compact spatial configuration.

to pass the T2 trigger level as well. The TOT–T1 is always promoted to the T2 level. For the pure threshold trigger, the signals have to pass another, higher, threshold trigger level to be promoted. The latter is required to further reduce the rate of transmission via the wireless communication system.

On the level of the surface detector array, the T3 trigger level selects stations whose T2 triggers are compatible with an air shower event, with respect to both the time and space requirements. If the T3 condition is fulfilled, the CDAS (Central Data Acquisition System) requests the corresponding FADC traces from the stations which were found to be candidate stations. The T3 trigger type again has two variants; see Fig. 3.4 for an illustration. One of the variants requires three T2 triggered stations in a compact configuration. The other variant allows T2 triggered stations in a less compact spatial configuration, but it requires at least four of them. The trigger rates contributed by both variants amount to 0.02 Hz and 0.01 Hz, respectively.

Following the T3 level, two additional trigger levels are to be fulfilled for the recorded station data to be taken into account for an air shower event reconstruction. The T4 trigger level restricts the outcome of the T3 stage to station configurations which are compatible with the geometry and time structure of extensive air showers; it is therefore referred to as a *physics trigger*. Finally, the T5 level of the trigger hierarchy can be considered a fiducial cut. It discards event candidates with a reconstructed air shower core at the borders of the array to make sure the reconstruction of the arrival direction and the energy estimation is not subject to large deviations.

## SD Calibration

The surface detector stations of the **Pierre Auger Observatory** provide two methods for their calibration. Firstly, the *online calibration* is basically accomplished by stabilising the background rate of atmospheric low energy muons detected at about 100 Hz. By adjusting the threshold for the T1 trigger accordingly once every minute, a uniform performance of

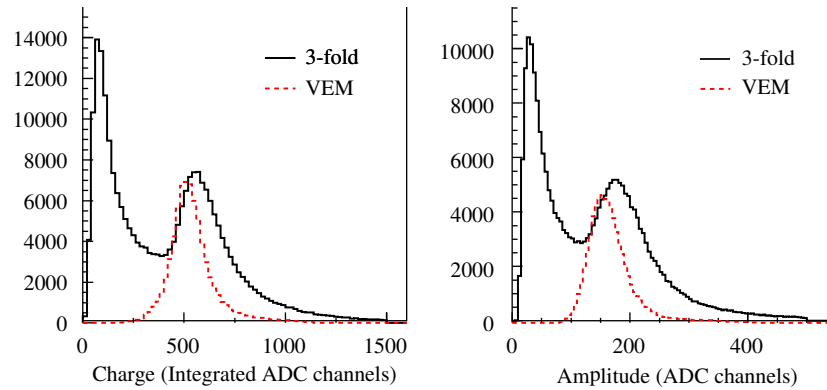


**Figure 3.5.:** Histograms of the charge (figure on the left) and pulse height (figure on the right) as recorded by an SD station (both taken from [Ber06]). The solid line stems from a 3-fold coincidence of the PMT signals, whereas the dashed line is obtained from a reference measurement using an external muon detector to select vertical muons.

the surface detector trigger is achieved. In addition, this type of calibration is used once during the startup sequence of the individual SD (Surface Detector) station to adjust the supply voltages for each of the three PMTs, since their amplification factors depend on the voltage applied. Apart from stabilising the station trigger rate, the ratio of the amplification factors for the anode and the last dynode of the PMTs are calculated from the signal traces of both channels during the *online calibration*.

The second mode, the *offline calibration*, makes use of histograms filled during the operation of an SD (Surface Detector) station (cf. Fig. 3.5). For each signal trace recorded, the pulse height and the integral of the area above the baseline of the signal are evaluated. A pronounced peak is seen at the FADC channel number corresponding to muons hitting the water volume from the vertical. A correction factor has been determined from hodoscope measurements for one tank [Ber06] by selecting muons entering the water Čerenkov detector station exactly at a zenith angle of  $0^\circ$ . The *offline calibration* is too expensive in terms of the computing power required to be accomplished online by the SD (Surface Detector) station itself. Instead, the histograms of the peak FADC (Flash Analogue to Digital Converter) values and the integrated charge are sent to the CDAS (Central Data Acquisition System) for further analysis, when a signal trace is requested by CDAS (Central Data Acquisition System). By applying this method, the energy unit VEM (Vertical Equivalent Muon), corresponding to vertical incidence of a muon, can be related to the signal recorded by an SD (Surface Detector) station with an uncertainty as low as 2% [Abr09a].

### 3.1.2. Fluorescence Detector

The fluorescence detector of the southern Pierre Auger Observatory site consists of four telescope buildings, each one hosting six telescope bays. The telescopes cover a field



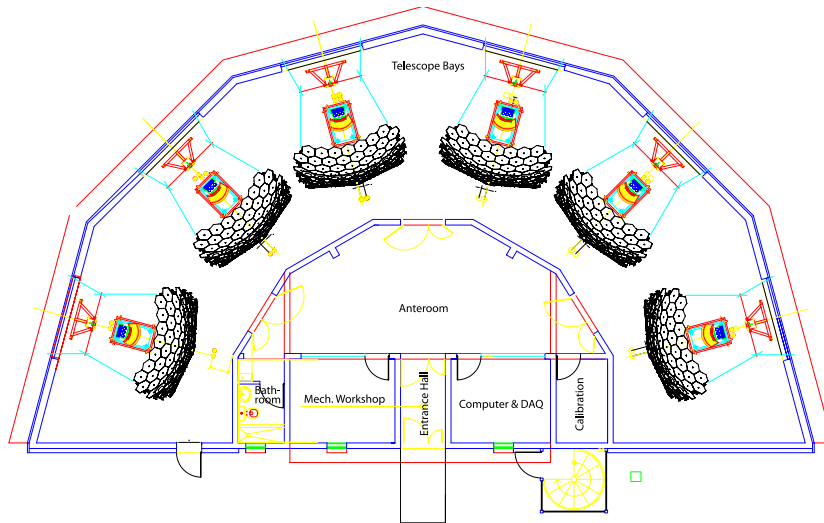


**Figure 3.6.:** Schematic view of a typical FD (Fluorescence Detector) building (taken from [Abr10a]). The six telescopes cover a field of view of approximately  $30^\circ \times 30^\circ$  each, adding up to approximately  $180^\circ \times 30^\circ$  in all.

of view of approximately  $30^\circ \times 30^\circ$  each, in total approximately  $180^\circ \times 30^\circ$  for a single FD (Fluorescence Detector) building. The fluorescence detector buildings are arranged at the borders of the surface detector array to monitor the atmosphere above the SD array.

The data acquisition of the FD can take place when the moon fraction drops below 60%. This corresponds approximately to a fortnight per month on average. In these nights, the actual data taking starts with the onset of the astronomical dusk and it ends with the onset of the astronomical dawn, resulting in an average time interval of ten hours in length. Thus, the FD telescopes are operational during 13% of the time. The duty cycle for individual telescopes may vary depending on the level of moon light at the different sites.

### FD Telescope

The FD (Fluorescence Detector) telescopes of the Pierre Auger Observatory make use of the detection method that was already exploited by e.g. the HiRes experiment. Basically, the atmosphere in which the extensive air showers develop as a consequence of the impact of a primary cosmic ray particle, is used as a calorimeter volume. The charged component of the secondary particle cascades excite nitrogen molecules of the air as the air shower propagates through it. The molecules then return to their ground state again, isotropically emitting fluorescence light. The number of photons emitted per unit energy is referred to as the *fluorescence yield*. As the main fraction of the primary cosmic ray energy is converted into the charged secondary particles of the air shower, the estimation of the energy can be accomplished by measuring the fluorescence light.

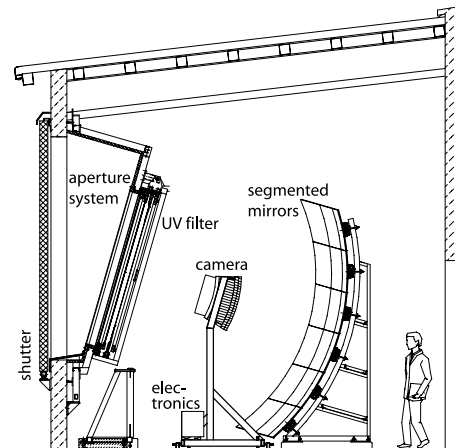


**Figure 3.7.:** Schematic view of an FD telescope (taken from [Abr10a]). Six of these units, named *Schmidt telescopes*, are installed in each of the FD (Fluorescence Detector) buildings to cover the full field of view of  $180^\circ \times 30^\circ$ , whereas each telescope bay only covers a fraction of  $30^\circ \times 30^\circ$ .

A schematic view of a typical FD telescope is shown in Fig. 3.7. The actual light detector, the *camera*, is assembled from 440 hexagonal shaped PMTs arranged in 22 rows with 20 pieces each. Each PMT contributes one of the pixels of the light detector. The pixel camera is located in the focal plane of a spherical mirror  $12\text{m}^2$  in size. A system of corrector lenses and filters complements the optical system of the telescope. As a security measure, a *shutter* can be lowered to protect the sensitive optical setup from damages due to sudden bright light or dangerous weather conditions like e.g. a thunderstorm.

For each of the camera pixels, the PMT signal is digitised at a rate of ten million samples per second, using 12 bit FADC (Flash Analogue to Digital Converter) devices. About  $100\mu\text{s}$  of the digitised signal are kept in a circular data buffer.

Each FD building is equipped with a GPS receiver for a time synchronisation of the detector components. In addition, weather station equipment is installed at each FD building (cf. Section 4).

### FD Trigger System

There are three levels of FD triggers. The first level is implemented for each of the camera pixels. The integrated PMT signals are compared to a threshold value to form a trigger. The threshold is tracked in such a way that the trigger rate per pixel is stabilised at about 100 Hz.

In a second level, the spatial structure of the pixel triggers is taken as a criterion. If five or more pixels roughly form a straight line, it is considered a candidate for a real event. The rate of this trigger ranges from a fraction of one Hertz up to several Hertz.

The third trigger level is supposed to suppress lightning events, charged particles

hitting the camera pixels and other triggers not related to air showers.

In each FD building, the local data acquisition system processes the triggers received from the bays. Event data is then sent to the CDAS for further processing and storage. It is also possible to initiate the readout of the SD array upon the acquisition of FD event data. In a joint data taking the arrival direction can be improved considerably more accurate than for the FD alone.

### FD Calibration

The *absolute calibration* of an FD telescope is accomplished by means of a diffuse light source to be mounted at the aperture of the FD bay. The camera is then illuminated by this calibrated light source and the measured light intensity is compared to the expected values to obtain a calibration. Since this type of calibration is rather time-consuming, it is only carried out a couple of times per year.

The *relative calibration* relies on a valid absolute calibration. Then light sources inside the FD bay can be used to monitor the short term variations of the performance of the detector system.

### Atmospheric Monitoring

For the FD (Fluorescence Detector), the knowledge of the instantaneous state of the atmosphere is inevitable. Facilities like the CLF (Central LASER Facility) and XLF (extreme LASER Facility) are used to provide reference beams of ultraviolet light to be detected by the telescopes. The LIDAR (Light Detection And Ranging) systems help in estimating the amount of aerosols in the air. In measurement campaigns of balloon launches, the vertical profile of the air in terms of the temperature and the density of the air is evaluated. For a detailed overview of monitoring efforts at the Pierre Auger Observatory see e.g. [ICR09a, Wie09, Kei09].

### 3.1.3. Enhancements for the Southern Site

To cover the energy regime down to  $10^{17}$  eV, two enhancements of the existing southern Pierre Auger Observatory site have been proposed, AMIGA (Auger Muon detectors and Infill for the Ground Array) and HEAT (High Elevation Auger Telescopes). In addition, the research and development of radio detectors is underway in the scope of AERA (Auger Engineering Radio Array).

#### HEAT

The HEAT (High Elevation Auger Telescopes) enhancements [ICR09b] consists of three fluorescence telescopes near the *Coihueco* telescope site; see Fig. 3.8(a). The new telescopes are similar to the FD telescopes of the original Pierre Auger Observatory design. However, it is possible to tilt the HEAT telescopes to extend the field of view of the

Coihueco site by  $30^\circ$  towards the vertical. Thus, the longitudinal profile of extensive air showers at lower energies can be measured, combining the measurements by the original FD telescopes and those of HEAT (cf. Fig. 3.8(b)).

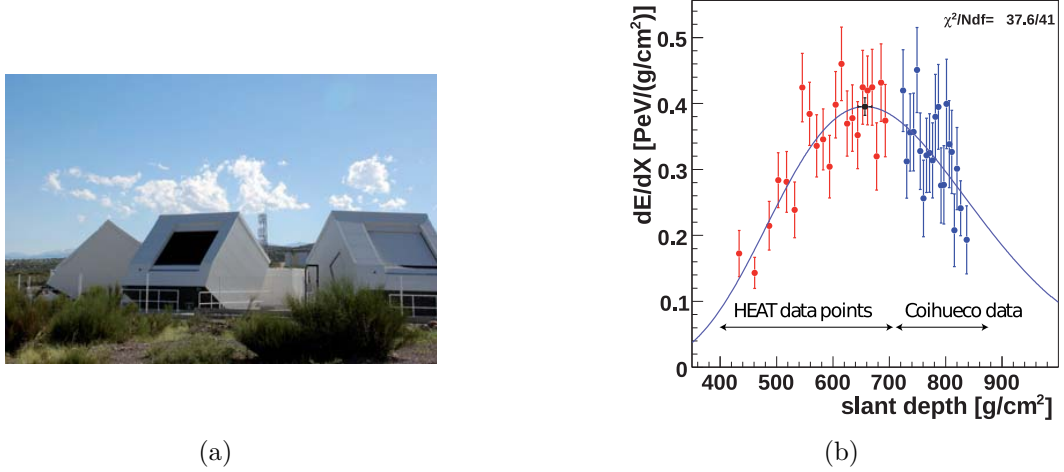


**Figure 3.8.:** HEAT (High Elevation Auger Telescopes) enhancement of the southern site of the Pierre Auger Observatory. *Left:* Picture of the three tilted HEAT telescopes on the Coihueco site. *Right:* Joint measurements by the original FD telescopes and the HEAT enhancement. Both taken from [ICR09b].

## AMIGA

Another enhancement concerns the deployment of additional surface detector stations on a dense grid to extend the energy range of the surface detector array towards lower energies. As a consequence, a part of the array will contain SD (Surface Detector) stations on a grid with 750 m and 433 m of spacing, respectively [Sup08].

Alongside 85 of those detector stations, muon counters will be buried; see Fig. 3.9 for an illustration. These detectors are shielded from the electromagnetic air shower component by the overburden of soil. As a consequence, they essentially only measure the muon component of the air showers. In a coincident measurement with a nearby detector station, this allows the separation of the electromagnetic and the muonic components of the lateral air shower profile, thereby providing a tool for composition analyses. Each underground detector will cover an area of  $30\text{m}^2$  of active scintillator area. The scintillator strips are optically coupled to a 64 pixel photomultiplier tube. The signals of each pixel are processed at a sample rate of approximately 300 million samples per second.

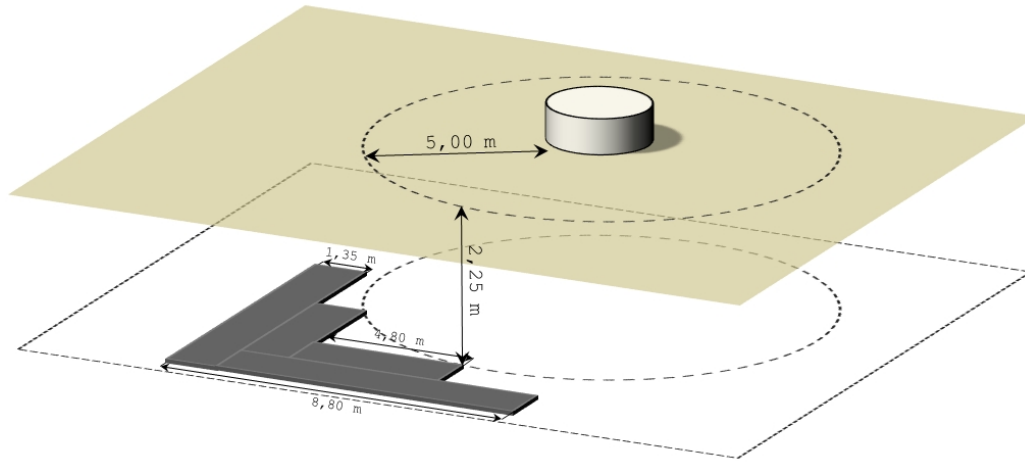


**Figure 3.9.:** Layout of a typical AMIGA muon counter (bottom), buried alongside an SD station (top) of the infill array. Taken from [Frö09].

## AERA

The AERA (Auger Engineering Radio Array) detector will cover a total area of approximately  $20\text{ km}^2$  in total. About 150 stand-alone detector stations will be distributed on that area, with a core area, where the stations are deployed on a grid with a spacing of 150 m and outer regions which are only sparsely populated with detectors [vdB65, ICR09b].

## 3.2. Northern Observatory Site

The northern site of the Pierre Auger Observatory will be located in the state of Colorado, USA, at an average altitude of 1300 m, at  $38^\circ\text{ N}$  and  $102.5^\circ\text{ W}$  [Blü10]. It will cover an area of  $20,000\text{ km}^2$ .

About 4000 surface detector stations will be deployed on a grid with a spacing of 2300 m. This detector will reach its full trigger efficiency at energies of 80 EeV, at energies of 10 EeV, about 50% of the air showers will trigger the array. The SD stations will be operated with only a single PMT (Photo Multiplier Tube) to reduce costs.

Five FD (Fluorescence Detector) stations with a total of 39 telescopes will be deployed to observe the fluorescence light in the atmosphere above the array. The atmospheric monitoring will be accomplished using DLF (Direct LASER Facility) units, distributed over the array.

The construction is planned to start in 2011 and it is expected to be finished in 2016 [Blü10].



# Chapter 4

## Sources of Weather Data

The development of extensive air showers in the atmosphere, and consequently the signals measured by detectors at ground level, depends on quantities describing the state of the atmosphere and therefore on the weather conditions.

Any attempt to compensate for weather-related effects is reliant on information on the instantaneous weather conditions. Therefore, weather data has to be acquired at a reasonable precision and rate, so each air shower event detected by the **Pierre Auger Observatory** can be assigned a corresponding set of weather observables.

The knowledge of the current atmospheric state is of paramount relevance for properly interpreting fluorescence detector data. Apart from the quantities, which primarily describe the Earth's atmosphere, i.e. the pressure  $P$ , the temperature  $T$  and the density  $\rho$  of the air, additional atmospheric properties are impacting the measurements in the case of fluorescence detectors, like they are used as one part of the hybrid detector for the **Pierre Auger Observatory**. This type of detector exploits the amount of light emitted by nitrogen molecules which are excited by charged air shower particles, that are traversing the atmosphere. It is used as a measure of the deposited energy per unit path length for the calorimetric determination of the primary particle energy. The light yield actually detected is varying depending on the instantaneous composition of the air. Therefore, the gas mixture and the amount of aerosols in the atmosphere have to be monitored all the time for a proper reconstruction of the energy. The CLF, the XLF as well as the LIDAR systems have been deployed for the purpose of accomplishing this monitoring task. However, this is not related to the development of extensive air showers, but rather it is linked to measurement issues. Since only air shower data acquired by the SD component of the **Pierre Auger Observatory** are used in the thesis at hand, the impact of the weather on the fluorescence detector is beyond the scope of the analysis and hence it is not addressed in more detail in this chapter. However, the energy calibration of the surface detector is obtained by relating its signal (converted to the value corresponding to an incidence at the reference zenith angle of  $38^\circ$ ) to the energy reconstructed by the FD. Any systematic deviation introduced as part of the air shower detection and

reconstruction of the longitudinal profile by means of the fluorescence detector is thus also impacting the reconstruction of surface detector data.

Albeit the weather impact is negligible for surface detector events initiated by primary particles of sufficiently high energy, this no longer holds when data corresponding to primaries, that do not meet the energy requirement for fully efficient detection, are to be considered in analyses. The latter is the case for the analysis at hand. Consequently, in this chapter the focus is put on available sources of weather information, provided by facilities on site of the **Pierre Auger Observatory**, as well as on the major climatic characteristics of the region covered by the observatory.

## 4.1. Climatic Site Characteristics

Among the characteristics defining the climatic situation, the range covered by the barometric pressure of the air on site of the **Pierre Auger Observatory** as well as the temperatures reached during the course of a year, and the magnitude of the variations in air density are those observables that are most relevant to the analysis at hand. Data taken by the central LASER facility of the observatory has been used to assess the climatic situation. The weather data set contains information collected from June 22, 2004, until December 31, 2009. As can be seen from Fig. 4.1(a), the air pressure is subject to variations at the level of 4 hPa only, never deviating more than  $\approx 20$  hPa from the mean barometric pressure. The overall mean temperature is  $14^\circ\text{C}$ , on average the temperature varies within  $\pm 10^\circ\text{C}$  (see Fig. 4.1(b)). In rare cases, the instantaneous temperature can fall below the mean temperature by up to  $40^\circ\text{C}$  or it can reach values of up to  $20^\circ\text{C}$  above the mean. Since the air density is none of the observables directly measured by the CLF, it has to be calculated from the barometric pressure and the air temperature by way of the ideal gas law; the validity of this approximation is verified in Section 4.4. According to Fig. 4.1(c), the density of the air amounts to  $1.06\text{ kg/m}^3$  on average and it is subject to variations of  $40\text{ g/m}^3$  on average. Variations of up to  $\pm 100\text{ g/m}^3$  with respect to the mean value are reached in some cases. On a seasonal scale, the time evolution of the temperature and the density of the air at ground level is shown in Fig. 4.2. Since only small overall variations of the air pressure are observed, its evolution has not been broken down into seasons.

## 4.2. Weather Stations

Weather stations are installed at all fluorescence telescope buildings of the **Pierre Auger Observatory**. In addition, information on the instantaneous weather conditions are provided by the CLF and the BLS (Balloon Launch Station). Fig. 4.3 shows, where the various stations are situated with respect to the observatory site. Unfortunately, not all weather stations were deployed already back in January 2004, when the observatory



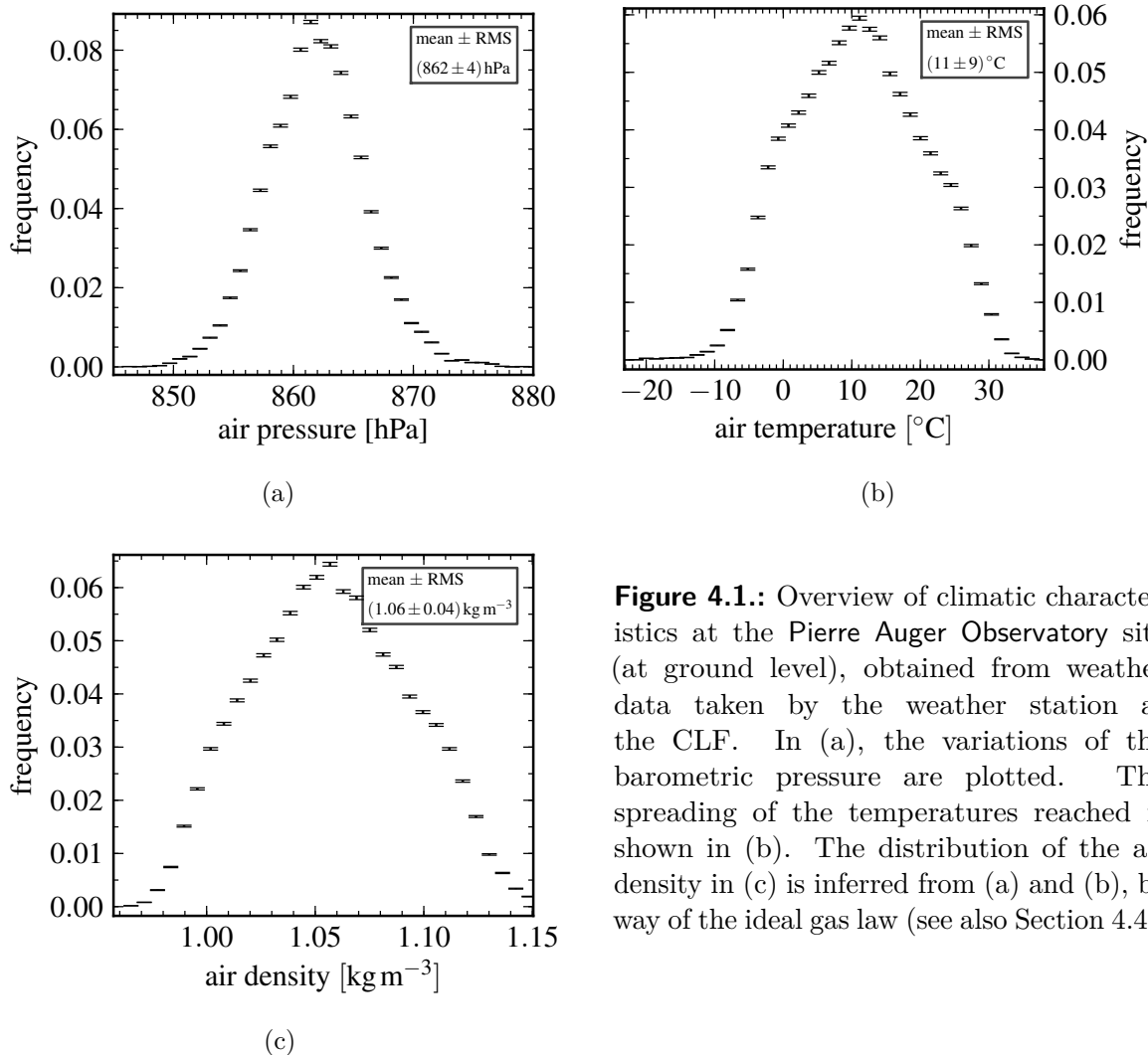


**Figure 4.1.:** Overview of climatic characteristics at the Pierre Auger Observatory site (at ground level), obtained from weather data taken by the weather station at the CLF. In (a), the variations of the barometric pressure are plotted. The spreading of the temperatures reached is shown in (b). The distribution of the air density in (c) is inferred from (a) and (b), by way of the ideal gas law (see also Section 4.4).

officially started to acquire air shower data. As a matter of fact, Los Leones was the only source of weather information then, followed by the central LASER facility, brought into service about half a year later.

The weather stations are designed to sample the weather observables in regular intervals of five minutes. The stations are recording a time stamp (UTC seconds), together with the instantaneous values of the air temperature (in  $^{\circ}\text{C}$ ), the relative humidity of the air (in percent), the wind speed (in km/h), the direction of the wind (in degrees, relative to the north), and the barometric pressure (in hPa) [All88].

Because of communication outages, scheduled maintenance work, power failures, etc., the weather stations do not continuously monitor the ambient conditions; see Fig. 4.4 for an overview of the duty cycles for the various facilities. As a consequence of the discontinuities, from January 2004 until December 2009 only outdated weather data,

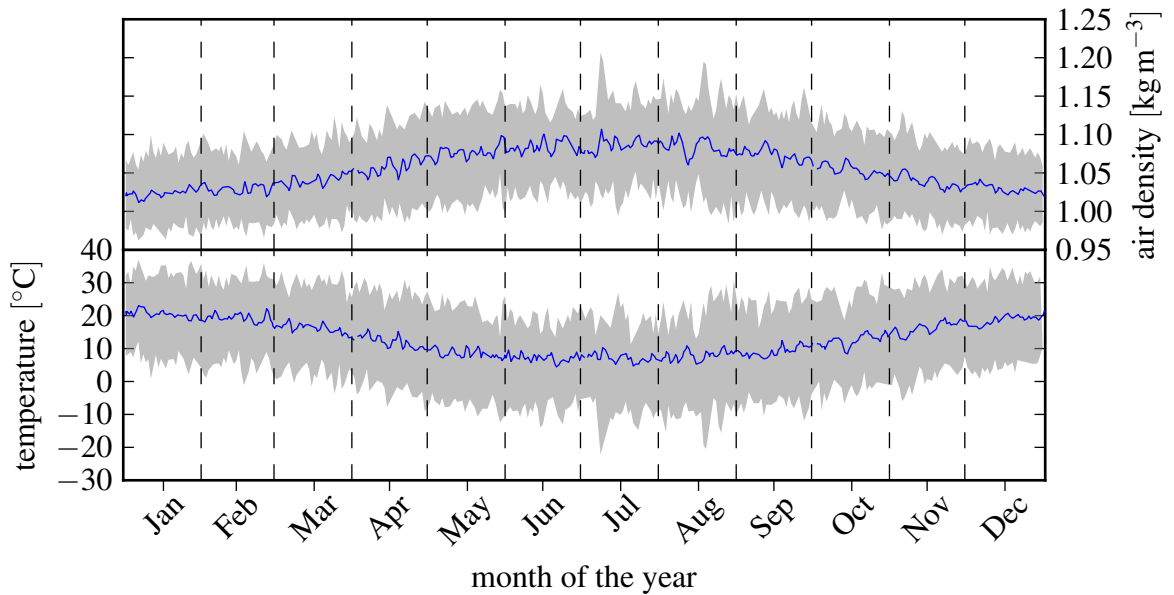


**Figure 4.2.:** Variation of the air density and temperature on a seasonal scale, averaged over a time period of 5.5 years (June 2004 to December 2009), at ground level of the CLF. *Upper pane:* Density of the air during the course of a year. *Lower pane:* Temperature of the air during the course of a year. The light grey areas depict the ranges that are covered by the quantities during the respective days of the year. The solid line results from a convolution of the instantaneous values with a (24 hours) top-hat window function. To avoid boundary effects, one day of data at the end of the time period has been prepended to the first day prior to convolution.

i.e. data older than one hour, are available for about 6% of the extensive air shower events detected. Although it is, in general, possible to complement missing information of one weather station with data taken by another one [All88], this procedure is prone to introducing a systematic deviation into the weather observables.

In addition to the regular operation of permanent weather station facilities, exploratory measurement campaigns are undertaken several times each month to collect data on the variation of the atmospheric state in a time scale of months [Kei21]. Balloon-borne weather sensors are used to accomplish these sounding missions. During the ascent of such a setup, information on the temperature, the barometric pressure, and the density of the air are collected at different altitudes above ground, in steps of 200 m. Moreover, balloons can be launched on demand, within a few hours from the detection of extensive air shower events whose reconstructed primary energy exceeds a specific threshold (see e.g. [Wil81]). In this way, it is possible to reduce the systematic uncertainties associated with the corresponding air shower measurements.

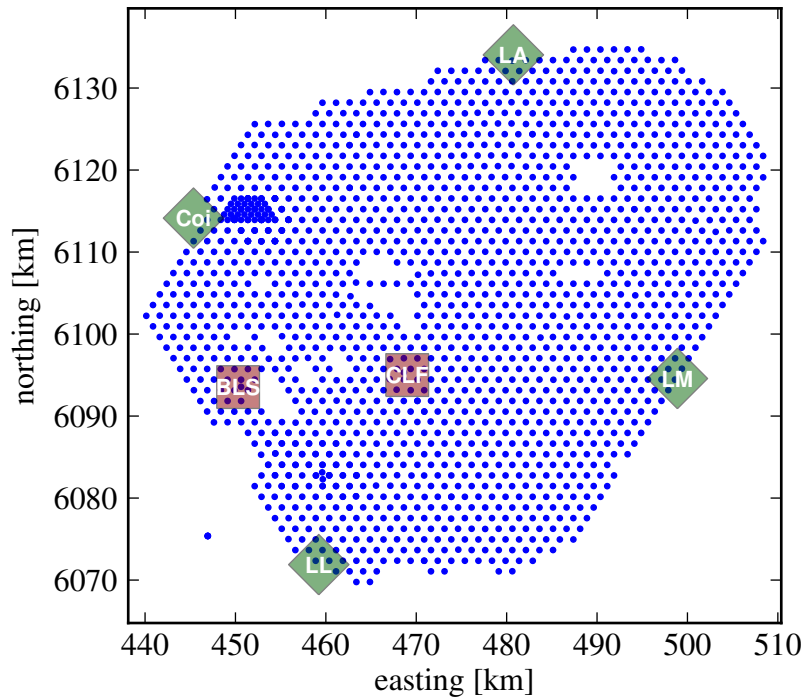


**Figure 4.3.:** Facilities on site of the Pierre Auger Observatory, hosting weather station equipment. The balloon launch station (BLS) and the central LASER facility (CLF) are depicted by reddish squares. Fluorescence telescope buildings are indicated by greenish, diamond-shaped markers (LA  $\hat{=}$  Loma Amarilla, LM  $\hat{=}$  Los Morados, LL  $\hat{=}$  Los Leones, Coi  $\hat{=}$  Coihueco); see Tab. 4.1 for the coordinates. In addition to these facilities, the water Čerenkov detector stations are marked by blue circles. All positions are given as UTM system coordinates (reference ellipsoid WGS84, zone 19H).

### 4.3. Deviations of Weather Station Data

The Pierre Auger Observatory covers a vast area, about  $3000 \text{ km}^2$  in all. The fluorescence detector telescope buildings, all of which are now hosting weather stations, are arranged at the outer boundaries of the area such that the atmosphere above the entire surface detector array can be surveyed. The BLS and CLF facilities, located within the array, are still far away from each other and also from the telescope buildings. Deviations of the quantities measured by individual weather stations arise therefore unavoidably from the mere distance of the stations between one another. In particular, rapid changes of the weather conditions take some time to propagate across an area as large as that of the Pierre Auger Observatory surface detector array. This type of systematic deviation is not predictable and hence it cannot be compensated for. As an example for the deviations, that are largely caused by this kind of effect, temperature data taken by the weather stations at the CLF and the fluorescence telescope building at Los Leones, respectively,

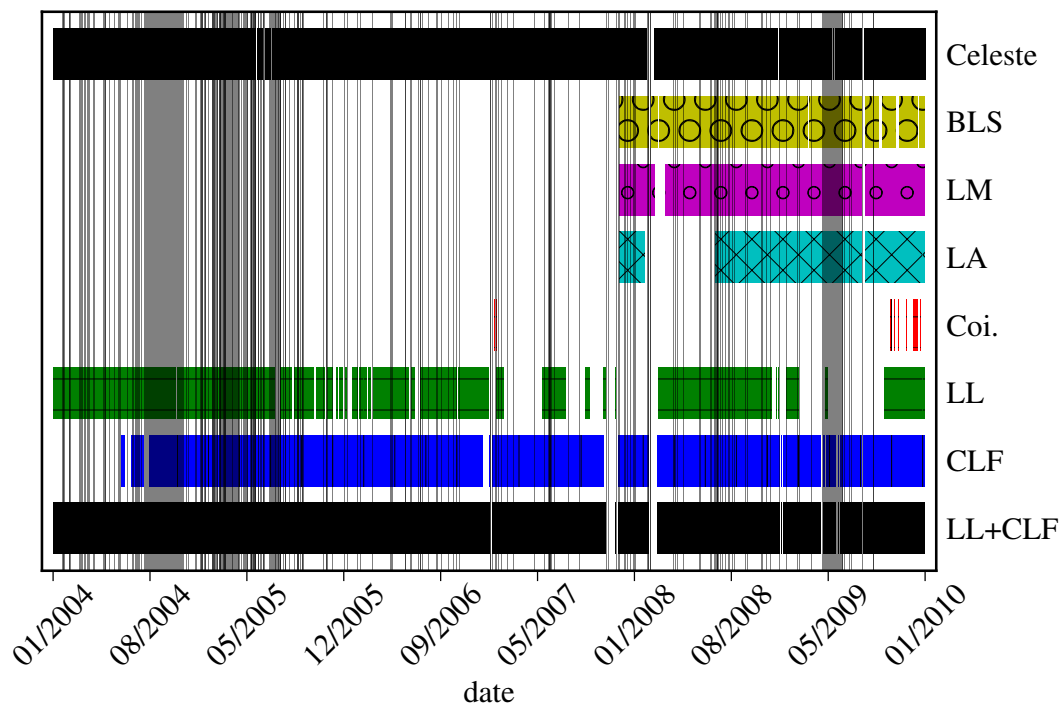


**Figure 4.4.:** Duty cycles of the various weather stations. The horizontal bars indicate the time periods of at least one hour of continuous weather data flow from Los Morados (LM), Loma Amarilla (LA), Coihueco (Coi.), the BLS, the CLF and Los Leones (LL), respectively. Accordingly, the gaps in the bars indicate times, when individual stations were inoperative. In the bottom row, the duty cycle is shown for the combined operation of Los Leones and the CLF. In comparison, the time periods, during which the water Čerenkov detector station Celeste (LsId=203) has been operational, are drawn (top row). Vertical lines and translucent, grey bars indicate time periods of at least one hour, during which the surface detector was inoperative altogether or operating with degraded performance, thus not taking data reliably (“bad periods”).

are compared in Fig. 4.5. Temperature deviations between both stations of up to  $5^{\circ}\text{C}$  are observed. In Fig. 4.6, the same is shown with respect to the measurements of the barometric pressure; deviations of up to 2 hPa are found.

An additional systematic effect can be attributed to the fact, that the weather stations are situated at different altitudes (see Tab. 4.1). In connection with the dependence of the air pressure and the temperature on the altitude above ground, a systematic shift of the quantities measured by the stations can be observed even in case of an otherwise stable weather situation. This shift can be estimated and compensated for if the typical temperature gradient as well as the decrease in air pressure at a certain altitude is known. These information can be obtained e.g. from measurement campaigns using balloon-borne weather station equipment.

weather station	altitude [m]	easting [m]	northing [m]
CLF	1,401.3	469,378.00	6,095,769.00
BLS	1,426.0	450,295.33	6,093,531.74
Coihueco	1,712.3	445,343.80	6,114,140.00
Loma Amarilla	1,476.7	480,743.10	6,134,058.40
Los Leones	1,416.2	459,208.30	6,071,871.50
Los Morados	1,416.4	498,903.70	6,094,570.20

**Table 4.1.:** Locations of the weather stations on the Pierre Auger Observatory site, in UTM coordinates (reference ellipsoid WGS84, zone 19H).

By retrieving weather data, especially temperature information, right where it is needed, the systematic uncertainty introduced by the large distances can be avoided. In Section 4.5, this approach is investigated for the case of surface detector stations.

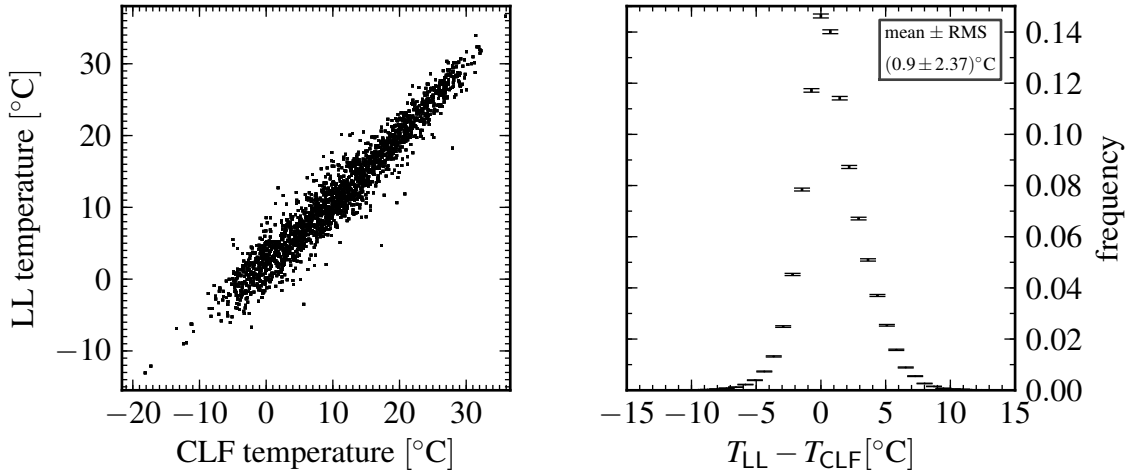


**Figure 4.5.:** Ambient temperatures recorded by the weather stations at Los Leones and the central LASER facility, respectively. See App. C for the data measured by all possible combinations of weather stations. *Left:* Correlation of the temperatures recorded by both stations simultaneously. *Right:* Distribution of the instantaneous deviations of the temperature measurements.

### 4.3.1. Temperature Gradient

By processing the temperature information obtained from the balloon-based measurements, it is possible to estimate the mean temperature gradient in the lower layers of the atmosphere (which corresponds to the relevant altitudes considered in this analysis).

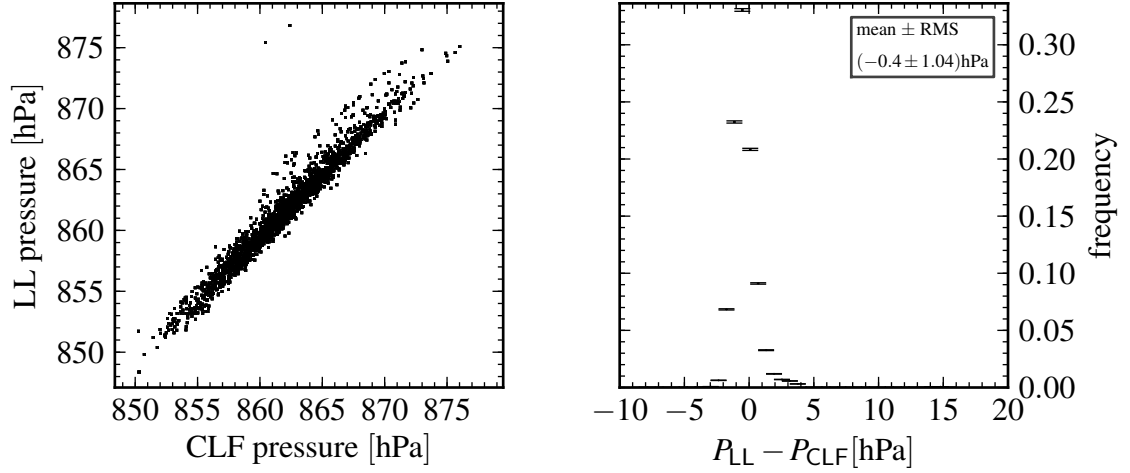


**Figure 4.6.:** Barometric pressure at ground level, recorded by the weather stations at Los Leones and the central LASER facility, respectively. See App. C for the data measured by all possible combinations of weather stations. *Left:* Correlation of the air pressure recorded by both stations simultaneously. *Right:* Distribution of the instantaneous deviations of the measurements of the barometric pressure.

For two weather stations located at different altitudes above sea level,  $h_1$  and  $h_2$ , the temperatures recorded by both of them simultaneously,  $T_1$  and  $T_2$ , can be matched by applying a compensation for the systematic shift:

$$\tilde{T}_2 = T_2 - (h_2 - h_1) \frac{\Delta T}{\Delta h}. \quad (4.1)$$

In this equation,  $\Delta T/\Delta h$  denotes the temperature gradient and  $\tilde{T}_2$  is the temperature measured by weather station 2, corrected for the different altitudes, such that it would match the value recorded by station 1 (apart from uncertainties not related to the altitude).

The temperature and altitude data taken during the balloon flights are shown in Fig. 4.7. Only the most recent data set for each month has been used. For each monthly profile, a value for the temperature gradient is determined from a linear regression fit to the data. The resulting values for each month are listed in Tab. 4.2. Averaging over all months, the mean temperature gradient can be estimated:

$$\Delta T/\Delta h = (-6.7 \pm 0.9) \cdot 10^{-3} \text{ }^\circ\text{C/m.}$$

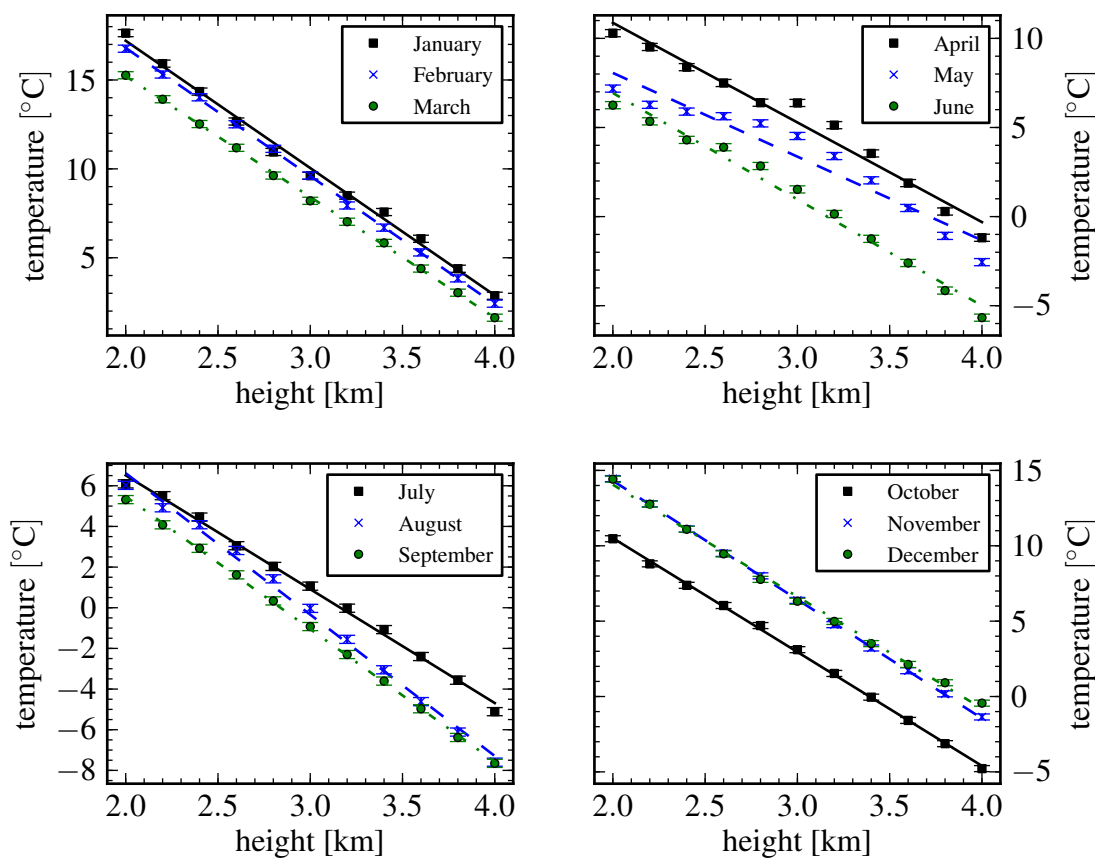


**Figure 4.7.:** Monthly profiles of temperature vs. altitude, as measured by balloon-borne radio sounding devices during exploratory campaigns.

	monthly profile					
	Jan	Feb	Mar	Apr	May	Jun
$\Delta T/\Delta h$ [°C/km]	-7.2	-7.2	-6.8	-5.6	-4.7	-6.0
	Jul	Aug	Sep	Oct	Nov	Dec
$\Delta T/\Delta h$ [°C/km]	-5.6	-7.0	-6.5	-7.6	-7.9	-7.4

**Table 4.2.:** Results for the temperature gradient in the lower atmospheric layers, from the linear regression fits to the monthly temperature profiles, obtained from balloon-based measurement campaigns. The uncertainty for the temperature gradients is in the order of magnitude of 0.1 °C/km for each of the fits.

### 4.3.2. Air Pressure Gradient

Actually, the pressure at a certain altitude  $h$  above ground is described by an exponential law:

$$P(h) \propto e^{-h/h_0},$$

where  $h_0$  denotes the pressure scale height (in the order of magnitude of 10 km). However, for low altitudes, i.e. for the lower *troposphere*, the dependence of the pressure on the altitude can be approximated by means of a linear pressure gradient. For two weather stations with their respective altitudes above sea level,  $h_1$  and  $h_2$ , that are simultaneously recording the values  $P_1$  and  $P_2$  for the barometric pressure, respectively, a correction for the measurement results can be applied:

$$\tilde{P}_2 = P_2 - (h_2 - h_1) \frac{\Delta P}{\Delta h}. \quad (4.2)$$

Here,  $\Delta P/\Delta h$  denotes the air pressure gradient and  $\tilde{P}_2$  is the air pressure measured by weather station 2, corrected for the difference in altitude of station 1 and 2, such that it would comply with the value recorded by station 1 (within the uncertainties not related to the altitude).

The air pressure and altitude data acquired during the balloon-based measurements are shown in Fig. 4.8. Again, only the most recent data set for each month has been used. To determine a value for the linear pressure gradient, a linear regression fit is applied to the data. The resulting values for each month are listed in Tab. 4.3. The mean air pressure gradient can be estimated as the average of the gradient values obtained for all months:

$$\Delta P/\Delta h = (-87 \pm 1) \cdot 10^{-3} \text{ hPa/m.}$$

## 4.4. Ideal Gas Approximation

In the *homosphere*, which includes the *troposphere* (up to altitudes of about 10 km) and the *planetary boundary layer* (typically 100 m to 1000 m in thickness), the turbulent diffusion processes cause the atmosphere to be homogeneous. As a consequence, the molar mass of dry air in this region can be considered constant [Kei09]. Therefore, the atmosphere can be treated as an ideal gas and its density can be estimated from

$$\rho \approx \frac{PM_{\text{air}}}{RT}, \quad (4.3)$$

with  $P$  being the instantaneous barometric pressure and  $T$  the temperature of the air;  $R$  denotes the universal gas constant and  $M_{\text{air}}$  the molar mass of air.

Results from radiosonde measurements can be used to verify the assumption that the ideal gas law is a valid approximation for the air density in the lower atmosphere layers.



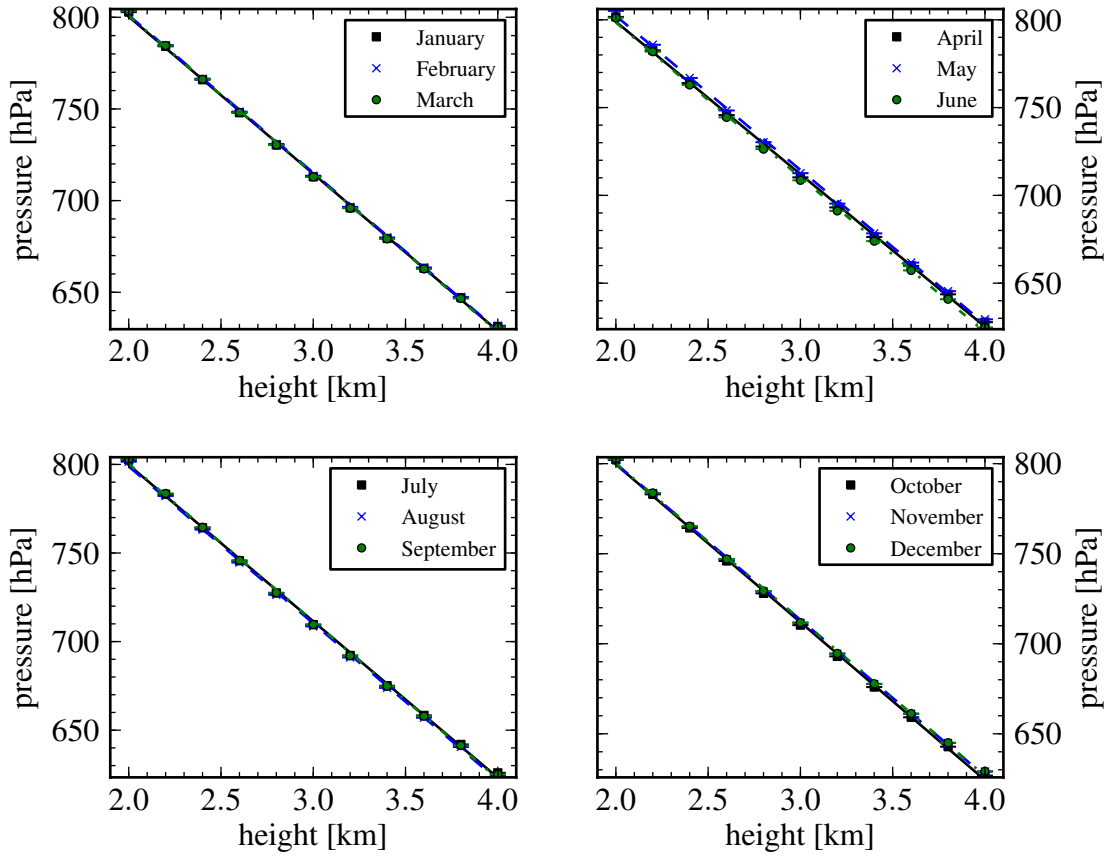


**Figure 4.8.:** Monthly profiles of air pressure vs. altitude, as measured by balloon-borne radio sounding devices during exploratory campaigns.

	monthly profile					
	Jan	Feb	Mar	Apr	May	Jun
$\Delta P/\Delta h$ [hPa/km]	-85.7	-85.9	-86.2	-86.9	-87.8	-88.1
	Jul	Aug	Sep	Oct	Nov	Dec
$\Delta P/\Delta h$ [hPa/km]	-88.3	-88.5	-88.9	-87.6	-86.7	-86.7

**Table 4.3.:** Results for the air pressure gradient in the lower atmospheric layers, from the linear regression fits to the monthly air pressure profiles, obtained from balloon-based measurement campaigns. The uncertainty for the pressure gradients is in the order of magnitude of 0.5 hPa/km for each of the fits.

In Fig. 4.9, the results of a comparison of measured and calculated values for the air density are plotted; data from all monthly profiles are used, only the latest measurement of each profile is taken into account. The comparison shows that the calculated values of the air density are compatible with the measured ones.

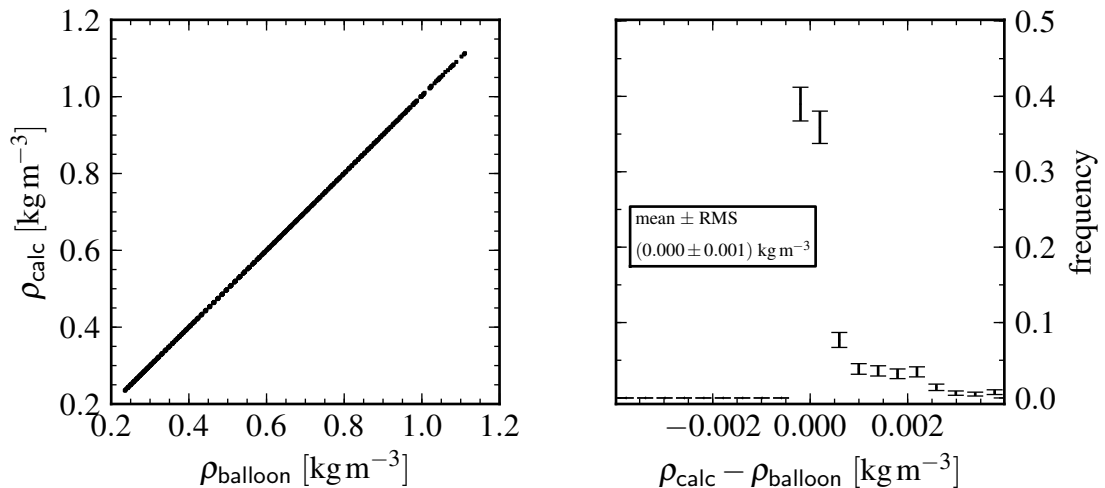


**Figure 4.9.:** Validation of the ideal gas law approximation. Data taken by balloon-borne radiosondes has been used to confirm that the air density above the Pierre Auger Observatory site is adequately described by the ideal gas law. *Left:* Correlation of the air densities actually measured by the radiosondes with those calculated from the measured values of the air pressure and temperature. *Right:* Deviation of the calculated values of the air density from the actually measured values.

## 4.5. Temperature Information from SD Stations

Most of the stations of the surface detector array are equipped with six temperature sensors each. The temperatures of the batteries are monitored by two sensors, the electronics box also contains a sensors of its own. In addition, the temperature at the base of each of the three photomultiplier tubes (PMTs) is recorded by the local station electronics. Also, provisions are made in the monitoring system to measure the water temperature; however, the corresponding sensor hardware is not installed in most cases.

Monitoring data, which include the temperature information from internal sensors, are taken in intervals of 400 seconds. Unfortunately, no data concerning environmental conditions, like e.g. the ambient temperature are recorded.

### 4.5.1. Precision of Temperature Sensors

Temperature sensors, installed as part of the internal monitoring equipment in each surface detector station, were not designed for precise measurements. In particular, they were not intended to be used for measurements of ambient temperatures at all. Therefore, in order to infer this type of information from the sensors, their characteristics, especially the precision of the temperature measurement, have to be determined.

For this purpose, the temperature information recorded by station pairs, i.e. surface detector stations which are located at a distance of only 11 m from one another are considered. Each time temperature data is available from both of the stations belonging to the respective station pair, the information is compared. The results in Fig. 4.10 are shown for the station pair consisting of the stations named *Neuquen* and *Santa Cruz*. For each of the stations, the average temperature of the bases of all active photomultiplier tubes has been determined and is taken as the temperature of the respective station. From the distribution of the temperature deviations found, the lower limit for the uncertainty of measurements of the ambient temperature can be estimated to be in the order of magnitude of  $1^\circ\text{C}$ . See Figures C.10, C.9 and C.8 for the deviations of all station pairs of the Pierre Auger Observatory.

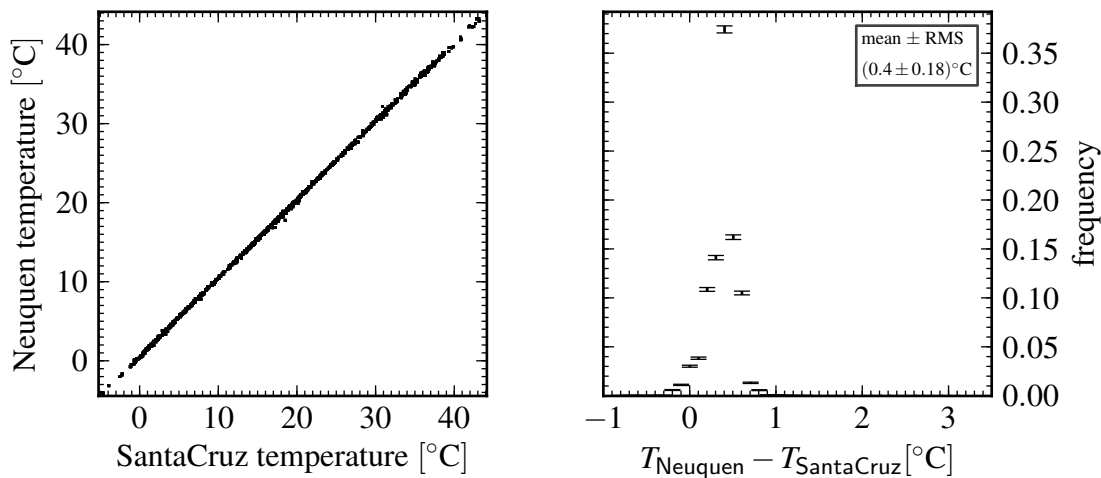


**Figure 4.10.:** Correlation and deviation of the temperatures of the photomultiplier tubes (PMTs) installed in the surface detector stations. In these diagrams, temperature data of a pair of stations, named *Neuquen* and *Santa Cruz*, located at a distance of 11 m from one another, are shown. The temperature value for each station is obtained by averaging the measurements by its sensors in the bases of the up to three (active) photomultiplier tubes. See App. C for the data measured by all pairs of SD stations. *Left:* Correlation of the temperatures measured by the two stations simultaneously. *Right:* Distribution of the instantaneous deviations of the temperatures reported by both surface detector stations at the same time.

### 4.5.2. Deconvolution of SD Station Temperatures

Due to the thermal insulation of the inner temperature sensors of a surface detector station, the temperature measured inside the tank follows any change of the ambient temperature with a certain delay. Moreover, sudden changes of the air temperature surrounding the detector station are strongly damped. The evolution of the temperature signal of a station can be considered the result of a convolution of the response function describing the station with the ambient temperature as a function of the time:

$$T_s(t) = R * T_a = \int_0^t T_a(t')R(t-t')dt' \quad (4.4)$$

Here,  $T_s(t)$  is the temperature signal of a station and  $T_a(t)$  denotes the corresponding ambient temperature at the same time;  $R(t)$  is the time response function of the detector station with respect to the temperature characteristics. If the inverse transformation of the response function, i.e.  $R^{-1}(t)$ , is known, the ambient temperature can be derived from the temperatures measured by internal sensors of a station:

$$R^{-1}(t) * T_s(t) = R^{-1}(t)R(t) * T_a(t) = T_a(t). \quad (4.5)$$

One way of obtaining the inverse transformation of the response function consists in tackling the problem in the frequency domain, where the convolution in the time domain translates into a simple multiplication [Smi97]:

$$\mathcal{F}R^{-1}(t) \cdot \mathcal{F}T_s(t) = \mathcal{F}T_a(t), \quad (4.6)$$

with  $\mathcal{F}$  being the Fourier transform operator. In the frequency domain, the inverse response function can thus be calculated via

$$R^{-1}(f) = \frac{T_a(f)}{T_s(f)}, \quad (4.7)$$

$$\text{with } R^{-1}(f) = \mathcal{F}R^{-1}(t), \quad T_s(f) = \mathcal{F}T_s(t), \quad \text{and } T_a(f) = \mathcal{F}T_a(t).$$

However, the inverse transformation of the station response function in the time domain is required for calculating the value of the ambient temperature from the temperature measured by the internal sensors of a detector station. Applying an inverse Fourier transform to the inverse frequency response function of the station yields:

$$R^{-1}(t) = \mathcal{F}^{-1}R^{-1}(f) = \mathcal{F}^{-1}\frac{T_a(f)}{T_s(f)}, \quad (4.8)$$

where the inverse Fourier transform operator is indicated by  $\mathcal{F}^{-1}$ .

Since temperature data is not taken continuously, but it is sampled in regular intervals, it suggests itself to implement the transformations from the time domain to the frequency domain (and vice versa) by means of a discrete Fourier transform (DFT) [Coo65, Pre07].

### 4.5.3. Construction of the Convolution Kernel

Temperature data, taken by both a reference weather station and the internal temperature sensors of a nearby surface detector station, can be used to construct the time response function. The weather station at the central LASER facility (CLF) is chosen as the reference weather station, since it is situated nearly in the centre of the surface detector array, and therefore it is surrounded by large number of surface detector stations. At a distance of only about 18 m from the CLF, the detector station named *Celeste* is located. It stands to reason that the ambient temperature at its location is equal to the one measured by the CLF (within the uncertainty of the measurements).

The weather stations of the **Pierre Auger Observatory** are taking temperature data at regular intervals of 300 seconds, whereas monitoring data, including the temperature information, are recorded less frequently by the detector stations, only once every 400 seconds. In order to determine the frequency response of the detector station by means of a discrete Fourier transform, both temperature data sets need to be available at the same rate. By resampling the data, this precondition can be satisfied. For that, the moving average of each data set, using a sliding window with a length of 20 minutes (the least common multiple of both time intervals), is calculated. Also, by doing so, minor gaps (less than 1200 seconds) in the acquisition of weather data are bridged.

Consecutive bins of temperature data from both sources, treated this way, are then subjected to a discrete transformation into the frequency domain. Subsamples of 1024 bins in each data set are selected for constructing the time response function. This size of the subsample is chosen for three reasons. Firstly, for sample sizes, that are integral powers of two, the DFT can be implemented using an efficient fast Fourier transform (FFT) algorithm [Coo65]. Secondly, this sample size roughly corresponds to a fortnight, during which the detector station undergoes a full temperature cycle several times. In addition, for subsample sizes much larger than 1024, the number of subsamples available rapidly decreases.

From the Fourier transformed temperature data sets, the inverse frequency response vector can be calculated, according to Eqn. 4.7. For the discrete Fourier transform, this implies dividing complex numbers, one per time bin in each data set of the selected subsamples. Subsequently, the time response vector for the inner temperature sensors of the detector station *Celeste* can be calculated, according to Eqn. 4.8. However, the time response vector cannot directly be used as a convolution kernel for obtaining information on the ambient temperature from the temperatures measured by the detector stations. The reason lies in the limited resolution of the conversion of temperature information into digital data. This conversion introduces quantisation noise [Smi97]. In addition, variations of the temperatures smaller than the resolution do not translate into different

digital values. This results in irregular components of the frequency response vector, which in turn causes artefacts of the time response vector.

Therefore, prior to using the time response vector as a convolution kernel, it has to be regularised. For a convolution kernel of length  $M$ , the time response vector has to be shifted circularly by  $M/2$  time bins, prepending the contents of the last  $M/2$  bins to the first bin. Finally, the actual convolution kernel then results from applying a *Hamming window* [Kan81, Bla59] of length  $M$  to the time response vector modified this way. The ambient temperature nearby a surface detector station can then be calculated from

$$(\bar{T}_a)_i = (K * \bar{T}_s)_i = \sum_{j=1-M/2}^{j=M/2} K_j (\bar{T}_s)_{i-j} , \quad (4.9)$$

where  $(\bar{T}_a)_i$  and  $(\bar{T}_s)_i$  denote bin  $i$  of the resampled ambient temperature and the detector station temperature, respectively. The expression  $K_i$  indicates bin  $i$  of the convolution kernel, obtained by shifting and windowing the time response vector as described above.

#### 4.5.4. Residual Temperature Uncertainty

The magnitude of deviation of the ambient temperature reconstructed from the station temperature by deconvolution depends on the length  $M$  of the convolution kernel. For small values of  $M$ , even moderately rapid changes of the ambient temperature cannot be reconstructed properly. Convolution kernels with a large  $M$  are prone to irregularities introduced due to the limited resolution of the temperature measurement. In addition, the boundary effects caused by convolving a temperature data set of length  $N$  with a convolution kernel of length  $M$  render  $M$  bins of the temperature data unusable. As a consequence, these data are not available for estimating the ambient conditions at the corresponding times, thus favouring a small value of this parameter.

In order to optimise the temperature uncertainty with respect to the parameter  $M$ , the deconvolution is applied to the station temperature data several times for different values of  $M$ . For each deconvolution result, the mean deviation of the reconstructed temperature, using temperatures measured by the Celeste station, from the actual ambient temperatures, measured by the weather station at the central LASER facility, is calculated. The results of this parameter scan can be seen in Fig. 4.11. It shows, that the optimum value for the parameter (in terms of both the remaining deviation and the kernel length) is  $M \approx 50$ , where the residual temperature uncertainty reaches a value of about  $1.5^\circ\text{C}$ .

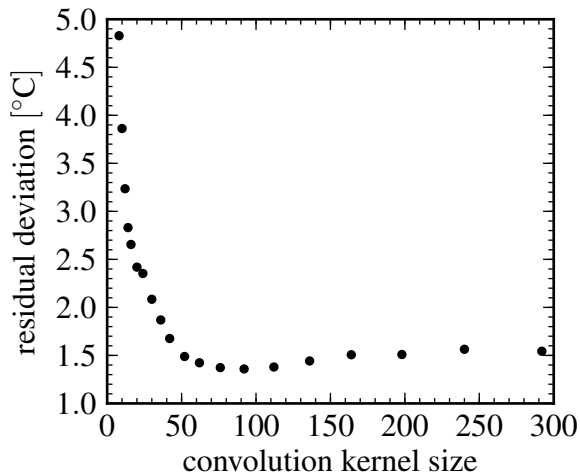


**Figure 4.11.:** Residual uncertainty of the deconvoluted station temperature, as a function of the size of the convolution kernel. The uncertainty is determined by averaging the deviation of the reconstructed ambient temperature from the one actually measured by the CLF station

## 4.6. Summary

In this chapter, the major climatic characteristics of the Pierre Auger Observatory site were investigated. An overview of the facilities on the site, providing information on the instantaneous weather conditions, was given.

The systematic effects, the facilities are subject to, were described and measurements of balloon-borne weather station equipment were exploited to reduce the deviations they are causing.

Finally, a procedure for deriving ambient temperatures from temperatures recorded by the sensors located at the bases of the photomultiplier tubes in the surface detector stations was described and its performance was evaluated. The ambient temperature can be determined at an accuracy of about  $1.5^{\circ}\text{C}$ , which is comparable to the typical measurement uncertainty of the internal temperature sensors of a surface detector station of  $\approx 1^{\circ}\text{C}$ .





# Chapter 5

## Weather Corrections

The development of an extensive air shower, as it propagates through the atmosphere, is subject to weather dependent variations. The different states of the atmosphere can be described by a set of instantaneous quantities, specifically the atmospheric pressure, the temperature of the air and its density. Since in the energy regime beyond  $\approx 100\text{TeV}$  the major characteristics of primary cosmic ray particles can only be derived by indirect means, i.e. by observing the properties of extensive air showers, it is crucial to estimate the impact of the weather conditions for precise measurements.

The surface detector of the **Pierre Auger Observatory** had been designed with a nearly 100% duty cycle as a major objective. Hidden dead times of the surface detector reduce the duty cycle to values considerably lower than 100% [Abr09a]. The fluorescence detectors of the observatory, on the other hand, are only operative during about one tenth of the duty cycle of the SD. This deficiency, however, is compensated for by the lower energy required for fully efficient operation. In hybrid mode, i.e. in a joint operation with the surface detector, nearly all extensive air showers are detected for primary particle energies exceeding 1 EeV. Since the joint data taking limits the number of events recorded in a specific time period to the capabilities of the FD, the surface detector alone still outperforms the fluorescence detector as well as the hybrid detector with respect to the number of air shower events recorded.

Therefore, in this chapter the impact of the instantaneous weather conditions on the quantities measured by the surface detector are investigated. In order to be able to make use of air shower data at energies, at which the detector is not fully efficient, strategies for compensating the weather impact are established.

### 5.1. Atmospheric Effects on EAS

From the quantities characterising the state of the Earth's atmosphere, the pressure  $P$  and the density  $\rho$  of the air are the properties, which most notably are affecting the development of extensive air showers.

Assuming that the weather conditions do not impact the development of extensive air showers, the number of events recorded by the surface detector array is expected to follow, within the limits imposed by the statistical uncertainty, the evolution of the integrated exposure of the detector as it is shown in Fig. 5.1. The number of events in a particular period of time is then not expected to be correlated to any weather observable. The compatibility of two distributions can be tested by means of a quantile–quantile plot [Zey06]. Several quantiles of the distributions to be compared are plotted against one another. For compatible distributions, the plot is expected to result in a straight line. In the case of the distributions of the event rates and the air densities, Fig. 5.2 suggests, that they are substantially compatible and hence that the event rate depends on the weather situation. At the same time, the systematic deviations from the reference line indicate, that the event rate is not only subject to modulations caused by air density variations.

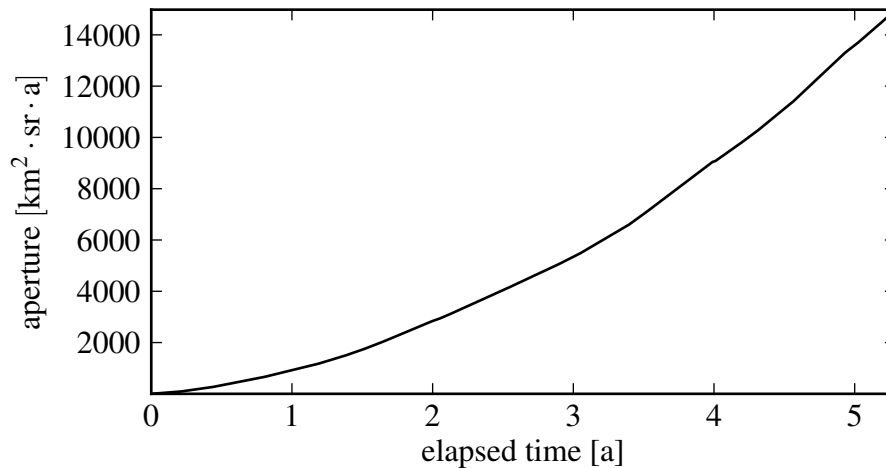


**Figure 5.1.:** Aperture of the SD (Surface Detector) vs. the time elapsed since the beginning of the data taking. Line segments of non-linear increase are due to the growth of the detector array during the data taking period as well as due to time periods of degraded performance. The uncertainty of the integrated aperture amounts to about 1.5% [Abr09a].

A detailed discussion of the underlying effects, in particular with respect to the surface detector of the Pierre Auger Observatory, is presented in [Abr09b]. In this section, the main statements of that work are briefly summarised.

### 5.1.1. Sensitivity of the SD (Surface Detector)

The surface detector stations of the Pierre Auger Observatory, implemented as water Čerenkov detectors, are capable of detecting both the muonic and the electromagnetic component of extensive air showers. As a consequence, the impact of varying weather

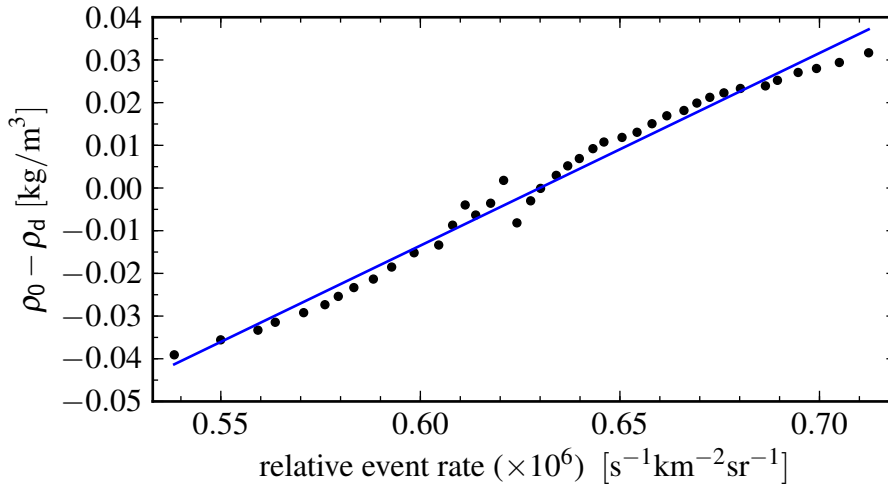


**Figure 5.2.:** Quantile–quantile plot for the distributions of the air densities and the event rates. The air densities are actually the deviations from the mean air density, they are averaged on a time scale of one day. The event rate is divided by the aperture of the detector. The solid, blue reference line indicates the case of identical distributions. Data from January 1, 2004, until April 15, 2009, is used for this diagram.

conditions on both constituents has to be taken into account to quantify their overall impact. In the following, the contributions of the air pressure and the density of the air are described separately.

### 5.1.2. Variations of the Atmospheric Pressure

The pressure is a measure of the vertical air column density above ground. For higher values of the air pressure (as compared to the mean value), the larger amount of matter overburden causes an air shower to be older when it approaches the observation level. That is, the maximum particle number in the air shower is already reached at higher altitudes, corresponding to a lower value of the atmospheric depth  $X_{\max}$ . However, this does not significantly affect the muons because there is no pronounced maximum of the corresponding shower size (see Section 2.2); thus, the number of muons nearly does not exhibit a dependence on the pressure of the air at all. The electromagnetic component, on the contrary, is exponentially attenuated beyond its maximum. For this reason, a systematic shift of the signals recorded by the water Čerenkov detectors is expected, depending on the instantaneous air pressure.

The longitudinal profile of air showers can be parametrised by the Gaisser–Hillas function [Gai78]; see Fig. 5.3 for an illustration. For the surface detector stations of the Pierre Auger Observatory, the signal at 1000 m from the air shower core position is the relevant quantity for the energy reconstruction. At this distance, the electromagnetic

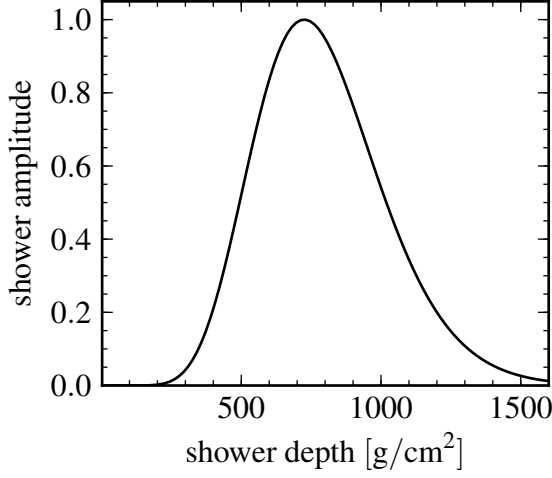


**Figure 5.3.:** Typical longitudinal profile of an extensive air shower, parametrised by the Gaisser–Hillas function. In this case, the position of the air shower maximum is chosen to be at  $X_{\max} = 725 \text{ g/cm}^2$ .

component of the total signal can be written as

$$S_{\text{em}}(E, X) \propto X^{\tilde{X}_{\max}/\Lambda} e^{(\tilde{X}_{\max}-X)/\Lambda}, \quad (5.1)$$

where

$$\Lambda \approx 100 \text{ g/cm}^2, \quad \tilde{X}_{\max} = X_{\max} + \Delta, \quad \Delta \approx 150 \text{ g/cm}^2, \quad (5.2)$$

with  $E$  being the primary particle energy,  $X$  the slant depth,  $X_{\max}$  the shower maximum,  $\tilde{X}_{\max}$  the corresponding value at a distance of 1000 m from the shower core;  $\Delta$  denotes its typical shift. The parameter  $\Lambda$  is the effective attenuation length beyond the shower maximum. The position of the air shower maximum  $X_{\max}$  can be approximated from measurements of the elongation rate, i.e. the change of  $X_{\max}$  per decade in the energy [Abr10b]:

$$X_{\max} = X_{E_0} + \begin{cases} d_{10} \log E/E_0, & E < E_0 \\ D_{10} \log E/E_0, & E > E_0 \end{cases} \quad (5.3)$$

with  $E_0 \approx 2 \text{ EeV}$ ,  $X_{E_0} \approx 715 \text{ g/cm}^2$ ,  $d_{10} \approx 88 \text{ g/cm}^2$ , and  $D_{10} \approx 47 \text{ g/cm}^2$ . Since an infinitesimal change of the pressure directly translates into a variation of the slant depth according to

$$dX = \frac{dP}{g \cos \theta}, \quad (5.4)$$

where  $g$  is the acceleration of gravity constant and  $\theta$  is the zenith angle of the air shower arrival direction, the relative deviation of the electromagnetic signal due to a change of the atmospheric pressure can be estimated by:

$$\frac{dS_{\text{em}}}{S_{\text{em}}} \approx \xi_{\text{em}} dP \quad \text{with} \quad \xi_{\text{em}} = \frac{\sec \theta}{g \Lambda} \left( \frac{\tilde{X}_{\max}}{X} - 1 \right), \quad (5.5)$$

where  $X = X_{\text{PAO}} \sec \theta$  with  $X_{\text{PAO}} \approx 880 \text{ g/cm}^2$  being the atmospheric depth of the Pierre Auger Observatory site.

### 5.1.3. Variations of the Atmospheric Density

The lateral distribution of the electromagnetic component of extensive air showers can be described, in good approximation, by the NKG (Nishimura–Kamata–Greisen) function [Gre56, Kam58]; see Fig. 5.4 for an illustration. At large distances from the air shower core, the expression for the electromagnetic signal component simplifies to

$$S_{\text{em}} \propto r^{-\eta} r_{\text{M}}^{\eta-2} \quad \text{with} \quad \eta \approx 6.5 - 2s \quad \text{and} \quad s = \frac{3X}{X + 2X_{\text{max}}}, \quad (5.6)$$

where  $s$  denotes the age of the air shower (see Section 2.2) and  $r$  is the distance from the shower core. Again,  $X = X_{\text{PAO}} \sec \theta$  for the observation level at the Pierre Auger Observatory site. The Molière radius  $r_{\text{M}}$  is given by

$$r_{\text{M}} = \frac{E_s X_0}{E_{\text{crit}} \rho}, \quad (5.7)$$

with  $E_{\text{crit}} \approx 84.2 \text{ MeV}$  being the critical energy,  $X_0 \approx 37.1 \text{ g/cm}^2$  is the radiation length (in air);  $E_s \approx 21 \text{ MeV}$  corresponds to the mean energy loss due to multiple Coulomb scattering. An increase of the air density  $\rho$  causes the Molière radius to become smaller. As a consequence, the electromagnetic signal component  $S_{\text{em}}$  is also affected by variations of  $\rho$  (by way of Eqn. 5.6). Here, an infinitesimal change of the atmospheric density translates into a relative signal departure:

$$\frac{dS_{\text{em}}}{S_{\text{em}}} \approx \frac{d\rho}{\rho} (2 - \eta). \quad (5.8)$$

Although the major impact on the electromagnetic signal amplitude stems from the variation of the Molière radius about two radiation lengths above ground level [Gre56], corresponding to an altitude of about 700 m for vertical incidence in the case of the Pierre Auger Observatory site, it shows that this is closely related to the situation at ground level. In the lower atmospheric layer, the long-term temperature gradient (in the time scale of days up to a season) amounts to about  $5.5 \text{ }^\circ\text{C/km}$ . On the short-term (in a time scale of hours), the temperature gradient undergoes a change, causing the diurnal variation of the temperature (and thus the density) at two radiation lengths above ground to show a weaker correlation to the ground temperature. Since the air temperatures are roughly linked to the air density via the ideal gas equation, the atmospheric density can be derived from the ground temperature by taking the temperature gradient into account. As the short-term characteristics differ considerably from those in the long-term, a separate ansatz for both time scales is self-evident. The overall variation of the electromagnetic

signal component, caused by a change in atmospheric density, can therefore, in a simple model, be written as

$$dS_{\text{em}} = S_{\text{em}}^0 [\alpha_{\text{em}}(\rho_{\text{d}} - \rho_0) + \beta_{\text{em}}(\rho - \rho_{\text{d}})]. \quad (5.9)$$

Here,  $\alpha_{\text{em}}$  denotes the coefficient describing the impact of the long-term effect, whereas  $\beta_{\text{em}}$  is the coefficient for the short-term effect. By averaging the atmospheric depth over the whole data taking period,  $\rho_0$  is obtained;  $\rho_{\text{d}}$  is the running mean in a time scale of a day. The coefficient  $\beta_{\text{em}}$  is expected to be considerably smaller than  $\alpha_{\text{em}}$ , because the amplitude of the air density variations decreases with increasing altitude according to

$$d\rho(h) = d\rho(0)e^{-h/700\text{m}}, \quad (5.10)$$

in the case of the Pierre Auger Observatory site, with  $h$  being the altitude above ground; for the density dependence of the lateral distribution of secondary particles, the relevant value is  $h \approx 700\text{m} \cdot \cos\theta$ . Hence, the ratio of  $\beta_{\text{em}}$  and  $\alpha_{\text{em}}$  should be in the order of magnitude of:

$$\frac{\beta_{\text{em}}}{\alpha_{\text{em}}} \approx e^{-\cos\theta}. \quad (5.11)$$

Generally, the varying atmospheric density is expected to impact the lateral development of the muon component in a similar way, however, to a lesser extent. Air shower simulations [Abr09b] yield values for the corresponding coefficients compatible with a vanishing signal variation, though.

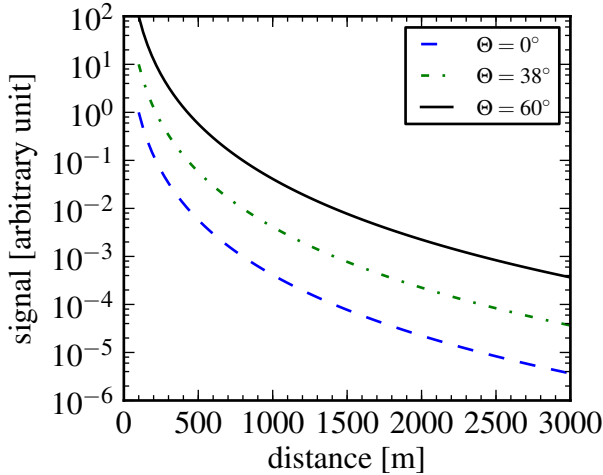


**Figure 5.4.:** Typical lateral air shower profile, parametrised by a NKG-type LDF (Lateral Distribution Function), vs. the distance from the air shower core position. The lateral profile is shown for different values of the zenith angle  $\Theta$ . For the sake of clarity, the signals have been scaled with different factors.

#### 5.1.4. Impact on $S_{1000}$

Because it is mainly the electromagnetic shower component, which is subject to variations caused by the instantaneous weather conditions, the fraction of the total signal it accounts

for has to be known to estimate the impact on the reconstructed signal at a distance of 1000 m, i.e.  $S_{1000}$ . According to [Abr09b], the electromagnetic fraction, hereafter denoted by  $F_{\text{em}}$ , can be inferred from simulations of extensive air showers. However, this implies an uncertainty of  $F_{\text{em}}$  caused by both the hadronic interaction model used in the simulation and the cosmic ray composition adopted. Using a set of simulated air showers with a proton as the primary particle, a parameterisation of  $F_{\text{em}}$  can be obtained:

$$F_{\text{em}} \approx F_{\text{em}}^0 + \frac{1 - \sec \theta}{2}. \quad (5.12)$$

The electromagnetic fraction for vertical incidence,  $F_{\text{em}}^0$ , varies between approximately 0.65 (for  $E \approx 1 \text{ EeV}$ ) and 0.7 (for  $E \approx 10 \text{ EeV}$ ). It can roughly be parametrised as [Ble09]:

$$F_{\text{em}}^0 \approx 0.7 + 0.035 \left( \log \frac{E}{\text{EeV}} - 1 \right). \quad (5.13)$$

The dependence of the electromagnetic signal fraction on the zenith angle and the primary particle energy is shown in Fig. 5.5 for the approximation defined by Eqn. 5.12 and Eqn. 5.13.

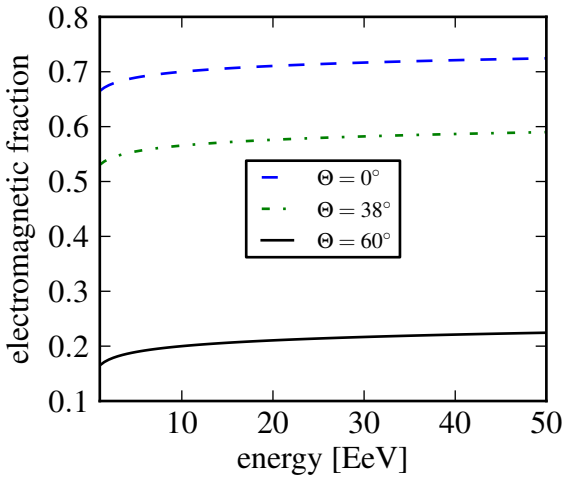


**Figure 5.5.:** Fraction of the signal measured by a surface detector station of the Pierre Auger Observatory, caused by the electromagnetic air shower component. The fraction is plotted for different values of the zenith angle  $\Theta$ . The approximation provided by Eqn. 5.12 and Eqn. 5.13 is used for this diagram.

Exploiting Equations 5.5, 5.9, and 5.12, the deviation of  $S_{1000}$  can be written as:

$$dS_{1000} = S_{1000}^0 F_{\text{em}} [\xi_{\text{em}}(P - P_0) + \alpha_{\text{em}}(\rho_d - \rho_0) + \beta_{\text{em}}(\rho - \rho_d)], \quad (5.14)$$

where  $S_{1000}^0$  denotes the signal that would be measured if no weather effects were affecting the shower development. Consequently, an estimate for  $S_{1000}^0$  can be inferred from the result of the reconstruction procedure, which determines a value for  $S_{1000}^{\text{reco}}$ , usually by fitting a lateral distribution function (LDF) to the signals measured by surface detector stations around the air shower core position. Eventually, the model described above

yields:

$$S_{1000}^0 \approx \frac{S_{1000}^{\text{reco}}}{F_{\text{em}}} [F_{\text{em}}^{-1} + \xi_{\text{em}}(P - P_0) + \alpha_{\text{em}}(\rho_d - \rho_0) + \beta_{\text{em}}(\rho - \rho_d)]^{-1}. \quad (5.15)$$

### 5.1.5. Impact on the Event Rate

For air shower events causing a signal in excess of the trigger threshold  $S_{\text{thr}}$  at 1 km from the shower core position, the number of events per unit time, i.e. the trigger rate, per unit solid angle in a zenith angle bin  $d\theta$  can be expressed by

$$\frac{dR}{d\theta} = \frac{dA}{d\theta} \int_{S_{\text{thr}}} dS_{1000} P_{\text{tr}}(S_{1000}) \frac{d\Phi}{dS_{1000}}, \quad (5.16)$$

where  $A$  is the geometrical aperture,  $\Phi$  the flux of the cosmic radiation, and  $P_{\text{tr}}$  the probability for triggering the surface detector array, depending on the signal strength  $S_{1000}$ . For the surface detector array of the Pierre Auger Observatory, the signal  $S_{1000}$  is converted into a reconstruction estimate for the energy of the primary particle according to

$$E \propto (S_{1000})^B, \quad (5.17)$$

with  $B$  resulting from the energy calibration using data recorded by the FD telescopes of the observatory [Abr08]. This calibration of the SD energy scale by means of FD data is substantially independent of the peculiarities of any underlying hadronic interaction models. By applying Eqn. 5.17 to Eqn. 5.15, the corresponding energy correction can be calculated, yielding an estimate for the primary energy  $E_0$ , i.e. the value obtained by compensating for the weather impact. Taking into account that the flux  $\Phi$  essentially follows a power law ( $d\Phi/dE \propto E^{-\gamma}$ ), the differential flux can be written as follows:

$$\frac{d\Phi}{dS_{1000}} \propto E_0^{-\gamma} \frac{dE_0}{dS_{1000}} \propto S_{1000}^{-B\gamma+B-1} [1 + \xi(P - P_0) + \alpha(\rho_d - \rho_0) + \beta(\rho - \rho_d)]. \quad (5.18)$$

Here, the dependence of the parameters on the energy are neglected. By means of Eqn. 5.16, the rate per zenith angle bin can finally be written as:

$$\frac{dR}{d\theta} \propto [1 + \tilde{\xi}(P - P_0) + \tilde{\alpha}(\rho_d - \rho_0) + \tilde{\beta}(\rho - \rho_d)], \quad (5.19)$$

with  $\tilde{\xi} = (\gamma - 1)F_{\text{em}}B\xi_{\text{em}}$ ,  $\tilde{\alpha} = (\gamma - 1)F_{\text{em}}B\alpha_{\text{em}}$ , and  $\tilde{\beta} = (\gamma - 1)F_{\text{em}}B\beta_{\text{em}}$ .

### 5.1.6. Determination of the Parameters $\tilde{\xi}$ , $\tilde{\alpha}$ and $\tilde{\beta}$

The parameters  $\tilde{\xi}$ ,  $\tilde{\alpha}$  and  $\tilde{\beta}$  have been determined in basically the same way as proposed in [Abr09b], but for the events of the data taking period from January 1, 2004, until



April 15, 2009. The set of parameters is fitted in such a way, that the expected rate of events matches the measured rate best. The parameter values are given in Tab. 5.1. The log-likelihood fit results in a reduced  $\chi^2$  of 1.13 in this case.

parameter	value	uncertainty
$\tilde{\xi}$ [hPa <sup>-1</sup> ]	$-3.0 \cdot 10^{-3}$	$2 \cdot 10^{-4}$
$\tilde{\alpha}$ [kg <sup>-1</sup> m <sup>3</sup> ]	-1.94	0.04
$\tilde{\beta}$ [kg <sup>-1</sup> m <sup>3</sup> ]	-0.57	0.04

**Table 5.1.:** Results of a log-likelihood fit of the expected number of events per unit time to the number of air shower events measured by the detector in the same time period. The fit results correspond to a reduced  $\chi^2$  of 1.13 for data from January 1, 2004, until April 15, 2009.

## 5.2. Impact on Zenith Angle Distributions

As long as the trigger conditions of the surface detector array of the **Pierre Auger Observatory** are still fulfilled despite any weather related signal degradation, the loss in signal strength can be compensated for using the method described in [Abr09b]. By exploiting the signal/energy conversion relation (Eqn. 5.17), the deviation of the reconstructed energy with respect to the energy of the primary cosmic ray particle can be corrected for as well. This is certainly possible for primary particle energies, at which the detector array is nearly fully efficiently recording every air shower event. For the surface detector array of the **Pierre Auger Observatory**, this corresponds to an energy of 3 EeV, where the efficiency is at the level of 97% [Abr09a]. In this case, the modulation of the signal due to varying weather conditions is negligible as compared to the total signal strength and does therefore not noticeably reduce the detection probability.

In contrast, the variations of the signals become decisive for energies far below 3 EeV. Apart from shower-to-shower fluctuations and any statistical uncertainty of the signal detection, an extensive air shower might be detected for one set of weather observables. For a significantly different weather condition, a comparable extensive air shower, however, might not trigger the SD (Surface Detector), even for primary cosmic rays arriving from the same direction at the same energy of the primary particle.

This effect can affect the search for a small scale anisotropy in the arrival directions of cosmic rays, at least at energies far below the level required for a fully efficient detection. In this case, an anisotropy signal might be found to stand out against an isotropic background radiation in one season of the year, while in another season the anisotropy signal virtually vanishes. In particular, inclined air showers, i.e. those which are initiated by cosmic ray particles at large zenith angles (close to 60° and beyond), are expected to

be significantly subject to weather effects due to the attenuation they suffer on their way to the detector.

As a consequence of the dependence of the trigger probability on the instantaneous weather situation, the zenith angle distributions are also expected to differ depending on the set of weather observables. Therefore, in this section a method for a compensation of this effect, especially targeted at the search for a small scale anisotropy at low energies, is presented.

### 5.2.1. Dataset

For this analysis, air shower event data from the *CDAS Herald repository* are used. Only events recorded from January 1, 2004, until April 15, 2009, are taken into account. All events have to satisfy the standard cuts, i.e. the T5 trigger condition has to be fulfilled, the reconstruction of the events has to be successful, and the reconstructed zenith angle must not exceed  $60^\circ$ . In addition, event data acquired during time periods of degraded detector performance are discarded. The CIC (Constant Intensity Cut) energy estimation of the reconstructed air showers are used.

Data taken by the CLF (Central LASER Facility) (as described in Chap. 4) were also used to obtain information on the instantaneous weather conditions for each event.

### 5.2.2. Lowest Energy Cut

In order to define the lowest energy cut for this analysis, the energy spectrum of the events, as they are recorded by the surface detector of the *Pierre Auger Observatory*, is evaluated. The first derivative (with respect to the reconstructed energy) of this spectrum is shown in Fig. 5.6. At an energy of 0.35 EeV, a steep decrease is seen. At this point, the slope of the energy spectrum of the cosmic radiation starts to outperform the increasing detection probability for extensive air showers. Therefore, a value of 0.5 EeV is chosen as the lowest energy to be considered in the analysis at hand.

### 5.2.3. Selection of a Subsample Cut Parameter

Because in this analysis, a method for the compensation of the deviations of the zenith angle distributions for different sets of weather observables shall be established, cut parameters for the selection of subsamples are to be defined first.

Taking into account, that the variations of the air pressure on the site of the *Pierre Auger Observatory* are at the level of 0.5% on average only (see Chap. 4), this quantity is not a suitable cut parameter. This is also supported by the small value for  $\tilde{\xi}$  in Tab. 5.1, which also suggests that its impact on the surface detector signals is small.

The larger variations of the air density (again according to Chap. 4) suggest that this quantity may be used as a criterion for the selection of subsamples. Also, the values for

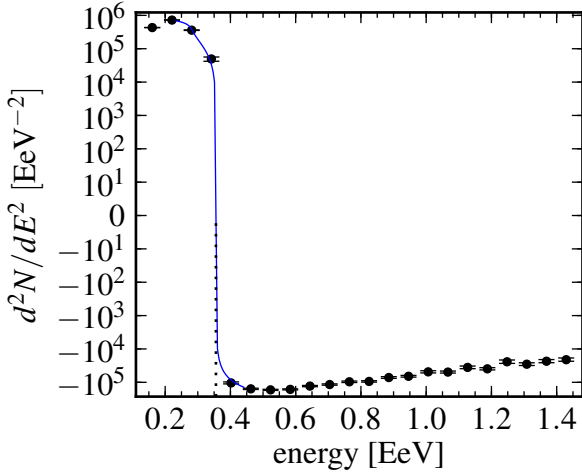


**Figure 5.6.:** First derivative of the differential energy spectrum of the events recorded by the surface detector array. The dotted line indicates the energy, at which the slope of the cosmic ray energy spectrum starts to prevail over the increase in detection efficiency.

$\tilde{\alpha}$  and  $\tilde{\beta}$  in Tab. 5.1 indicate, that the instantaneous air density significantly impacts the the actual signal strength in the surface detector stations at ground level.

Since the variations of the air pressure  $P$  are negligible as compared to those of the air density  $\rho$ , and since  $\rho \propto P/T$  holds (as shown in Chap. 4), the air temperature at ground level can be considered a suitable selection criterion as well.

In the following, two temperatures,  $T_{lo}$  and  $T_{hi}$ , are determined. Here,  $T_{lo}$  defines the upper limit for the temperature associated with the events in one subsample. Accordingly,  $T_{hi}$  is the lower temperature associated with the events in a second subsample. Both subsamples shall be disjoint subsets of the full event set.

#### 5.2.4. $\chi^2$ Maximisation

The temperatures  $T_{lo}$  and  $T_{hi}$  are determined in such a way, that the disagreement of the corresponding subsamples is maximised with respect to their zenith angle distributions. That is, values for  $T_{lo}$  and  $T_{hi}$  are found, which minimise the probability of the zenith angle distributions for being compatible. For that purpose, histograms of the zenith angles are created for each subsample. A two-sample  $\chi^2$  test statistic [Hec03] is then calculated from both histograms:

$$\chi^2 = \sum_{i=1}^M \frac{\left( R_{lo/hi} n_i^{(hi)} - n_i^{(lo)} / R_{lo/hi} \right)^2}{n_i^{(hi)} + n_i^{(lo)}}. \quad (5.20)$$

Here,  $M$  is the number of bins in each histogram; it is chosen to be 60 to form zenith angle bins of  $1^\circ$ . The number of entries in bin  $i$  is denoted by  $n_i^{(lo)}$  for events at temperatures  $T$  below  $T_{lo}$ . Accordingly,  $n_i^{(hi)}$  denotes bin  $i$  for events at temperatures exceeding  $T_{hi}$ .

The factor  $R_{lo/hi}$  is defined by:

$$R_{lo/hi} = \sqrt{\frac{N_{lo}}{N_{hi}}} \quad \text{with} \quad N_{lo} = \sum_{i=1}^M n_i^{(lo)} \quad \text{and} \quad N_{hi} = \sum_{i=1}^M n_i^{(hi)}.$$

A value for  $R_{lo/hi}$  close to unity is advantageous, since in this case both subsamples contain approximately the same amount of events and thus they are subject to statistical fluctuations to about the same extent. The parameter space, spanned by the temperatures  $T_{lo}$  and  $T_{hi}$ , is scanned in steps of 0.5 K, with the side condition  $T_{lo} \leq T_{hi}$ . The result of the scan is shown in Fig. 5.7. As can be seen from the diagram, the zenith angle distribution for  $T > T_{hi}$  and  $T < T_{lo}$  disagree maximally for both temperature cuts around the median temperature  $T_{med} \approx 285.3$  K, calculated from the complete set of event data. Therefore,  $T_{hi} = T_{lo} = T_{med}$  is chosen for the cuts to define the event subsamples to be used in the following. This configuration also implies  $R_{lo/hi} = 1$ .

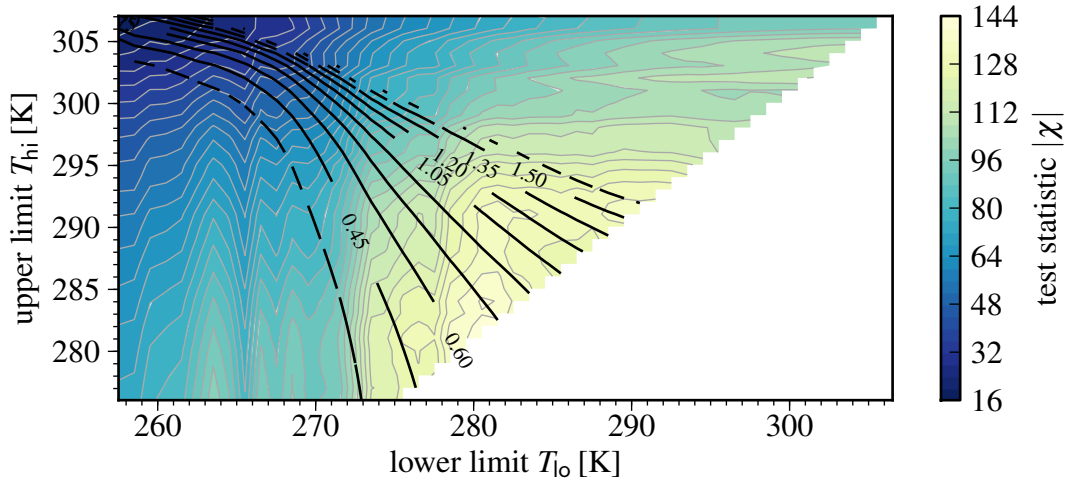


**Figure 5.7.:** Results of the maximisation for a two-sample  $\chi^2$  test statistic, calculated from the zenith angle distributions of two disjoint subsamples of surface detector events. The subsamples contain SD events, for which the instantaneous ambient temperature  $T$  falls below  $T_{lo}$ , and for which  $T$  exceeds  $T_{hi}$ , respectively; for the temperature limits, the inequality  $T_{lo} \leq T_{hi}$  holds. The square root of the  $\chi^2$  values for all valid combinations of  $T_{lo}$  and  $T_{hi}$  are represented by filled contours in the background of the diagram. The contour lines in the foreground correspond to the value of  $R_{lo/hi} = \sqrt{N_{lo}/N_{hi}}$ , where  $N_{lo}$  is the number of SD events, for which  $T < T_{lo}$ , and  $N_{hi}$  is the number of events, for which  $T > T_{hi}$ , respectively.

In Fig. 5.8, the zenith distributions for the two subsamples selected this way are shown for an energy threshold of 0.5 EeV. The difference of the numbers of entries in each zenith angle bin is plotted as well. For nearly the full range of the zenith angles, a systematic shift of the differences can be seen, corresponding to the disagreement of the zenith angle

distribution in the two-sample  $\chi^2$  test.

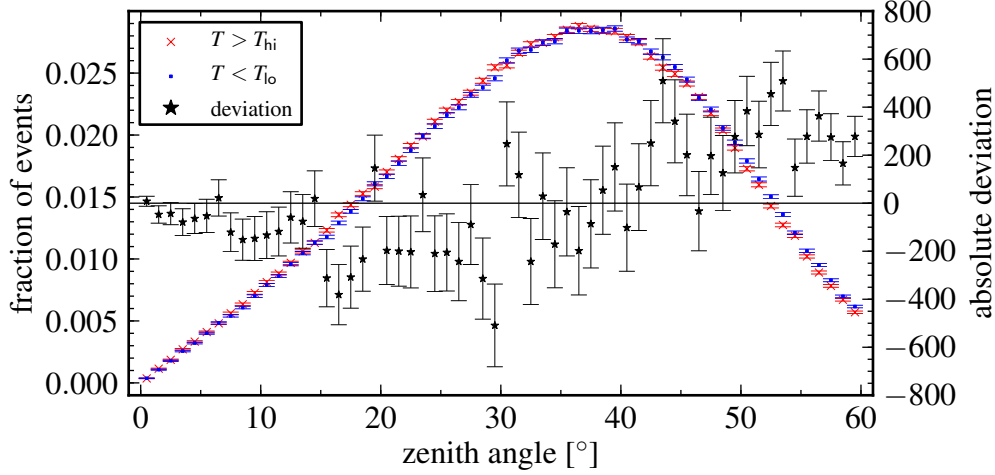


**Figure 5.8.:** Zenith angle distributions for high temperatures ( $T > T_{hi}$ ) and low temperatures ( $T < T_{lo}$ ), respectively, with  $T_{hi} = T_{lo} = T_{med}$ ;  $T_{med} \approx 285.3\text{K}$  denotes the median temperature of the surface detector events. The fraction of events in the corresponding zenith angle bin is plotted, using cross and dot markers, for both subsamples (ordinate on the left-hand side). The star shaped markers indicate the absolute deviation of the numbers of events in both subsamples for each zenith angle bin (ordinate on the right-hand side).

### 5.2.5. Ansatz for a Compensation

There is no way of recovering extensive air shower events that do not satisfy the minimum requirements for a surface detector trigger condition. This is still true even if the air shower event is lost simply because of the instantaneous weather conditions causing additional attenuation.

In most analyses of extensive air shower data, an energy cut is usually applied towards the lower end of the energy spectrum to exclude low energy events from being analysed. In searches for point source candidates this is often done to narrow the energy range to the region of interest.

According to Eqn. 5.17, a lower energy cut  $E_{lo}$  translates into a corresponding value of the signal strength  $S_{1000}^{(lo)}$  at a distance of 1000 m from the air shower core position. Conversely, the signal loss  $dS_{1000}$  caused by the instantaneous state of the atmosphere translates the intended energy cut  $E_{lo}$  into an actual energy cut  $E_{lo} + dE$  that depends on the weather situation.

In order to ensure the compatibility of the zenith angle distributions regardless of the

current atmospheric state, the intended energy cut  $E_{lo}$  can be replaced by

$$\tilde{E}_{lo} = E_{lo} + E_{mod}, \quad (5.21)$$

where  $E_{mod}$  depends on the weather observables and it is to be adjusted such that it outweighs the effect of  $dE$ .

The ansatz

$$E_{mod} = C_E p_E F_{em} (4s - 9) \frac{\rho_d - \rho_0}{2\rho_0}, \quad (5.22)$$

with

$$F_{em} = \left[ 0.7 + 0.035 \left( \log \frac{E}{\text{EeV}} - 1 \right) \right] - \frac{\sec \Theta - 1}{2}, \quad C_E = 1 \text{ EeV}, \quad \text{and} \quad s = \frac{6}{2 + 3 \cos^2 \Theta}$$

resembles the expressions given in Section 5.1 for the signal variation due to a change of the air density. The values for the zenith angle  $\Theta$  and the energy  $E$  are those of the individual reconstructed extensive air showers, to which the energy cut is to be applied. The value  $\rho_d$  is the running mean of the air density in a time scale of a day, sampled at the times of the individual events, whereas  $\rho_0$  is the overall mean air density. The air density on a diurnal scale is not taken into account, because the determination of the correction succeeds already using the running mean of the air density alone and no further improvement can be achieved due to the statistical uncertainty of the zenith angle reconstruction.

To properly align the zenith angle distributions by making use of the weather information, the only free parameter  $p_E$  has to be adjusted accordingly.

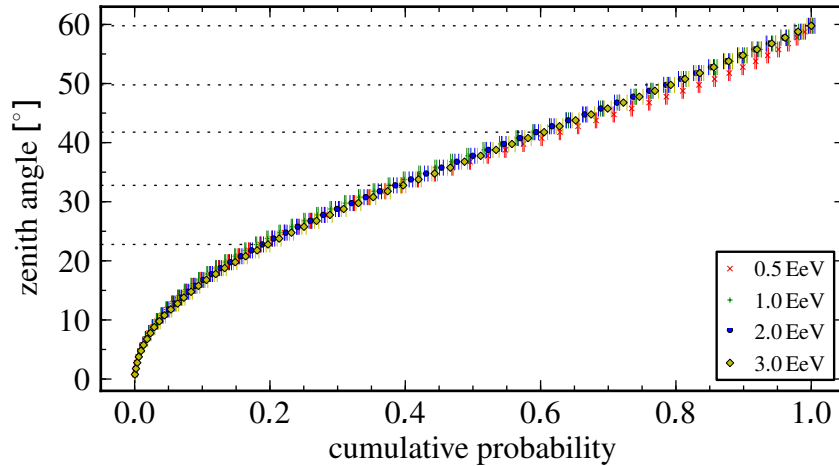


**Figure 5.9.:** Zenith angles vs. cumulative probability for different values of the lower energy cut.

probability $P_i$	0.2	0.4	0.6	0.8	1.0
zenith angle $\Theta_i$	23	33	42	50	60

**Table 5.2.:** Zenith angles and associated cumulative probabilities. The zenith angles  $\Theta_i$  are determined in such a way, that  $P_i$  is the associated cumulative probability for an air shower event to be detected at a zenith angle smaller than  $\Theta_i$ .

### 5.2.6. Parameter Estimation for $p_E$

Apart from the impact of the weather, the mean zenith angles of both event subsamples are expected to be compatible within the bounds of their statistical uncertainties. Therefore, the function

$$\Delta\bar{\Theta} = |\bar{\Theta}_{lo} - \bar{\Theta}_{hi}| = \left| \frac{1}{N_{lo}} \sum_{i=1}^{N_{lo}} \Theta_i^{(lo)} - \frac{1}{N_{hi}} \sum_{i=1}^{N_{hi}} \Theta_i^{(hi)} \right| \quad (5.23)$$

can be considered an estimator for the compatibility of the subsamples with respect to their zenith angle distributions.

Since the function  $\Delta\bar{\Theta}$  can only take discrete values, its minimisation cannot be accomplished applying methods like they are used by e.g. the MINUIT minimiser package. These methods rely on valid function derivatives to find the optimum parameter and to estimate the associated uncertainty [Jam98]. Instead, the  $\Delta\bar{\Theta}$  function is minimised by scanning the parameter space for the optimum value of  $p_E$ . The estimation of the parameter uncertainty can then be inferred from the uncertainty of  $\Delta\bar{\Theta}$ .

### 5.2.7. Estimation of the Parameter Uncertainty

If the function  $\Delta\bar{\Theta}$  reaches a global minimum value that is smaller than the uncertainty of the function value, then the symmetrical uncertainty of the parameter  $p_E$  can be estimated from:

$$\sigma_{p_E} \approx \frac{|p_1 - p_2|}{2}, \quad (5.24)$$

where  $p_1$  and  $p_2$  are defined via:

$$\Delta\bar{\Theta}(p_1) = \Delta\bar{\Theta}(p_2) = \sigma_{\Delta\bar{\Theta}} \quad \text{with} \quad p_1 \neq p_2. \quad (5.25)$$

The uncertainty of  $\Delta\bar{\Theta}$  is given by  $\sigma_{\Delta\bar{\Theta}} = \sqrt{\sigma_{\bar{\Theta}_{hi}}^2 + \sigma_{\bar{\Theta}_{lo}}^2}$ , where

$$\sigma_{\bar{\Theta}_{lo}} = \frac{1}{N_{lo}} \sqrt{\sum_{i=1}^{N_{lo}} \sigma_{\Theta_i^{(lo)}}^2} \quad \text{and} \quad \sigma_{\bar{\Theta}_{hi}} = \frac{1}{N_{hi}} \sqrt{\sum_{i=1}^{N_{hi}} \sigma_{\Theta_i^{(hi)}}^2}. \quad (5.26)$$

The uncertainty of the zenith angle for individual events can be estimated from a full chain of air shower simulations, detector simulations, and air shower reconstructions. The procedure is described in more detail in App. D. To select values for the zenith angles to be used in the simulations, the cumulative probability distribution of the zenith angles of the events detected by the surface detector array is plotted in Fig. 5.9. The zenith angles corresponding to uniformly distributed cumulative probabilities are listed in Tab. 5.2. The results of the simulations with respect to the zenith angle uncertainties are listed in Tab. 5.3.

energy range [EeV]	$E \in ]0.5, 1.0]$	$E \in ]1.0, 2.0]$	$E \in ]2.0, 3.0]$	$E > 3$
mean uncertainty $\sigma_{\Theta}$ [°]	1.5	1.2	1.3	0.8

**Table 5.3.:** Energy ranges and corresponding mean zenith angle uncertainties, which are determined as the mean of the zenith angle uncertainties for different zenith angle ranges (see Tab. D.1). These values result from the simulation chain described in more detail in App. D.

### 5.2.8. Results

In Fig. 5.10, the optimisation results for the lower energy cut at 0.5 EeV, 1.0 EeV, 2.0 EeV, and 3.0 EeV are shown. The values of the parameter  $p_E$  for each energy are listed in Tab. 5.4; for a full listing for energies ranging from 0.5 EeV to 3.0 EeV, see Tab. E.1. For the lowest energy,  $E = 0.5$  EeV, the zenith angle distributions and their deviations from one another are shown in Fig. 5.11 (cf. Fig. 5.8 for the corresponding diagram prior to the optimisation). For energy cuts at 1.0 EeV, 2.0 EeV, and 3.0 EeV, the corresponding plots (after applying the correction procedure) are found in App. E.

energy cut [EeV]	parameter $p_E$	uncertainty
0.5	0.795	0.006
1.0	1.27	0.02
2.0	1.25	0.04
3.0	1.95	0.04

**Table 5.4.:** Results of the parameter scan for lower energy cuts at 0.5 EeV, 1.0 EeV, 2.0 EeV, and 3.0 EeV.

The evolution of the parameter  $p_E$  as a function of the lower energy limit is shown in Fig. 5.12. The fraction of events, which is lost due to the modulation of the lower energy cut, is also shown in the diagram. For each lower energy cut, ranging from 0.5 EeV



to 3.0 EeV, the number of events in the dataset never changes by more than 2.1% as compared to the original number of events. The latter corresponds to the respective lower energy cut alone (without the additional energy modulation  $E_{\text{mod}}$ ).

### 5.2.9. Side Effects of the Compensation

The procedure for compensating the impact of the weather conditions on the zenith angle distribution (and thus on the distribution of the arrival directions of incoming cosmic radiation) is based on the modulation of the lower energy cut applied to the full event set. Therefore, it modifies the event subsamples to be used in a particular analysis. As a consequence, not only the zenith angle distribution is subject to a modification, but also the energy spectrum of the air shower events as well as the distribution of azimuth angles is, in general, affected.

To investigate the impact the energy modulation causes with respect to the energy spectrum of the air shower events, the energy undershoot, i.e. the deviation of the lower energy cut from the energy cut when no compensation is applied, is estimated. In Fig. 5.13, the results are presented. Even for the maximum energy undershoot found, the systematic deviation imposed on the determination of the energy (22% according to [ICR09b]) is to be considered the predominant source of uncertainty.

As has been shown in Section 5.1, the weather related signal deviation at ground level depends on the zenith angle of the incoming cosmic ray particle, its particle type, the primary particle energy, and the instantaneous weather conditions. The energy spectrum as well as the zenith angle distribution is therefore expected to be prone to variations caused by varying weather conditions. The azimuth angle distribution, on the contrary, should not exhibit such a dependence, since the weather related signal deviations do not depend on the azimuth angle. Consequently, it should not significantly be subject to modifications by the compensation procedure presented in this section.

To verify that the azimuth distributions remain substantially unaltered, a two-sample  $\chi^2$  test is applied to the azimuth distribution prior to and after applying the compensation procedure, respectively. The corresponding  $\chi^2$  test statistic is calculated in a similar way as in Eqn. 5.20. In this case, however, the azimuth angle range is subdivided into 360 bins, each one  $1^\circ$  in size. The results are shown in Fig. 5.14. The test statistic  $\chi^2$  is plotted versus the lower energy limit. The null hypothesis of the azimuth distributions being compatible cannot be rejected for any of the values of the test statistic. The corresponding critical region is defined by

$$\chi^2 > \chi_{\text{PPF}}(1 - \mathcal{P}_{5\sigma}, n_{\text{dof}}), \quad (5.27)$$

where  $\chi_{\text{PPF}}$  is the percent point function of the  $\chi^2$  distribution,  $n_{\text{dof}}$  is the number of degrees of freedom, and  $\mathcal{P}_{5\sigma}$  corresponds to the two-tailed  $5\sigma$  probability of the normal distribution.

The results of the tests for side effects of the correction procedure are listed in Tab. E.1.

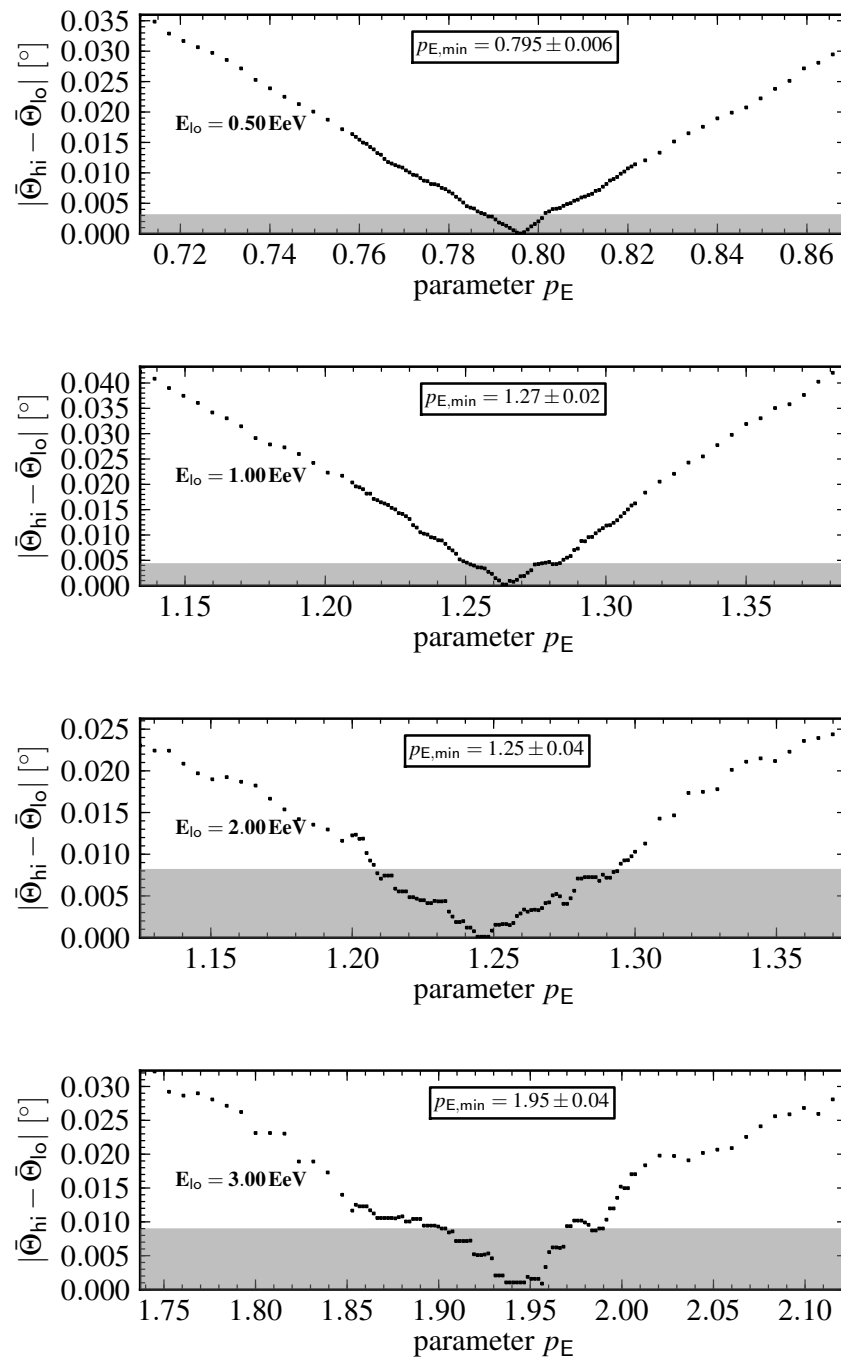


**Figure 5.10.:** Optimisation for the parameter  $p_E$ . The difference of the means of the zenith angle distributions for low and high temperatures, respectively, is depicted by dots. The corresponding uncertainty is shown by the grey area. *From top to bottom:* Results for a threshold energy of 0.5 EeV, 1.0 EeV, 2.0 EeV, and 3.0 EeV, respectively.

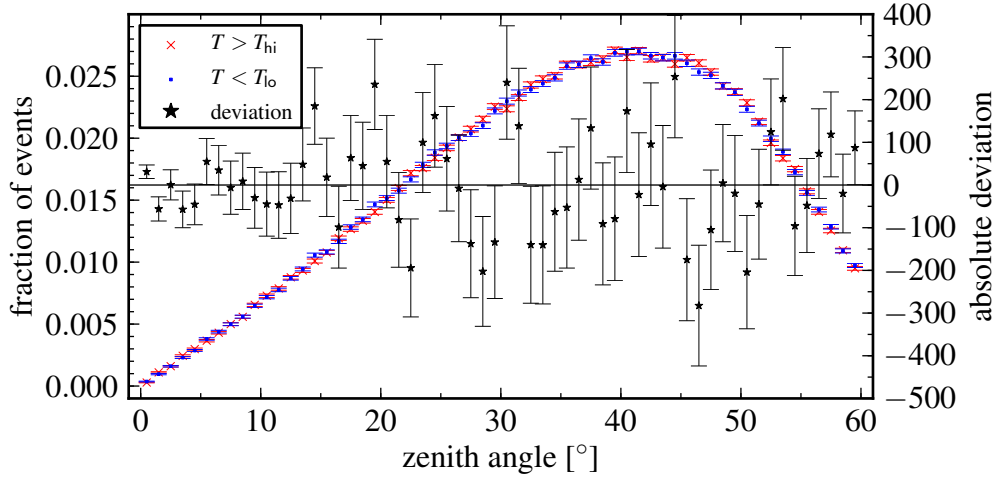


**Figure 5.11.:** Zenith angle distributions for high temperatures ( $T > T_{hi}$ ) and low temperatures ( $T < T_{lo}$ ), respectively, with  $T_{hi} = T_{lo} = T_{med}$ ;  $T_{med} \approx 285.3\text{K}$  denotes the median temperature of the surface detector events. The fraction of events in the corresponding zenith angle bin is plotted, using cross and dot markers, for both subsamples (ordinate on the left-hand side). The star shaped markers indicate the absolute deviation of the numbers of events in both subsamples for each zenith angle bin (ordinate on the right-hand side). The data corresponding to a lower energy cut at 0.5 EeV is shown.

### 5.3. Summary

In this chapter, methods for compensating weather induced variations of the quantities, which are measured by the surface detector of the Pierre Auger Observatory, were presented.

In addition, a method was established, that allows the compensation of the disagreement of the zenith angle distributions due to weather effects. Applying this method to the air shower event data, acquired by the surface detector, results in zenith angle distributions which are compatible within the statistical uncertainties even for sets of weather observables that are very much different from each other.

It was shown, that the correction procedure does not severely modulate the lower energy cut beyond the bounds of the uncertainty that is arising from the energy reconstruction of the air shower events. The azimuth angle distribution has not been found to experience significant alterations either.

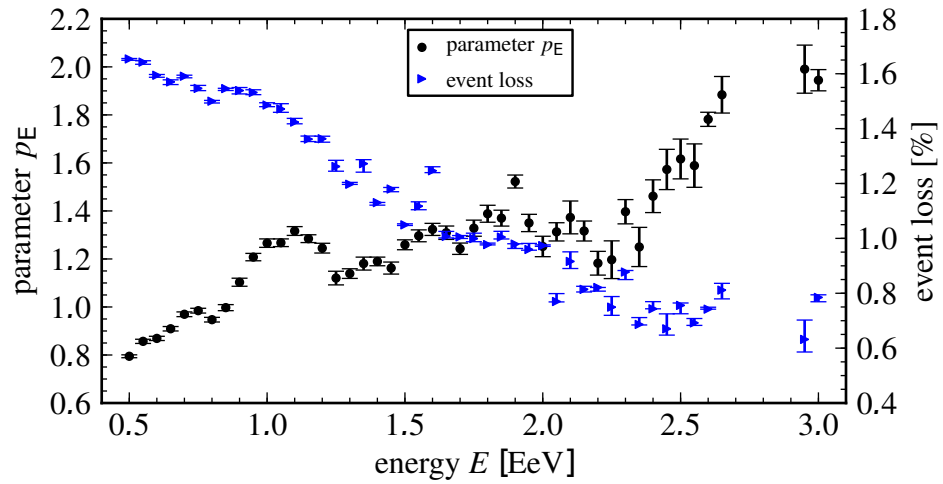


**Figure 5.12.:** Parameter  $p_E$  (black circle markers and ordinate on the left) versus the lower energy limit and the percentage of air shower events lost as a consequence of the correction procedure (blue triangle markers and ordinate on the right).

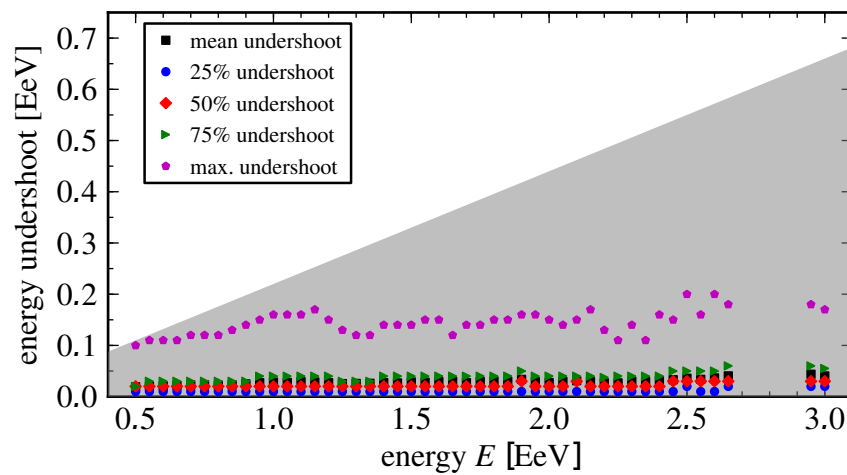


**Figure 5.13.:** Energy undershoot due to the correction. The maximum energy undershoot, the mean energy undershoot as well as the 25% quantiles, 50% quantiles, and the 75% quantiles are plotted. In comparison, the grey area in the background indicates the systematic energy uncertainty [ICR09b].

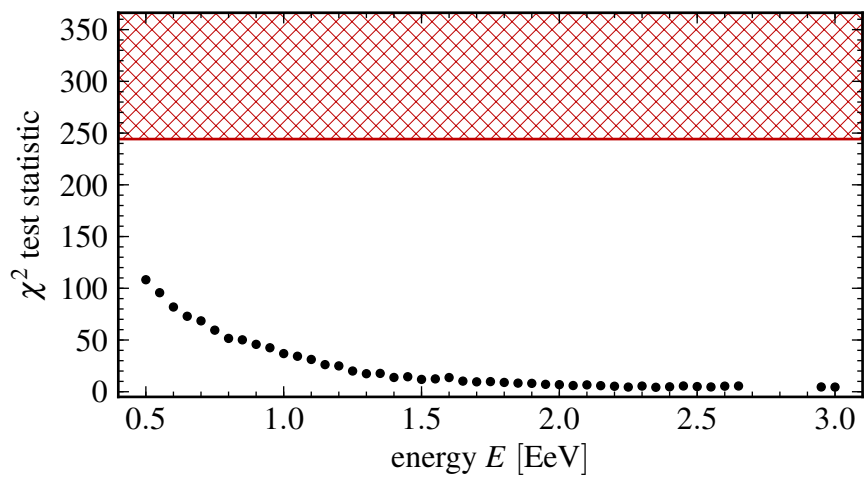


**Figure 5.14.:** Compatibility of the azimuth angle distributions prior to and after applying the corrections. The test statistic for a two-sample  $\chi^2$  test is plotted versus the lower energy limit. The critical region of the test corresponding to  $5\sigma$  in terms of the two-tailed Gaussian probability is indicated by the red hatched area. For values of  $\chi^2$  in this region, the distribution cannot be considered compatible.



# Chapter 6

## Application to the Search for Point Sources

In Chapter 5, a method was presented that allows the compensation of the impact of the instantaneous weather conditions on the zenith angle distribution. Although the procedure can, in general, be applied to any analysis, which is making use of cosmic ray data acquired by the **Pierre Auger Observatory**, it might prove useful especially in anisotropy studies. The zenith angle, together with the azimuth angle and the time, unambiguously defines the arrival direction of a cosmic ray particle. Stabilising the zenith angle distribution with respect to the impact of the weather conditions can therefore also help in enhancing the results of searches for point sources.

The extent, up to which the measurements of extensive air showers are affected by weather related variations of the zenith angle distribution, depends on the zenith angle range covered. The zenith angles, on the other hand, depend on the position of the air shower experiment and the arrival directions to be observed. In particular, the **Pierre Auger Observatory** is situated such that the observation of the centre of our galaxy is a natural choice. Therefore, the procedure described in Chap. 5 is applied to the observation of the centre of the Milky Way in this chapter.

### 6.1. Galactic Centre

The Galactic Centre, as a possible source of cosmic radiation, has been an object of investigation for several astroparticle experiments. The **HESS (High Energy Stereoscopic System)** experiment reported a significant  $\gamma$ -ray excess from the direction of **Sagittarius A\*** [Aha04]. Its position (as equatorial coordinates) at  $266.4^\circ$  in right ascension and  $-29.0^\circ$  in declination is commonly taken as the position of the centre of the Milky Way. Other observations, e.g. by **AGASA (Akeno Giant Air Shower Array)** [Hay99] and **SUGAR (Sydney University Giant Air shower Recorder)** [Bel01] also support the assumption of particle emissions from this region.

Being situated at about 35 degrees of latitude on the southern hemisphere, i.e. at a minimum distance of about 6 degrees from the projection of the Galactic Centre on the Earth, the Pierre Auger Observatory is well suited for its observation.

Charged particles originating from the Galactic Centre are subject to deflections by the magnetic fields in the spiral arms of the Milky Way (see Fig. 6.1(a) for an illustration). In addition, field reversals and irregular field components add further deflections. Only charged particles of sufficiently high magnetic rigidity  $p/q$  ( $p \equiv$  particle momentum,  $q \equiv$  charge of the particle) are capable of reaching the Earth despite the deflections.

Neutrons, being uncharged particles, are not subject to these deflections. At sufficiently high particle energies, a considerable fraction of the neutrons does not decay along the path from the Galactic Centre to the Earth (8.5 kpc in length) due to the dilatation of time. Neutrons can be produced in interactions of charged primordial particles with interstellar matter and they can also initiate extensive air showers in the Earth's atmosphere. The lower limit of the primary particle energy for the neutron scenario is in the order of magnitude of 1 EeV, as can be seen from Fig. 6.1(b). Thus, in the following, this energy will be used as the lower energy limit for the point source search procedure.

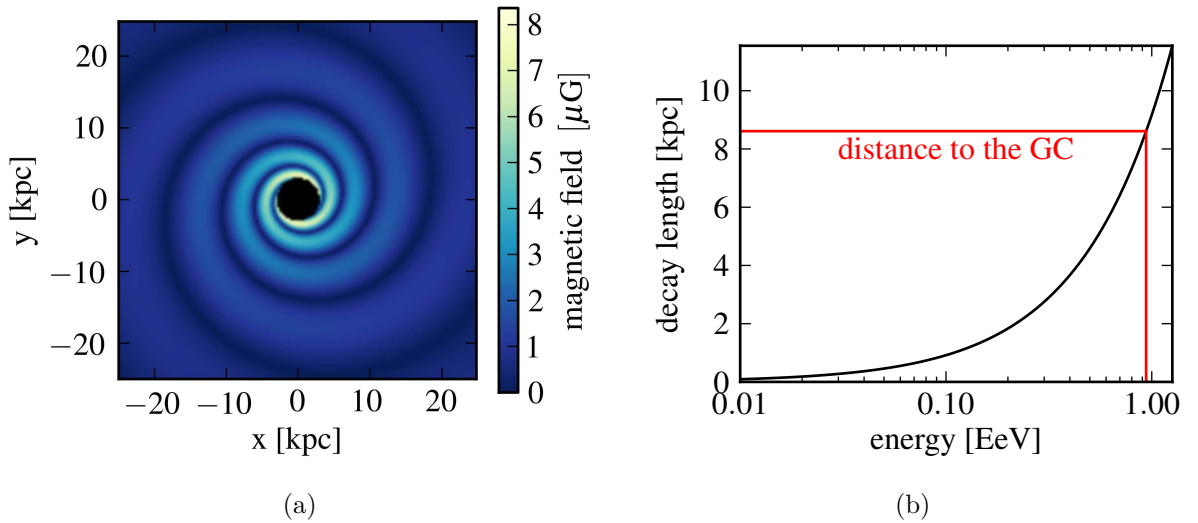


**Figure 6.1.:** Magnetic field strength in the spiral arms of the Milky Way, calculated according to the BSS (Bi-Symmetric Spiral) model [Sof86] (diagram on the left). In the diagram on the right, the decay length for neutrons is plotted versus the neutron energy.

## 6.2. Field of View

Due to the fact, that the angle between the zenith at the site of the Pierre Auger Observatory and the line of sight of the Galactic Centre reaches values down to  $6^\circ$ , it is in the field of view of the observatory during extended periods of time (cf. Fig. 6.2).



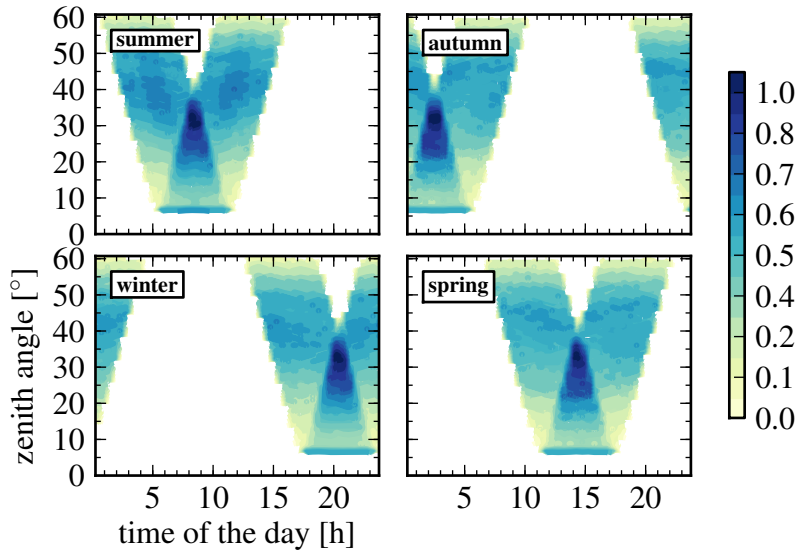


**Figure 6.2.:** Zenith angle at which the Galactic Centre is seen in the course of the day during different austral seasons. The purely geometrical probability for a certain zenith angle at a specific time of the day is weighted with the probability to detect air showers at a certain zenith angle (i.e. the zenith angle distribution of events). The normalised total probability is shown by the colour scale.

However, for different seasons, the centre of our galaxy is in the field of view of the observatory during different times of the day. Therefore, the observations take place for considerably different weather conditions as well. As a consequence, the systematic deviations of the observations are depending on the seasons. The energy modulation procedure described in Chap. 5 aims at compensating for this issue.

For objects whose line of sight is close to the zenith of the observation site, the slant depth (and thus  $\sec\Theta$  with  $\Theta \equiv$  zenith angle) of air showers originating from those objects is subject to large variations. Again, this causes a dependence on the weather conditions; see Chap. 5 and [Abr09b]. In Fig. 6.3, the evolution of  $\sec\Theta$  during one day is shown for the Galactic Centre as the object to be observed and for an object at declination  $\delta \approx 65^\circ$ , respectively.

### 6.3. On–Off Method

The *on-off method* originates from  $\gamma$ -astronomy. It is based on the estimation of the background rate of events from regions of sky, where the detector is positively not observing the point source candidate. As can be seen from Fig. 6.4, cells are defined in a certain declination band. The cell enclosing the source candidate, is referred to as the *on* cell, the other cells are called *off* cells. For cells of equal sizes in the same declination

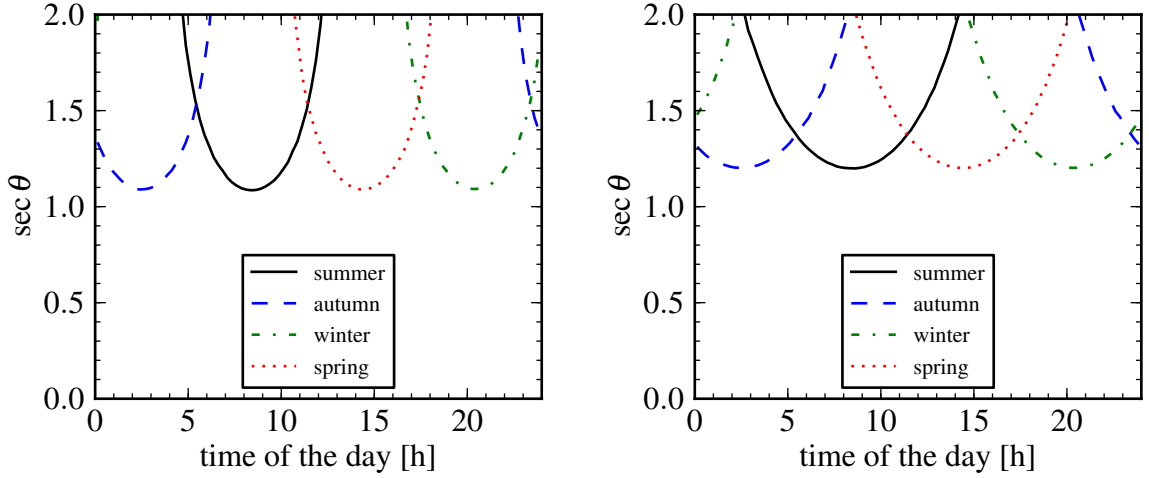


**Figure 6.3.:** Variations of  $\sec\Theta$  for two astronomical objects to be observed in different austral seasons. *Left:* Mean zenith angle vs. the time of the day for different seasons and the Galactic Centre. *Right:* Same as in the diagram on the left, for an astronomical object at declination  $\delta \approx 65^\circ$ .

band, all cells are expected to contain the same number of events, provided the detector is not subject to diurnal variations.

Cosmic ray excesses in the data can be evaluated by means of the Li–Ma significance [Li83, Gil04]; see also App. F:

$$|S_{\text{LiMa}}| = \sqrt{2N_{\text{on}} \ln \frac{(1 + \alpha)N_{\text{on}}}{\alpha(N_{\text{on}} + N_{\text{off}})} + 2N_{\text{off}} \ln \frac{(1 + \alpha)N_{\text{off}}}{N_{\text{on}} + N_{\text{off}}}}. \quad (6.1)$$

Here,  $N_{\text{off}}$  denotes the total number of events in all of the *off* cells,  $N_{\text{on}}$  is the number of events in the *on* cell and  $\alpha$  is the reciprocal of the number of *off* cells. It is also possible to define a signed Li–Ma significance according to:

$$S_{\text{LiMa}} = \begin{cases} +|S_{\text{LiMa}}|, & N_{\text{on}} \geq \alpha N_{\text{off}} \\ -|S_{\text{LiMa}}|, & N_{\text{on}} < \alpha N_{\text{off}} \end{cases} \quad (6.2)$$

## 6.4. Aperture Weighting

The number of active surface detector hexagons, and thus the instantaneous aperture, exhibits variations in the course of a day (see Fig. 6.5). Although this effect is still being investigated, it seems that it is related to battery failures during darkness, i.e. when the solar panel systems of the SD stations are not providing electrical power which then has

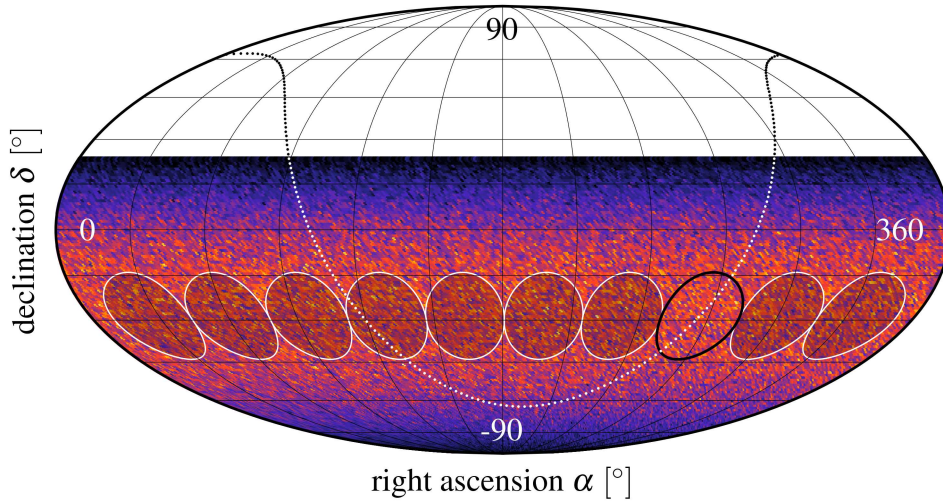


**Figure 6.4.:** Illustration of the *on-off method*. The reconstructed arrival directions of events in the *CDAS Herald repository* (from January 1, 2004, until April 15, 2009) are shown as a Mollweide projection [Sny97]. The dotted line indicates the galactic plane, the *on* and *off* cells are depicted by circles. The black circle marks the border of the *on* cell, whereas the *off* cells are shown as translucent circular disks, bordered by white circles. All directions are given as equatorial coordinates.

to be provided by the batteries [Aug]. At noon in terms of UTC time, i.e. around 9 am in terms of AST (Argentina Standard Time), the number of operational surface detector stations reaches its diurnal minimum.

On a time scale of full years, the variation of the number of active surface detector hexagons does not result in artificial anisotropy with respect to the distribution of right ascension angles. For fractions of the year, e.g. seasons, however, this translates into a non-uniformity of the right ascension distribution. Since the *off* cells are arranged along the right ascension axis, this can cause an artificial loss of events in the *off* cells or in the *on* cell.

The ansatz

$$w(\mathbf{t}) = \frac{N_{\text{d}}^{(\text{hex})}(\mathbf{t})}{N^{(\text{hex})}(\mathbf{t})} \quad (6.3)$$

can be used to apply a compensation. The weight for an air shower event recorded at the time  $\mathbf{t}$  is  $w(\mathbf{t})$ , the instantaneous number of active surface detector hexagons is denoted by  $N^{(\text{hex})}(\mathbf{t})$ . The running mean of the instantaneous number of active surface detector hexagons on a time scale of one day is  $N_{\text{d}}^{(\text{hex})}(\mathbf{t})$ . Instead of counting the number of events in each *on/off* cell, their corresponding weights have to be added to apply the aperture weighting.

The systematic uncertainty that is caused by the weighting procedure as well as by

the energy modulation proposed in Chap. 5 is estimated in the following using simulated sets of events.

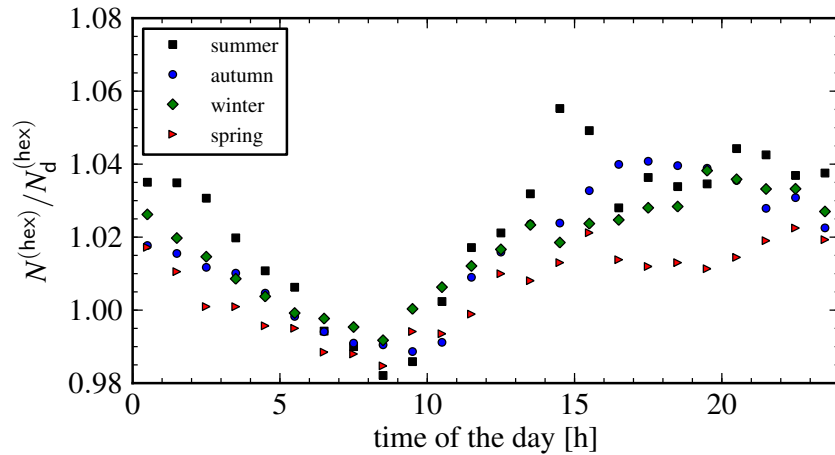


**Figure 6.5.:** Diurnal variations of the number of active surface detector hexagons. The ratio of the instantaneous number of events and its running mean in a time scale of one day is plotted for each austral season.

## 6.5. Application to Isotropic Datasets

Applied to an isotropic dataset, the on-off method is not supposed to yield a significant anisotropy signal; the same is true for other valid methods for investigating small scale anisotropy. Since the datasets acquired from real experiments usually contain a small amount of reconstructed air shower events only, they are subject to fluctuations. Thus, there is a finite probability that an event set exhibits a non-uniform distribution of arrival directions even though the air shower events might stem from an isotropic background.

Apart from this unavoidable effect, that is merely due to the nature of Poisson processes, anisotropy might artificially be created by deficiencies of the detector itself. Moreover, artificial anisotropy might be caused by procedures trying to compensate for such detector deficiencies. In this section, the method described in the previous chapter is therefore examined with respect to parasitic effects.

### 6.5.1. Generating Isotropic Datasets

The method for generating isotropic datasets to be used as the input data for the point source search algorithms can be created from a dataset of real events, i.e. air shower events recorded by an air shower experiment.

Here, air shower event data acquired by the surface detector of the Pierre Auger Observatory is used to form the event pool from which the isotropic datasets are created. Events recorded from January 1, 2004, until April 15, 2009, are used in the following. The standard quality cuts are applied and time periods of degraded detector performance are excluded. Events at reconstructed zenith angles beyond  $60^\circ$  are not taken into account.

Values for the reconstructed primary particle energy and the azimuth angle of isotropic events are directly drawn from the distributions of the corresponding reconstructed quantities of the original event set. By doing so, their distributions in the isotropic dataset is expected to be compatible with the input set of events.

As already shown in Chap. 5, the performance of the surface detector, especially regarding the impact of the weather conditions, is depending (among other things) on the zenith angle. Zenith angles for the dataset to be created should therefore be drawn from parts of the original angular distribution rather than from the full range of zenith angles. Here, the distribution is subdivided into five intervals of equal cumulative probability. The limits of the zenith angle intervals are those listed in Tab. 5.2.

An isotropic dataset, created from some original dataset, should have the same seasonal and diurnal features. By splitting the time values of the original dataset (in terms of UTC) into full days and the remainder, the diurnal part, this can be achieved [San08]. By drawing values from both distributions and combining them again, the UTC time values for the isotropic event set is formed.

For the weather correction procedure, weather data also has to be included into the new dataset. Weather information of the original event set, matching the values of the new UTC time values best, are used as an approximation.

A total of 1000 isotropic datasets has been produced this way.

### 6.5.2. Li–Ma Significance of Isotropic Datasets

For each isotropic dataset, the Li–Ma significance for the *on* cell centered at the position of the Galactic Centre has been evaluated. The energy cut is chosen to be 1 EeV, according to Section 6.1. The radius of the *on/off* cells is chosen to be  $8^\circ$ , as determined in a prescription scan [GCG78, Bon09]. The results are filled into a histogram; see Fig. 6.6. As can be seen, the standard deviation and the mean value of the distribution of the significances are compatible with a normal distribution.

### 6.5.3. Li–Ma Significance of Isotropic Datasets, Corrections Applied

Fig. 6.7 contains the results for the Li–Ma significance after applying the corrections. As can be seen from the diagrams, the correction for the energy modulation does not introduce a systematic shift for the significance. However, the aperture correction, causes a shift by  $0.2\sigma$ , which is still small compared to the statistical uncertainty of the Li–Ma significance.

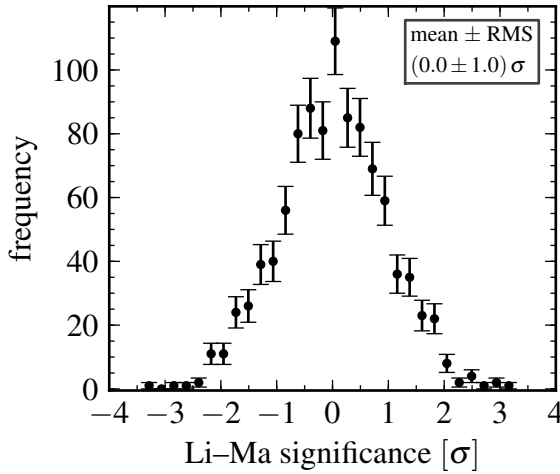


**Figure 6.6.:** Li–Ma significance distribution for isotropic data. The standard deviation and the mean value correspond to a normal distribution.

## 6.6. Application to Anisotropic Datasets

In this section, the effect of the correction procedures on anisotropic datasets shall be investigated. The isotropic datasets created in Section 6.5 are reused for this purpose. Following a Gaussian distribution, air shower events in the *on* cell are selected with respect to the angular distance from the Galactic Centre. These events are then added to the events contained in the *on* cell region to create an excess of events of 10%, corresponding to a Li–Ma significance of about  $4.5\sigma$ .

In Fig. 6.8, the results for this modified dataset are shown. Again the aperture correction introduces a small systematic shift.

## 6.7. Application to Data Taken by the SD Array

In this section, the method for modulating the lower energy limit is applied to data taken by the surface detector, starting from January 1, 2004, until April 15, 2009. In addition to this correction, the variations of the aperture are compensated for as described in Section 6.4.

In Fig. 6.9, the Li–Ma significances of an excess in the vicinity of the Galactic Centre are shown. The lower energy limit,  $E_{lo}$ , is chosen to be 1 EeV in accordance with the lower energy limit of neutrons corresponding to a decay length of 8.5 kpc. A cell radius of  $8^\circ$  is chosen as it is suggested by the scan performed in [GCG78]. The map is created by determining the value of the Li–Ma significance for the *on* cell centered at positions in an area of  $\pm 20^\circ$  around the position of the Galactic Centre. The position, in terms of the right ascension and the declination, is changed in steps of  $1^\circ$ , yielding 1681 pixels in the contour plot.

Since the cell radius originates from a scan of a subset of the dataset, no conclusion can be drawn from the excess found in the map. Further data needs to be acquired to

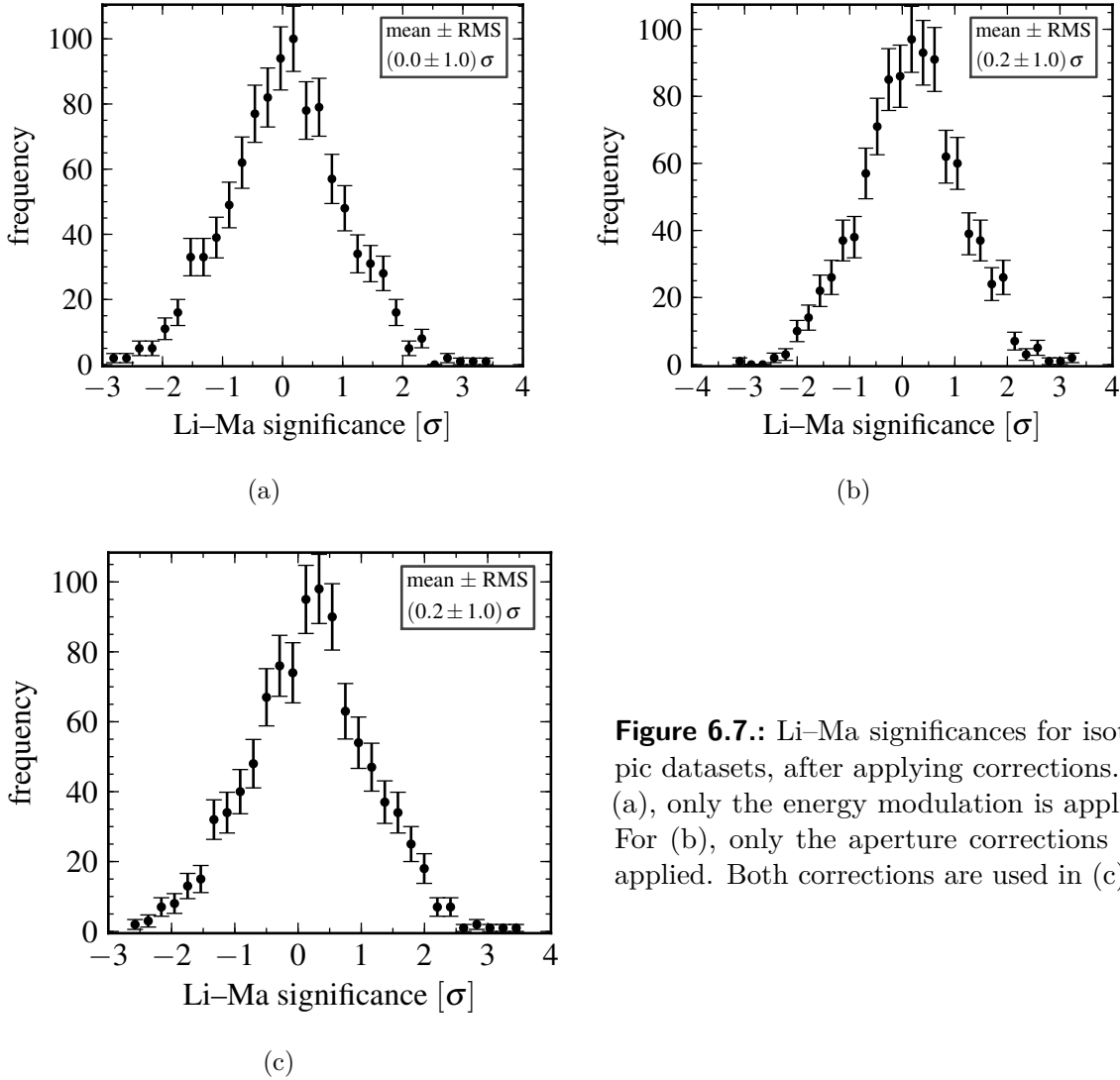


**Figure 6.7.:** Li-Ma significances for isotropic datasets, after applying corrections. In (a), only the energy modulation is applied. For (b), only the aperture corrections are applied. Both corrections are used in (c).

accept or reject the assumption of an excess for the parameters specified.

For the same set of parameters, the results of a full sky survey (apart from a small margin of  $8^\circ$  at the borders of the map) are plotted in Fig. 6.10, applying the same method as described for Fig. 6.9. In this case, the Mollweide map projection [Sny97] is chosen, since for the range of right ascension angles and declination angles covered, the map would be subject to distortions otherwise.

To evaluate the impact of the corrections on a scan of the parameter space spanned by the lower energy cut,  $E_{lo}$ , and the radius of the *on* cell (which equals the radii of the *off* cells), the scan is performed twice.

Firstly, the Li-Ma significance of an excess (or deficit) of cosmic rays, originating from the direction of the Galactic Centre region, is calculated for various values of the lower

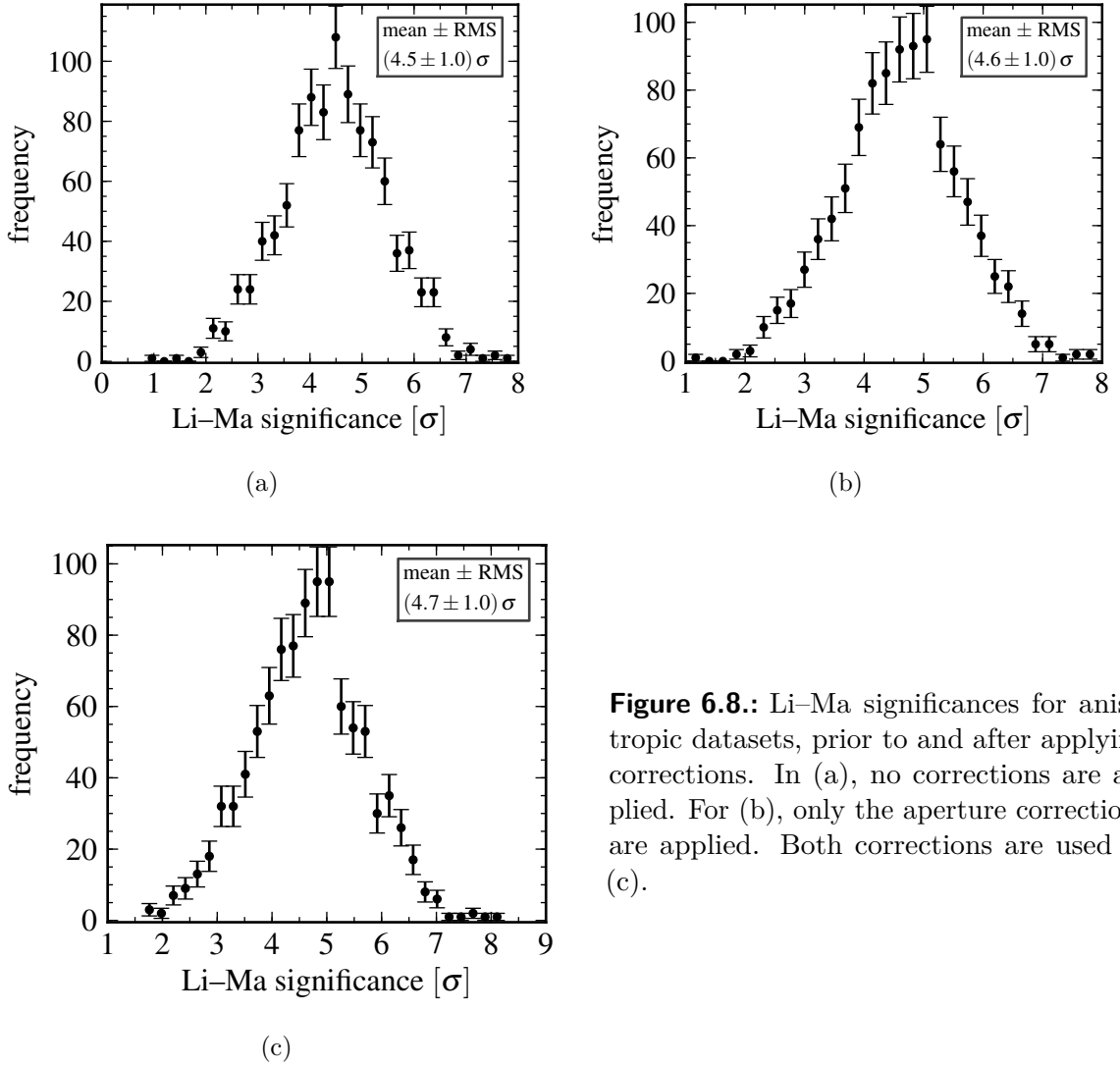


**Figure 6.8.:** Li-Ma significances for anisotropic datasets, prior to and after applying corrections. In (a), no corrections are applied. For (b), only the aperture corrections are applied. Both corrections are used in (c).

energy cut and various values of the cell radius. No corrections are applied at this point. However, the zenith angle range of cosmic ray events taken into account needs to be restricted to reduce the impact of the variations of the zenith angle distributions. A range of  $1^\circ < \Theta \leq 23^\circ$  is chosen as it is proposed in [GCG78]. A maximum significance of about  $3.6\sigma$  is found for a cell radius of  $12^\circ$  and a lower limit for the energy of approximately 1 EeV (cf. Fig. 6.11(a)). However, the excess is found to disappear again for slightly higher energies, whereas cosmic ray sources are commonly expected to emit particles according to a continuous energy spectrum, not as a monoenergetic radiation.

Secondly, this procedure is repeated for a dataset to which the corrections regarding the energy modulation and the aperture variations are applied. The result is shown in Fig. 6.11(b). This time, no restrictions of the zenith angle range of the cosmic ray events



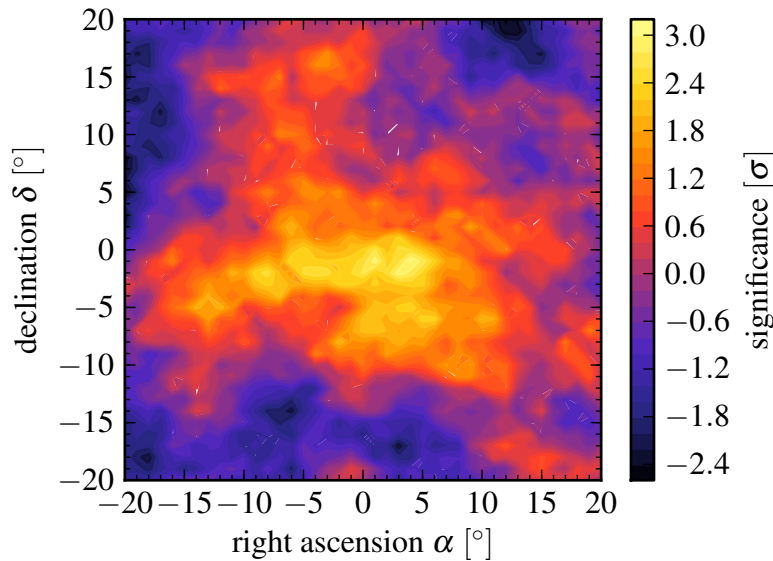


**Figure 6.9.:** Li–Ma significance map for the vicinity of the Galactic Centre of the Milky Way. The filled contours indicate the significance of an excess of cosmic radiation originating from arrival directions of  $\pm 20^\circ$  in both declination and right ascension with respect to the central region. The levels of significance are given in terms of Li–Ma significance, they are shown as a colour scale [Rap02]. Both the aperture weighting (see Section 6.4) and the energy modulation, as described in Chap. 5, were applied prior to estimating the significances.

are applied, since the procedure described in Chap. 5 is expected to stabilise the zenith angle distribution. As can be seen from the diagram, no pronounced excess is found in the low energy regime, whereas the excess at about 1.9 EeV clearly stands out and extends towards higher energies as it is expected for cosmic ray sources with a continuous energy spectrum.

## 6.8. Summary

In this chapter, the effect of the correction procedure presented in Chap. 5 on the Li–Ma significance for event maps was investigated. In addition, a further correction, concerning the variations of the number of active surface detector hexagons, was presented and also subjected to tests regarding its impact on the Li–Ma significance for event maps. It was found that the correction procedure presented in Chap. 5 does not interfere with neither isotropic nor anisotropic event maps. The aperture correction presented in this chapter causes a small systematic deviation.

Finally, the correction procedures were applied to data taken by the surface detector of the Pierre Auger Observatory during a period of time of more than five years. The Li–Ma significance of an excess of cosmic radiation originating from a direction close to

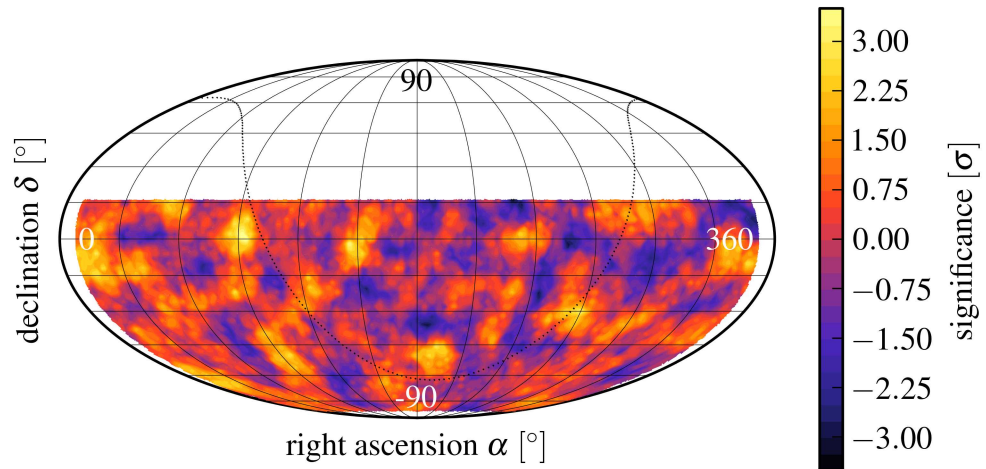
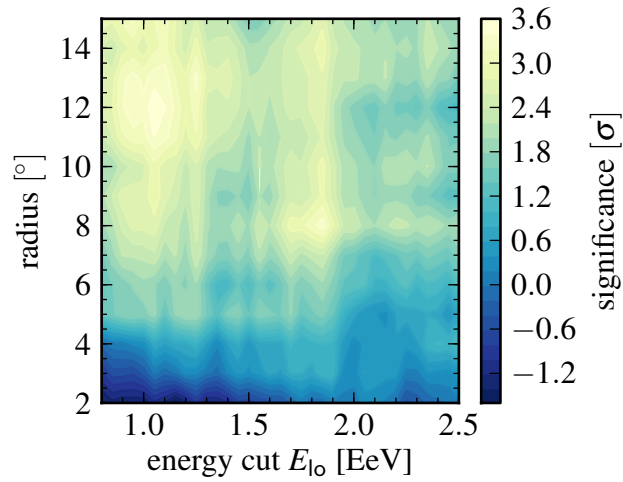
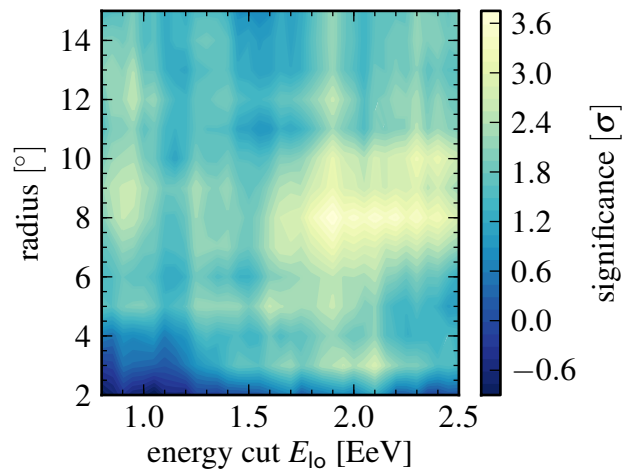


**Figure 6.10.:** Significances of cosmic ray excesses for the full sky, except for  $8^\circ$  margins in right ascension and declination. The aperture weighting (see Section 6.4) as well as the energy modulation (cf. Chap. 5) were applied prior to estimating the significances. The levels of the significance are indicated by the colour scale [Rap02]. The significance map is presented as a Mollweide projection [Sny97].

the Galactic Centre was evaluated and its evolution depending on the lower energy cut and the size of the *on* cell, used for the application of the *on-off method*, was calculated. It seems, the correction procedures cause a suppression of the excess found at energies of about 1 EeV when no correction is applied. Instead, the excess at about 1.9 EeV (and beyond) seems to be enhanced. No final conclusion, however, can be made until more air shower data is available, since at this time, the excess observed could be due to statistical fluctuations alone.



(a)



(b)

**Figure 6.11.:** Results of a parameter scan, varying both the lower energy cut and the size of the *on* cell. Surface detector data from January 1, 2004, until April 15, 2009, are used. In (a), the result is shown for the scan without any corrections applied. In (b) the corresponding result is shown after applying the corrections described in Chap. 5 and Section 6.4.



# Chapter 7

## Summary

The impact of the variations of the weather on the performance of the Pierre Auger Observatory were the subject matter of the thesis at hand. In particular, the effects these variations are giving rise to with respect to small scale anisotropy studies were investigated and procedures for their compensation were established.

In order to be able to estimate the dependence on weather observables, a survey of the weather characteristics of the southern site of the Pierre Auger Observatory was performed. The sources for weather data were assessed and complemented by a procedure that allows the estimation of ambient temperatures from the internal sensor equipment of the detector stations which constitute the SD (Surface Detector) array. Nearly all detector stations are equipped with internal temperature sensors suitable for applying this procedure. Therefore, the estimation of the air temperature at ground level in the vicinity of the air shower core of a particular extensive air shower becomes possible. The knowledge of the instantaneous weather conditions is a requirement for the estimation of atmospheric effects on the development of extensive air showers (see e.g. [Abr09b]).

Once an extensive air shower triggers the surface detector array of the Pierre Auger Observatory, the signals recorded by the detector stations can be corrected for to reduce the uncertainty caused by weather effects. However, at energies of the primary cosmic ray particle, for which the probability to detect its incidence is considerably lower than 100%, the actual fraction of events recorded by the extensive air shower experiment also depends on the weather. A procedure was therefore established to compensate for the dependence of the zenith angle distribution of the air showers on the weather. Since the zenith angle, in connection with the azimuth angle and the time, unambiguously defines the arrival direction of a cosmic ray particle, this is expected to also impact studies of small scale anisotropy. It was found, that the procedure is capable of stabilising the zenith angle distribution at the expense of the number of events available for analysis. However, the loss of events hardly exceeds a fraction of 2%. The azimuth angle distribution is substantially left unaltered. No effect on the energy spectrum beyond the bounds imposed by the systematic uncertainty of the energy reconstruction of the SD data could be observed. To establish the correction procedure, the zenith angle uncertainty of the reconstruction of the arrival direction had to be estimated. The estimation

was performed by creating simulated air showers using AIRES (AIR-shower Extended Simulations), followed by a detector simulation and air shower reconstruction using the Offline framework.

As the southern site of the **Pierre Auger Observatory** is located on the 35<sup>th</sup> degree of latitude on the southern hemisphere, the Galactic Centre of the Milky Way is well within the field of view of the observatory for extended periods of time. The procedure for stabilising the zenith angle distribution was therefore applied to the search for a point source located in the vicinity of the Galactic Centre. It was found, that the procedure does not create artificial anisotropy in simulated isotropic sets of air shower events. It does not dilute simulated anisotropy signals either.

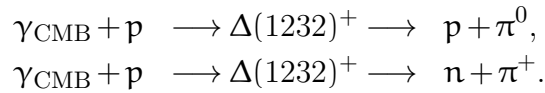
The number of active hexagons of the surface detector array of the **Pierre Auger Observatory** was found to be subject to variations in the course of a day. Although these variations are not expected to be significant on the time scale of full years, this is no longer true for fractions of years or with respect to the austral seasons. A procedure was therefore established to reduce the variations of the instantaneous aperture, which is calculated from the number of active hexagons per unit time.

Both the procedure for stabilising the zenith angle distribution and for reducing the variations of the active surface detector area were applied to air shower event data, recorded by the surface detector of the **Pierre Auger Observatory** during more than five years of operation. By using a scan procedure, a set of parameters maximising the excess of cosmic radiation in the vicinity of the Galactic Centre was determined. Within a radius of approximately  $8^\circ$  around the central region, an excess of cosmic radiation, corresponding to a significance of  $3.6\sigma$ , was found for a lower energy cut of 1.9 EeV. However, due to the scan, further air shower data has to be acquired before the assumption of a signal from the centre of the Milky Way can be accepted or rejected.

# Appendix A

## GZK Horizon for Protons

The suppression of the cosmic ray flux caused by the the GZK (Greisen–Zatsepin–Kuz'min) mechanism is mainly due to the resonant production of  $\Delta(1232)^+$  in interactions of CMB (Cosmic Microwave Background) photons with cosmic ray particles:



The cross sections for heavier resonances are considerably smaller than for  $\Delta(1232)^+$  [Müc99], they only contribute significantly at energies much higher than the GZK threshold. Around the threshold energy, cosmic ray particles are also subject to direct, i.e. non-resonant, conversion processes, which only contribute negligibly, however [Müc99].

For a precise prediction of the energy loss of cosmic ray protons, all interaction channels have to be taken into account. Therefore, the procedure presented in this appendix can only provide a rough estimation of the energy loss as only the main channel is considered.

### A.1. Proton Tracking

The energy loss a cosmic ray proton suffers, while it is propagating through the CMB radiation field, is estimated by tracking a certain number of protons along their paths; for this simulation, the number of protons is arbitrarily chosen to be 100. After distances corresponding to multiples of the mean free path length of a proton in the CMB, the energy loss for each proton is calculated. The typical decrease in energy of a proton is then determined by averaging the energies of all the protons tracked at each individual waypoint.

The length  $\lambda$  of the mean free path can be estimated by

$$\lambda \approx \frac{1}{\sigma_{\Delta} n_{\gamma}}, \quad (\text{A.1})$$

where  $n_\gamma$  denotes the number density of photons in the CMB radiation field, which, according to results from WMAP (Wilkinson Microwave Anisotropy Probe) and COBE (Cosmic Background Explorer) [Ben03], can be estimated to be close to  $n_\gamma \approx 410 \text{ cm}^{-3}$ . The cross section of the  $\Delta(1232)^+$  can roughly be described by a boxcar function [Ste73, Gai95, Muc99]:

$$\sigma_\Delta(\sqrt{s}) = \Theta(\sqrt{s} - [m_\Delta - \Gamma_\Delta/2])\Theta([m_\Delta + \Gamma_\Delta/2] - \sqrt{s}) \cdot 500 \mu\text{b}. \quad (\text{A.2})$$

Here,  $\Theta$  is the Heaviside step function and  $\sqrt{s}$  is the energy in the centre of mass system of a cosmic ray proton and a CMB photon. Values for the mass  $m_\Delta$  of the  $\Delta$  resonance and its decay width  $\Gamma_\Delta$  are (see [Ams08])  $m_\Delta = (1232 \pm 2) \text{ MeV}$  and  $\Gamma_\Delta = (120 \pm 5) \text{ MeV}$ . Thus, provided the centre of mass energy suffices for the resonant production of the  $\Delta(1232)^+$ , the mean free path length for the proton is in the order of magnitude of 1.6 Mpc.

By means of a Lorentz transformation into the centre of mass system of the cosmic ray proton and the CMB photon, the minimum proton energy required for the production of a photo-pion can be estimated as a function of the photon energy  $E_\gamma$ :

$$E_p > \frac{m_{\pi^0}}{2E_\gamma}(2m_p + m_{\pi^0}). \quad (\text{A.3})$$

During the tracking of individual protons, this inequality is evaluated at each single waypoint. Only those cosmic ray protons, which are meeting the criterion then, are subject to a simulated energy loss. The production of a pion via an intermediate  $\Delta(1232)^+$  baryon essentially causes a decrease of the Lorentz factor of the cosmic ray proton according to [Rac96]

$$\tilde{\gamma}_{\text{CR}} \approx \gamma_{\text{CR}} \frac{m_p - m_{\pi^0}}{m_p} \quad \text{with} \quad \gamma_{\text{CR}} = E_p/m_p c^2, \quad (\text{A.4})$$

where  $\gamma_{\text{CR}}$  denotes the Lorentz factor of a cosmic ray proton prior to the interaction with a CMB photon and  $\tilde{\gamma}_{\text{CR}}$  is the corresponding Lorentz factor after photo-pion production.

The energy spectrum of CMB photons resembles that of Planck's blackbody radiation at a temperature of  $T_{\text{CMB}} = 2.73 \text{ K}$  [Fix96]. Therefore, values for the photon energies used in simulated photon-proton interactions are randomly drawn from the distribution

$$\frac{dn_\gamma}{dE_\gamma} = C_\gamma \frac{E_\gamma^2}{e^{E_\gamma/k_B T_{\text{CMB}}} - 1}, \quad (\text{A.5})$$

where  $k_B$  stands for the Boltzmann constant,  $dn_\gamma/dE_\gamma$  for the photon number density at the energy  $E_\gamma$ ;  $C_\gamma$  is the normalisation constant for the energy interval considered. For this simulation, photon energies between  $10^{-5} \text{ eV}$  and  $2 \cdot 10^{-3} \text{ eV}$  were taken into account, because the cumulative probability for photon energies beyond these limits is negligible.



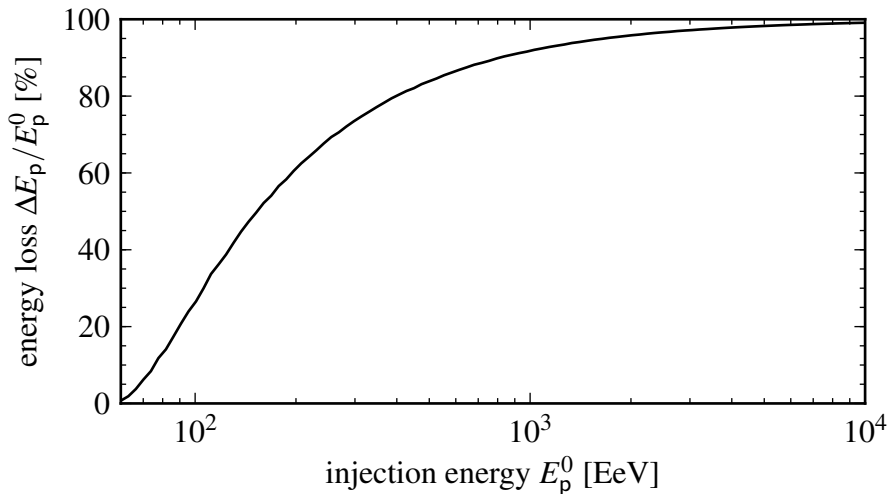


**Figure A.1.:** Energy loss of a proton due to the GZK suppression. The relative decrease in energy after a propagation distance of 100 Mpc is plotted against the injection energy  $E_p^0$ .

## A.2. Results

The results of the proton tracking simulations for various injection energies are shown in Fig. 2.5; the suppression is plotted versus the distance from the point of injection. In Fig. A.1, the relative energy loss of a proton after a fixed propagation distance of 100 Mpc is presented as a function of the injection energy. For an injection energy of 100 EeV, the GZK horizon for a 50% energy loss can thus be estimated to be in the order of magnitude of  $D_{\text{GZK}} \approx 100$  Mpc. For injection energies of about  $10^4$  EeV, only approximately 1% of the injection energy still remains after 100 Mpc as a consequence of the interactions of the cosmic ray proton with the photons of the cosmic microwave background radiation.



# Appendix B

## Weather Databases

Weather data originating from two sources have been used for the analysis at hand. Firstly, the molecular atmosphere database, which is one of the Offline databases [Kei21], is queried to retrieve the monthly atmospheric layer profiles as well as the information from individual balloon launches. Secondly, the *Bariloche weather files* [All88, Bar] have been used to obtain weather information on the temperature and air pressure at ground level.

Additionally, monitoring information of the SD (Surface Detector) stations have been exploited to infer the instantaneous weather conditions from the quantities measured by internal sensors of the stations.

### B.1. Balloon Data & Monthly Layer Profiles

The results of the radio soundings can be retrieved in the following way, using the data found in the MySQL<sup>®</sup> databases of the Offline [All08b]:

- select table `molecular` in the Offline database `Atm_Molecular_0_A`,
- select entries for which `profile_type_id=14` ( $\equiv$  radio soundings).

In a similar way, the monthly atmosphere profiles can be accessed:

- select the Offline database `Atm_Molecular_0_A`,
- in table `profile_type` look for the `profile_type_id` for which `profile_type_name='Malargue month model'` (with *month* being replaced by the English name of the month),
- look for the `molecular_id` of the most recent ( $\equiv$  highest value for `last_modified`) entry in table `molecular` for which `profile_type_id` is equal to the one found in the previous step,

- select the entries in table `molecular_layer` for which `molecular_zone_id` is equal to the `molecular_id` found in the previous step.

The instantaneous air density at a certain altitude and time can be approximated using the averaged atmospheric layer profiles as well as current temperature information [Wil08]:

$$\rho(\mathbf{h}, \mathbf{t}) = \rho_{\text{avg}}(\mathbf{h}) + (\mathbf{T}_G(\mathbf{t}) - \mathbf{T}_{G,\text{avg}})\alpha(\mathbf{h}). \quad (\text{B.1})$$

Here,  $\rho(\mathbf{h}, \mathbf{t})$  is the instantaneous air density at a certain altitude,  $\mathbf{T}_G(\mathbf{t})$  is the instantaneous temperature at ground level,  $\rho_{\text{avg}}(\mathbf{h})$  is the average air density for the corresponding month, whereas  $\mathbf{T}_{G,\text{avg}}$  is the average temperature at ground for the same month. The function  $\alpha(\mathbf{h})$  yields the dependency of the air density on the temperature at ground; it can be parameterized by [Wil08]:

$$\alpha(\mathbf{h}) = A e^{-\mathbf{h}/B_{d\rho/dT}}. \quad (\text{B.2})$$

The parameters for the latter equation can be determined from radio soundings [Kei37] performed on a monthly basis on the **Pierre Auger Observatory** site. Basically, several measurements of the air density and temperatures at ground for each month have to be evaluated and Eqn. B.2 can be fitted to these data sets to obtain the parameter set for each month or each season separately.

## B.2. Weather Station Data

The weather conditions at the ground level of the **Pierre Auger Observatory** are monitored by the weather stations at the FD (Fluorescence Detector) telescope buildings, the CLF (Central LASER Facility) and the BLS (Balloon Launch Station); these stations provide data at regular intervals of 5 minutes. The information is available from [Bar] as ASCII files, containing one line for each data record. See [All88] for details on the structure of these files.

## B.3. Surface Detector Monitoring Data

The surface detector stations of the **Pierre Auger Observatory** record monitoring information at regular intervals of 400 seconds. It includes (among other quantities) station temperature information, that can be used to infer the ambient temperature (see Section 4 for details). The information are available as data trees (ROOT format), as part of the monitoring data repository from the CC-IN2P3 (Centre de Calcul de l'IN2P3).

# Appendix C

## Data from Weather Stations

This appendix contains figures showing weather information that were acquired by weather station equipment in various facilities on site of the Pierre Auger Observatory. In addition, distributions of the deviations between the quantities measured by the stations are plotted for all possible combinations of the data sources in the following.

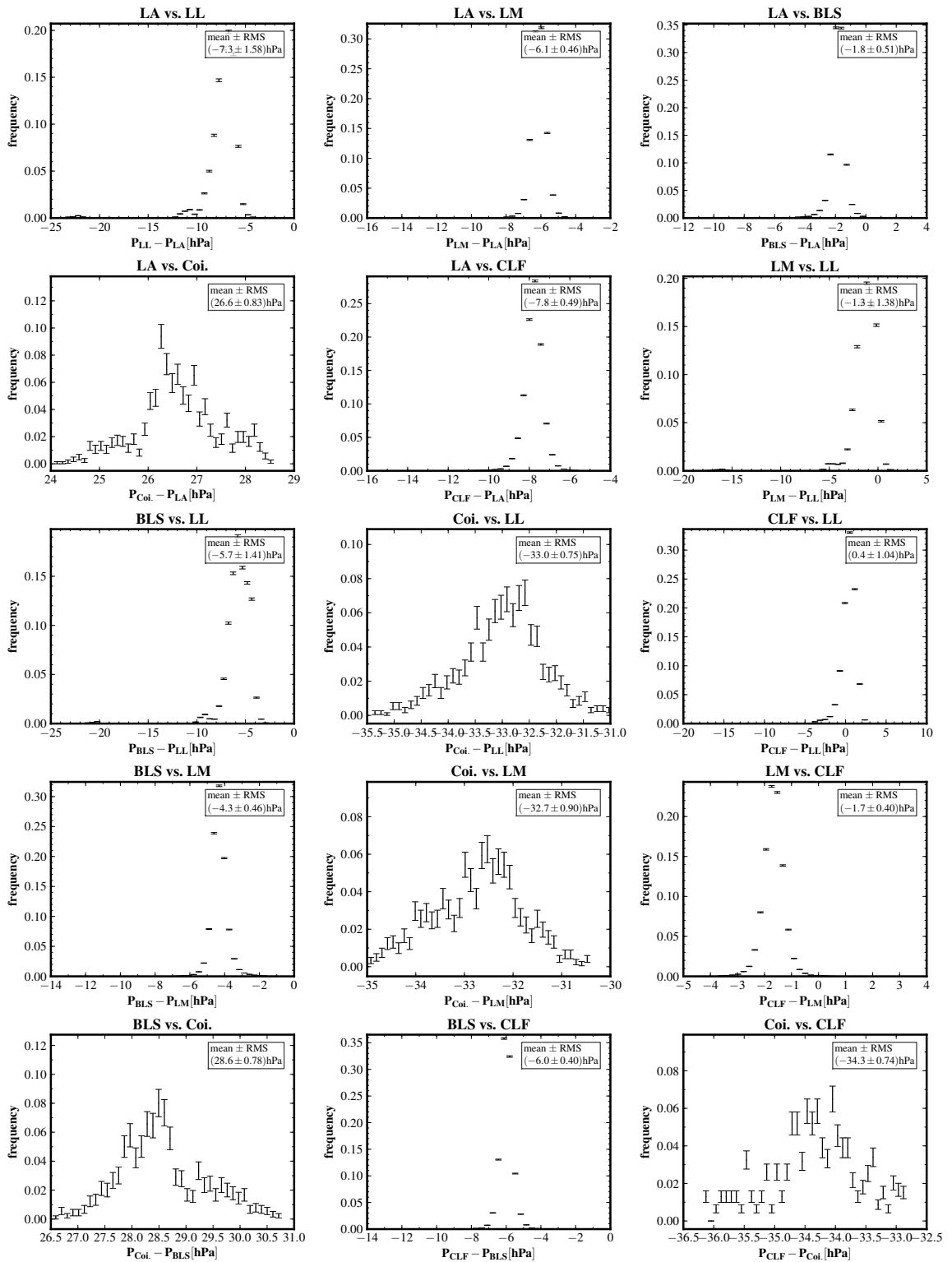
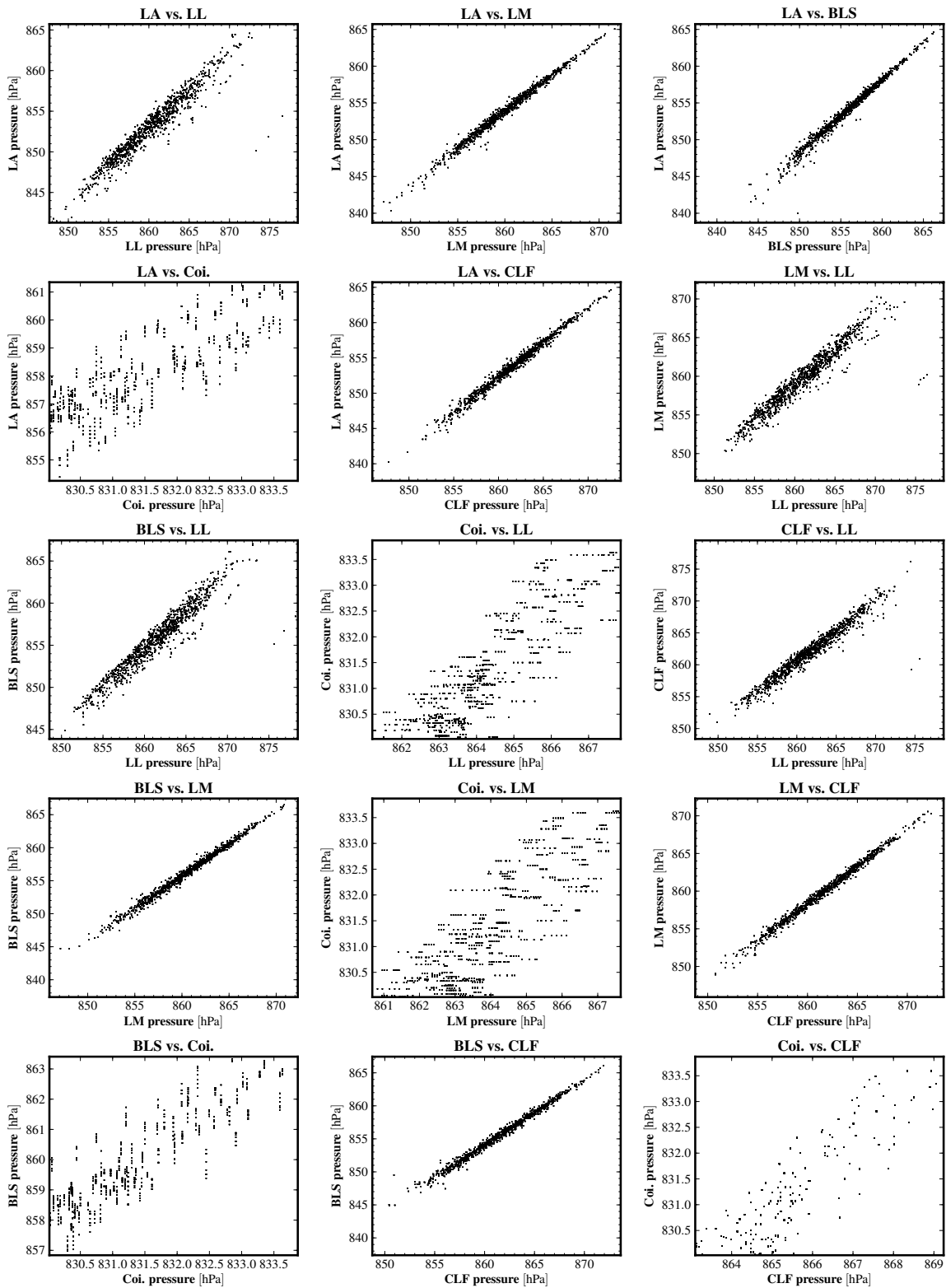


Figure C.1.: Pressure deviations between weather stations.



**Figure C.2.:** Correlation of pressure as recorded by the weather stations.

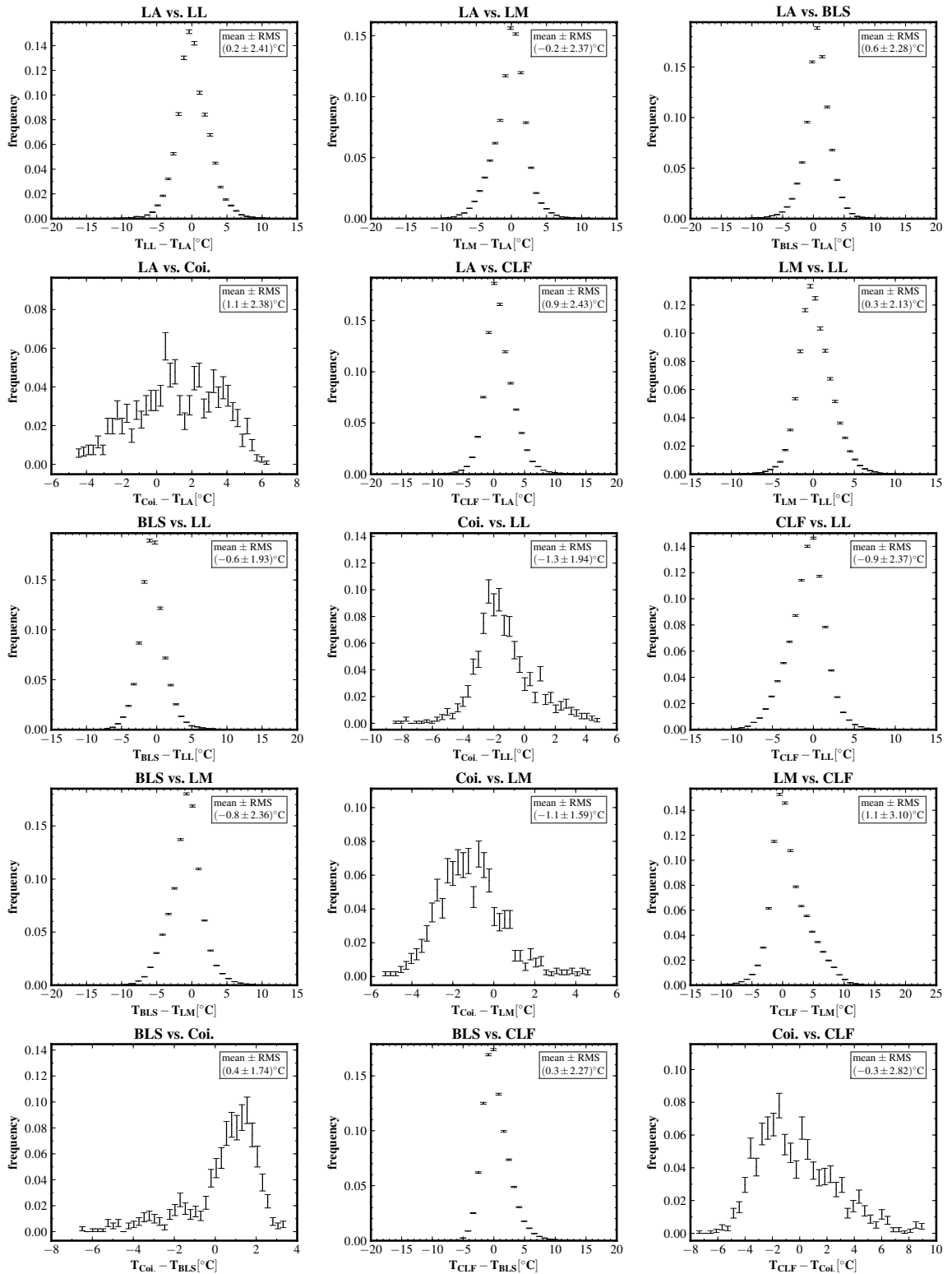


Figure C.3.: Temperature deviations between weather stations.



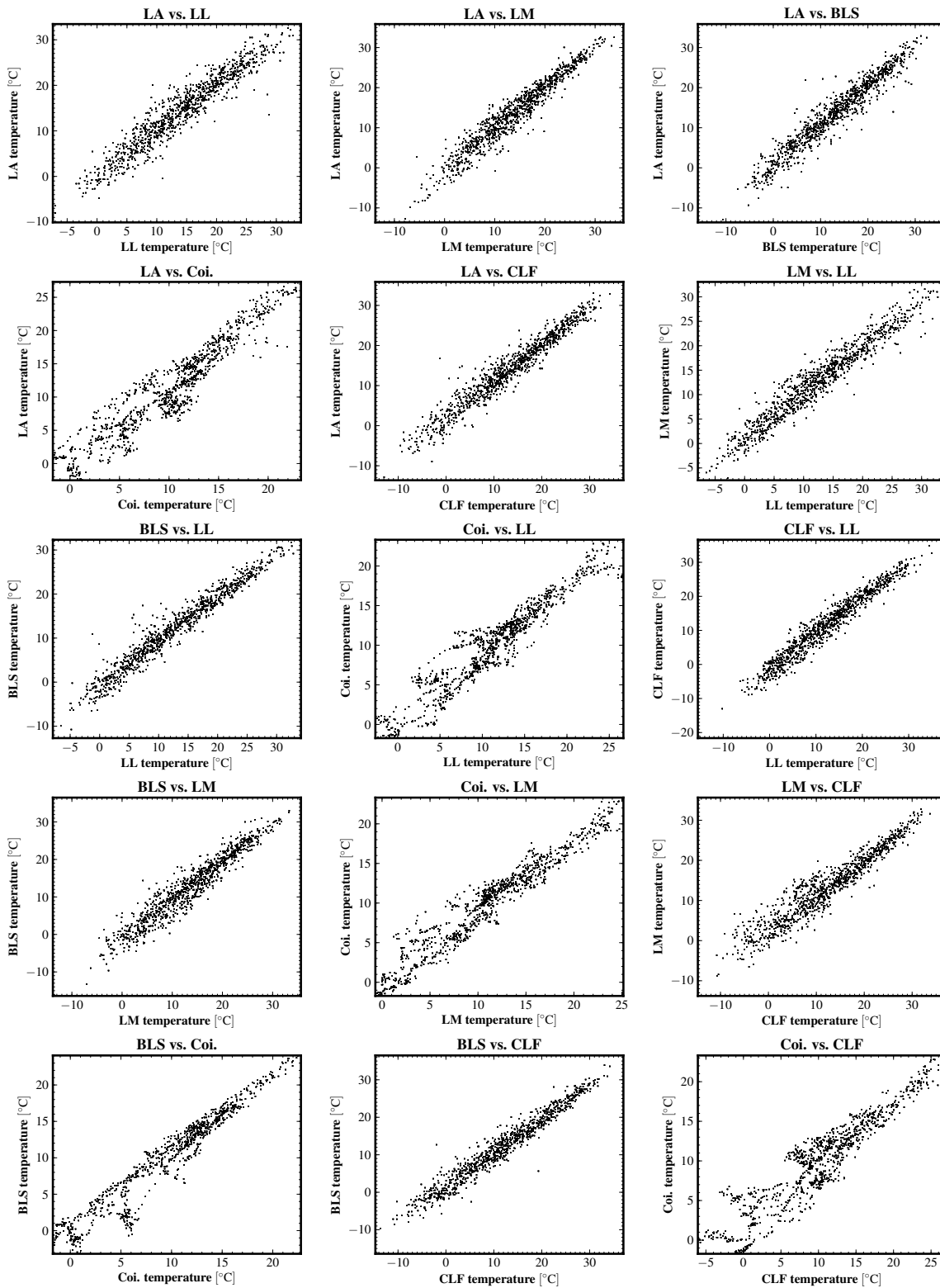
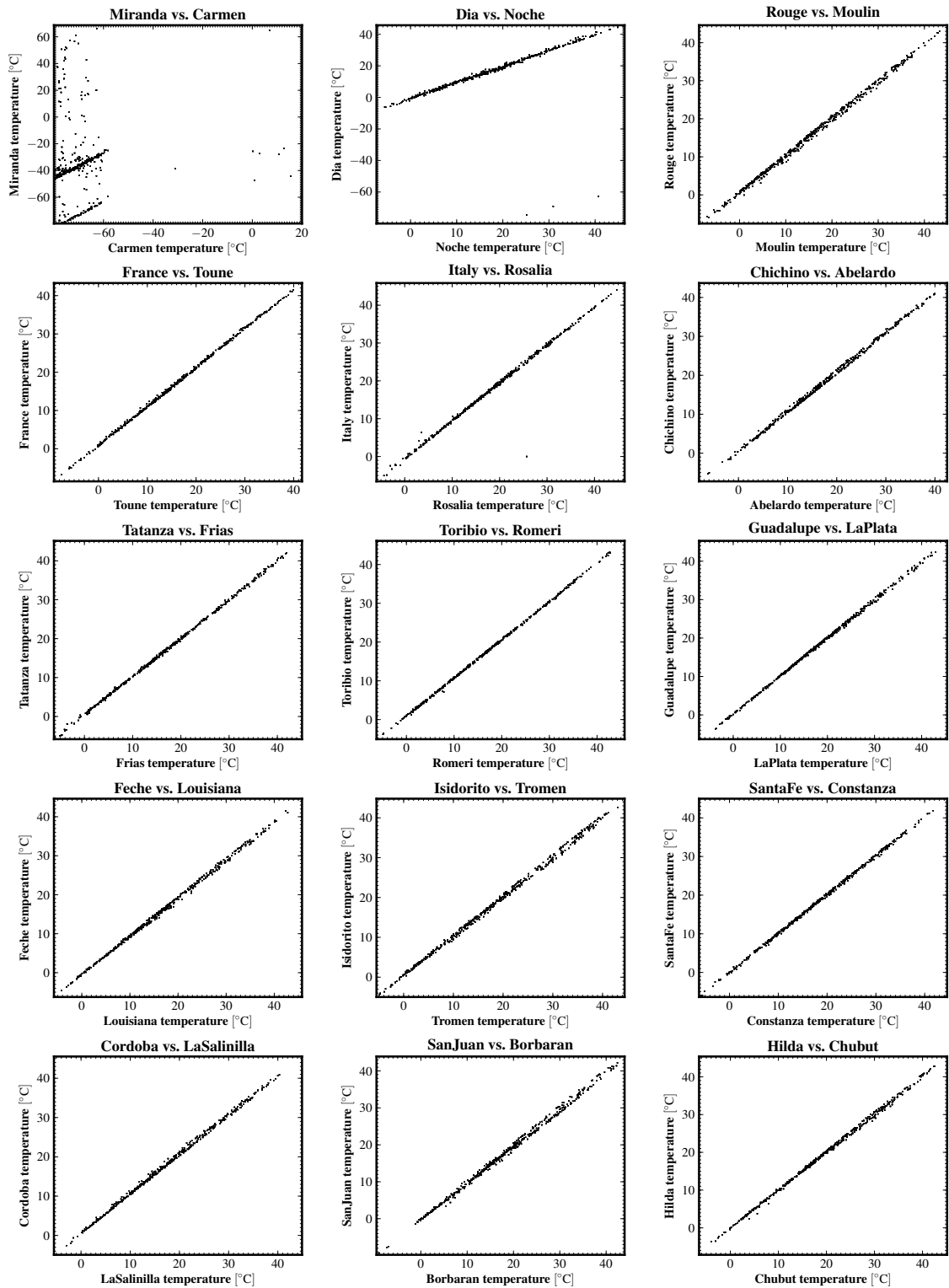
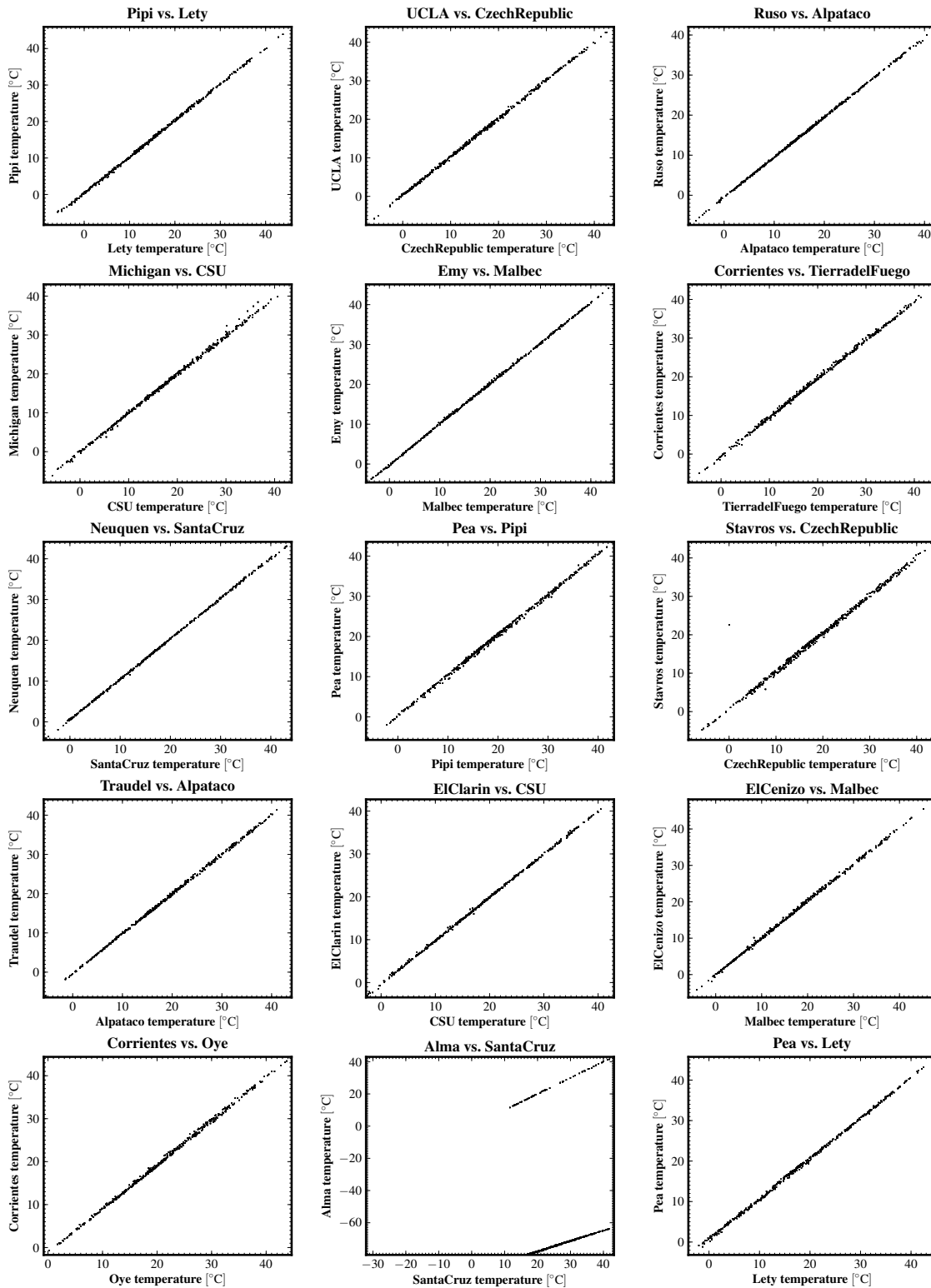


Figure C.4.: Correlation of temperatures as recorded by the weather stations.



**Figure C.5.:** Correlation of temperatures as recorded by the surface detector stations. Separate structures in the plots and unphysical values of the temperatures indicate a temporary malfunction of temperature sensors.



**Figure C.6.:** Correlation of temperatures as recorded by the surface detector stations (continued). Separate structures in the plots and unphysical values of the temperatures indicate a temporary malfunction of temperature sensors.

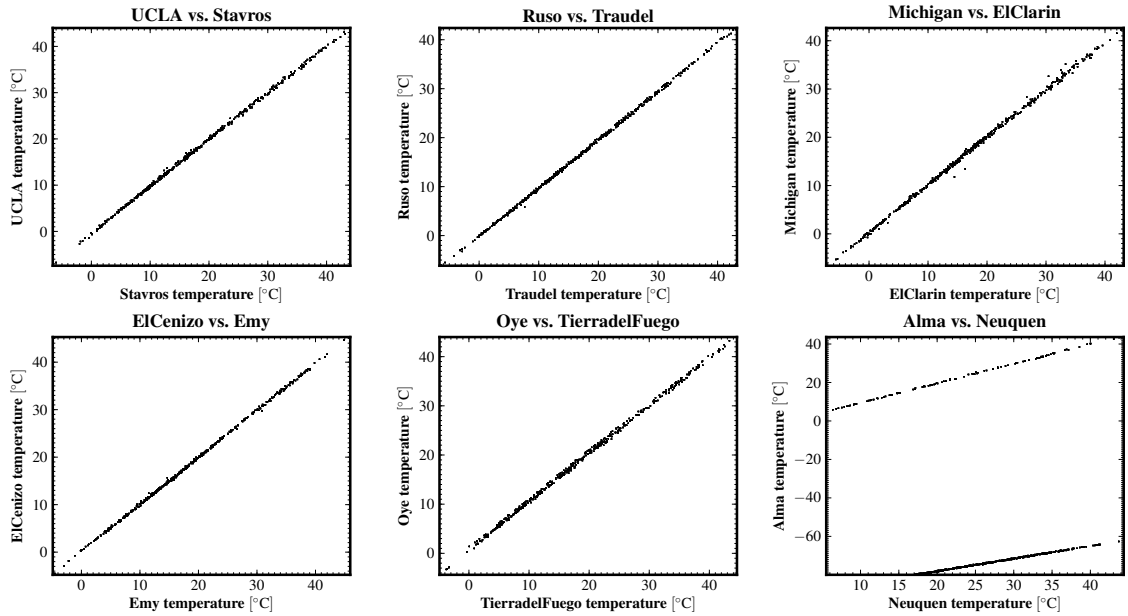


**Figure C.7.:** Correlation of temperatures as recorded by the surface detector stations (continued). Separate structures in the plots and unphysical values of the temperatures indicate a temporary malfunction of temperature sensors.

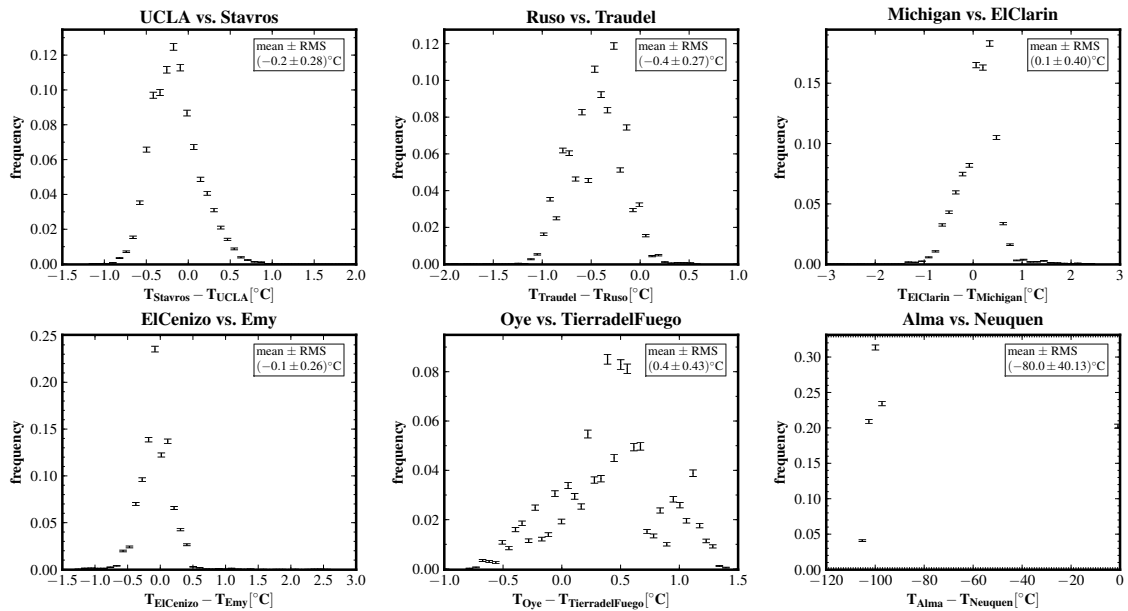


**Figure C.8.:** Temperature deviations between surface detector stations. Unphysical values of the temperatures recorded indicate a temporary malfunction of temperature sensors.

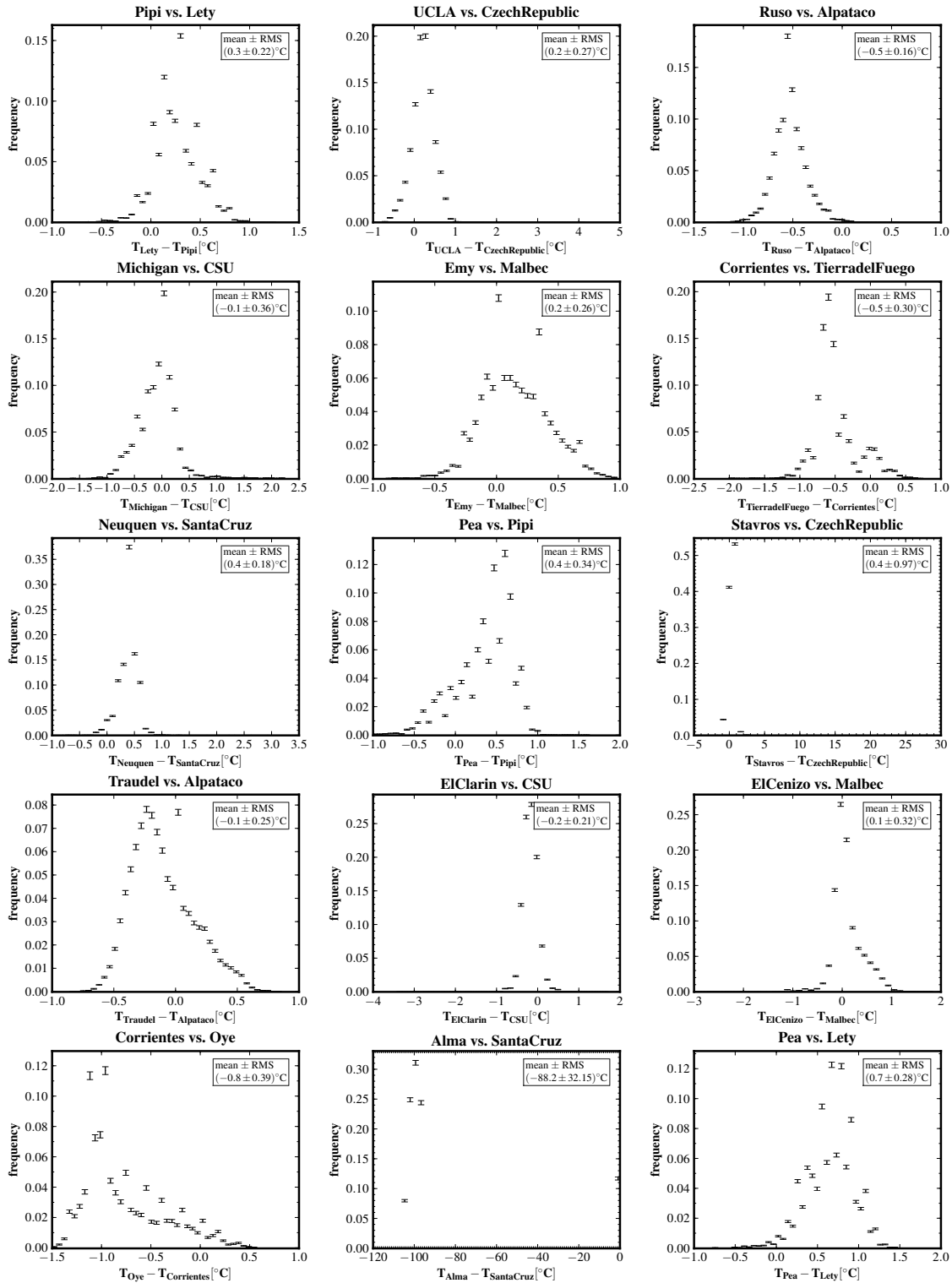


**Figure C.9.:** Temperature deviations between surface detector stations (continued). Unphysical values of the temperatures recorded indicate a temporary malfunction of temperature sensors.

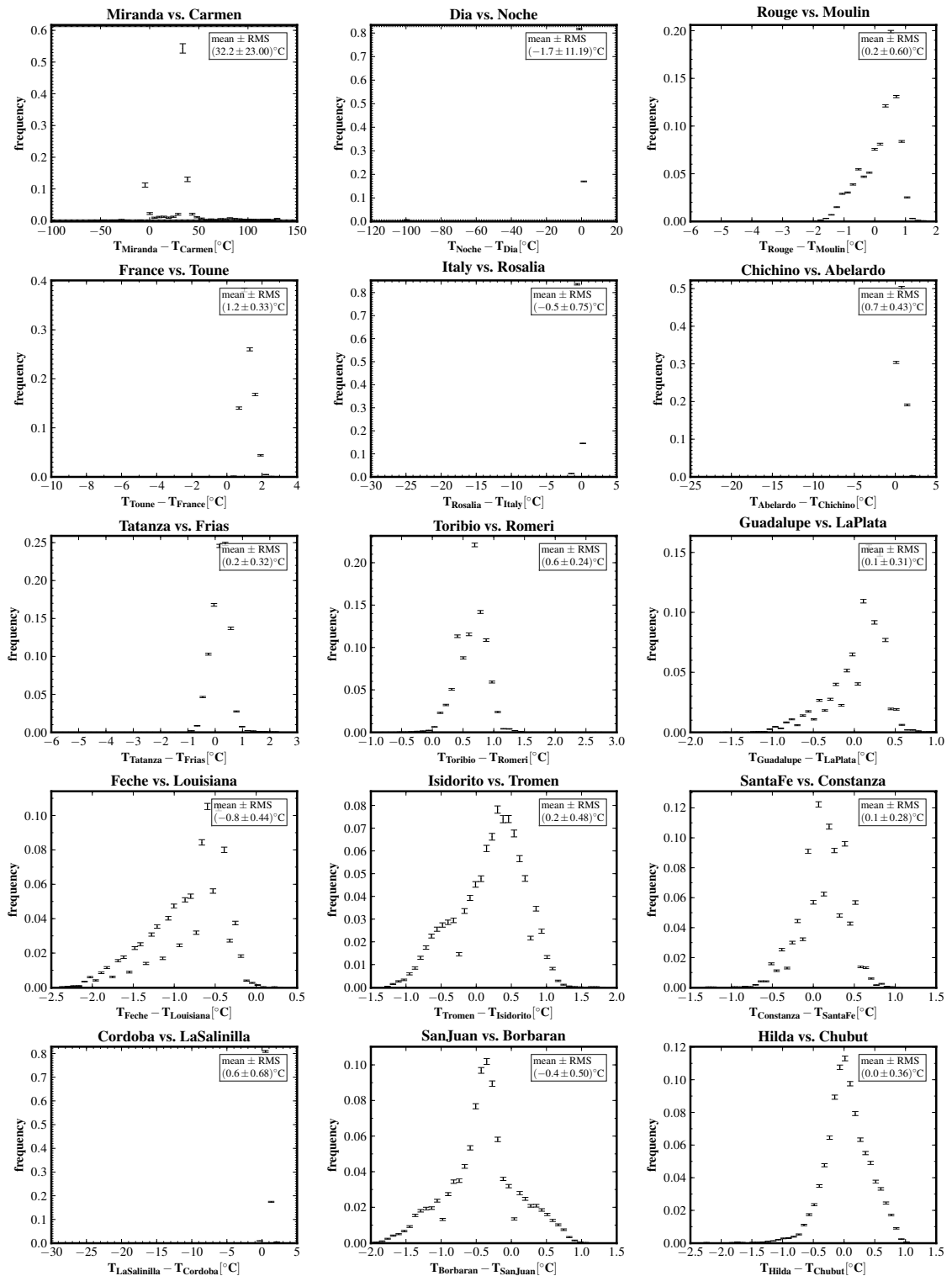


**Figure C.10.:** Temperature deviations between surface detector stations (continued). Unphysical values of the temperatures recorded indicate a temporary malfunction of temperature sensors.

# Appendix D

## Zenith Angle Uncertainties

To estimate the zenith angle uncertainty of the surface detector of the Pierre Auger Observatory at various energies and zenith angles, in total 200 extensive air showers were simulated using the AIRES (AIR-shower Extended Simulations) software package [Sci99], version 2.8.4a, and QGSJET-II [Ost06] as the hadronic interaction model. For each run, the steering parameters  $\Theta_{\text{MC}}$ , the zenith angle, and  $E_{\text{MC}}$ , the injection energy of the primary cosmic ray proton, were chosen to cover the range required for estimating the zenith angle reconstruction uncertainty. Thus, simulated extensive air showers were generated for zenith angles ranging from  $0^\circ$  to  $60^\circ$  and for energies ranging from 0.5 EeV, where the trigger efficiency amounts to  $\approx 20\%$  only, up to 3 EeV, where the surface detector array is nearly fully efficient (at the 97% level) [Abr09a].

The particle yield at ground level, obtained from the MC (Monte Carlo) simulation in AIRES, was then fed into a simulation model of the surface detector of the Pierre Auger Observatory, followed by a reconstruction of the air shower observables. In either stage, the Offline software framework [Arg07] of the Pierre Auger Observatory, version 2.6p2, was used. Each simulated air shower was reused up to ten times to provide the input data for the detector simulation; the position of the air shower core was chosen randomly. The reconstructed zenith angles, resulting from the full simulation and reconstruction chain, are listed in this appendix.

Tab. D.2 contains the results of the reconstructions for a simulated primary cosmic ray proton at an energy of  $E_{\text{MC}} = 0.5 \text{ EeV}$ . The results for  $E_{\text{MC}} = 1 \text{ EeV}$ ,  $E_{\text{MC}} = 2 \text{ EeV}$ , and  $E_{\text{MC}} = 3 \text{ EeV}$  are contained in Tab. D.3. The zenith angles  $\Theta_{\text{MC}}$  used as a steering parameter for AIRES were chosen such, that they subdivide the zenith angle distribution, as it is recorded by the surface detector, into portions containing equal numbers of events. See Tab. 5.2 for the values of  $\Theta_{\text{MC}}$  used.

The actual uncertainties of the zenith angle are determined as the square root of the second central moment of the zenith angle obtained from the reconstruction of the simulated air showers; see Tab. D.1 for the values.

In Figures D.1, D.2 and D.3, the histograms for the reconstruction results are shown. In addition, an estimate for the probability density function is plotted, using a Gaussian kernel density estimation (KDE) [Zha09, Sil98].

zenith angle $\Theta_{\text{MC}}$ [°]	energy $E_{\text{MC}}$ [EeV]			
	0.5	1.0	2.0	3.0
	uncertainty $\sigma_{\Theta}$ [°]			
23	1.7	1.2	1.2	1.0
33	2.0	1.7	1.3	0.8
42	1.3	1.1	0.9	0.7
50	1.6	1.0	2.4	0.8
60	0.9	1.1	0.7	0.5

**Table D.1.:** Zenith angle uncertainties for various energies  $E_{\text{MC}}$  and zenith angles  $\Theta_{\text{MC}}$ . The uncertainties have been calculated as the square root of the second central moment of the zenith angle distributions obtained from the simulation/reconstruction chain described in this appendix.



						<i>(continued from previous column)</i>					
$\Theta_{MC}$ [°]	23	33	42	50	60	$\Theta_{MC}$ [°]	23	33	42	50	60
reconstructed angle $\Theta_{reco}$ [°]						reconstructed angle $\Theta_{reco}$ [°]					
20.4	30.2	39.4	48.5	58.6		22.7	32.5	41.7	49.6	59.7	
20.5	30.5	39.7	48.5	58.9		22.7	32.6	41.7	49.6	59.7	
21.0	31.2	40.5	48.7	58.9		22.7	32.6	41.7	49.6	59.7	
21.2	31.2	40.6	48.7	58.9		22.7	32.7	41.7	49.7	59.8	
21.4	31.4	40.7	48.8	59.1		22.7	32.7	41.7	49.7	59.8	
21.4	31.5	40.8	48.8	59.1		22.7	32.7	41.7	49.7	59.8	
21.5	31.7	40.9	48.9	59.2		22.7	32.7	41.7	49.7	59.8	
21.6	31.9	40.9	48.9	59.2		22.7	32.8	41.7	49.7	59.8	
21.6	32.0	41.0	49.0	59.3		22.7	32.8	41.8	49.7	59.8	
21.6	32.0	41.1	49.0	59.3		22.8	32.8	41.8	49.7	59.9	
21.7	32.0	41.1	49.0	59.3		22.8	32.8	41.8	49.7	59.9	
21.9	32.1	41.2	49.1	59.3		22.8	32.8	41.8	49.8	59.9	
22.0	32.1	41.2	49.1	59.4		22.8	32.9	41.8	49.8	59.9	
22.1	32.1	41.2	49.2	59.4		22.8	32.9	41.8	49.8	59.9	
22.2	32.2	41.3	49.2	59.4		22.8	32.9	41.9	49.8	59.9	
22.3	32.2	41.3	49.2	59.4		22.8	32.9	41.9	49.8	59.9	
22.3	32.2	41.4	49.3	59.5		22.9	33.0	41.9	49.8	60.0	
22.3	32.2	41.4	49.3	59.5		22.9	33.0	41.9	49.8	60.0	
22.4	32.2	41.4	49.3	59.5		22.9	33.0	41.9	49.8	60.0	
22.4	32.2	41.4	49.3	59.5		22.9	33.0	41.9	49.8	60.0	
22.4	32.2	41.5	49.3	59.5		23.0	33.0	41.9	49.8	60.0	
22.4	32.2	41.5	49.4	59.5		23.0	33.0	41.9	49.8	60.0	
22.4	32.3	41.5	49.4	59.5		23.0	33.0	42.0	49.8	60.1	
22.4	32.3	41.5	49.4	59.5		23.1	33.0	42.0	49.8	60.1	
22.4	32.4	41.6	49.4	59.6		23.1	33.0	42.0	49.9	60.1	
22.5	32.4	41.6	49.4	59.6		23.1	33.0	42.1	49.9	60.1	
22.5	32.4	41.6	49.4	59.6		23.1	33.0	42.1	49.9	60.1	
22.6	32.5	41.6	49.4	59.6		23.1	33.1	42.1	49.9	60.1	
22.6	32.5	41.6	49.5	59.6		23.1	33.2	42.1	49.9	60.1	
22.6	32.5	41.6	49.5	59.6		23.2	33.2	42.1	49.9	60.2	
22.6	32.5	41.7	49.5	59.7		23.2	33.2	42.1	49.9	60.2	
22.6	32.5	41.7	49.5	59.7		23.2	33.2	42.2	49.9	60.2	
22.6	32.5	41.7	49.5	59.7		23.2	33.2	42.2	50.0	60.2	
						23.3	33.2	42.2	50.0	60.2	
						23.3	33.2	42.2	50.0	60.2	
						23.3	33.3	42.2	50.0	60.2	

*(continued in next column)*

*(continued in next column)*

*(continued from previous column)*

$\Theta_{\text{MC}} [^\circ]$	23	33	42	50	60
	reconstructed angle $\Theta_{\text{reco}} [^\circ]$				
23.4	33.3	42.3	50.0	60.2	
23.4	33.3	42.3	50.0	60.2	
23.4	33.4	42.3	50.0	60.2	
23.4	33.4	42.3	50.1	60.2	
23.4	33.4	42.3	50.1	60.2	
23.5	33.4	42.4	50.1	60.2	
23.5	33.4	42.4	50.1	60.2	
23.6	33.5	42.5	50.1	60.3	
23.6	33.5	42.5	50.1	60.3	
23.7	33.5	42.5	50.1	60.3	
23.7	33.5	42.7	50.2	60.3	
23.7	33.6	42.7	50.2	60.3	
23.8	33.7	42.8	50.2	60.4	
23.9	33.7	42.9	50.2	60.4	
24.0	33.7	42.9	50.2	60.4	
24.0	33.7	42.9	50.2	60.4	
24.1	33.7	43.0	50.3	60.4	
24.1	33.7	43.0	50.3	60.4	
24.1	33.8	43.0	50.4	60.4	
24.2	33.8	43.1	50.4	60.4	
24.2	33.8	43.6	50.4	60.4	
24.4	33.8		50.4	60.6	
24.7	33.9		50.5	60.6	
25.9	33.9		50.5	60.6	
26.8	34.1		50.7	60.7	
	34.2		50.9	60.7	
	34.3		50.9	60.7	
	34.3		51.0	60.7	
	34.3		51.4	61.1	
	35.1		51.8	61.2	
	35.3		54.8	62.3	

**Table D.2.:** Reconstructed zenith angles for simulated extensive air showers at  $E_{\text{MC}} = 0.5 \text{ EeV}$ . The reconstructed angles are rounded according to their mean uncertainty reported by the reconstruction procedure ( $\mathcal{O}(\sigma_{\Theta}) \approx 0.5^\circ$ ). Empty cells indicate, that either the simulated extensive air shower did not fulfill the trigger requirement of the simulated surface detector or its reconstruction was not possible.

$E_{MC}$	1 EeV					2 EeV					3 EeV				
$\Theta_{MC}$ [°]	23	33	42	50	60	23	33	42	50	60	23	33	42	50	60
reconstructed angle $\Theta_{reco}$ [°]															
19.7	29.2	35.6	47.3	58.1	20.0	30.1	40.3	47.3	57.3	20.4	30.2	39.4	48.5	58.6	
19.7	29.7	40.0	47.4	58.6	20.3	30.5	40.4	47.9	58.7	20.5	30.5	39.7	48.5	58.9	
20.8	30.9	40.1	47.8	58.6	20.5	30.5	40.5	48.3	58.8	21.0	31.2	40.5	48.7	58.9	
20.9	30.9	40.2	47.9	58.9	20.7	30.9	40.9	48.6	58.9	21.2	31.2	40.6	48.7	58.9	
20.9	31.3	40.2	48.1	58.9	21.1	31.3	41.0	48.7	58.9	21.4	31.4	40.7	48.8	59.1	
21.1	31.3	40.3	48.1	59.0	21.2	31.5	41.1	48.7	59.0	21.4	31.5	40.8	48.8	59.1	
21.1	31.3	40.3	48.3	59.0	21.6	31.7	41.1	48.8	59.0	21.5	31.7	40.9	48.9	59.2	
21.3	31.4	40.3	48.3	59.1	21.6	31.7	41.2	48.8	59.2	21.6	31.9	40.9	48.9	59.2	
21.4	31.5	40.4	48.7	59.2	21.8	31.8	41.2	48.8	59.2	21.6	32.0	41.0	49.0	59.3	
21.5	31.5	40.5	48.8	59.2	21.9	31.9	41.3	49.0	59.2	21.6	32.0	41.1	49.0	59.3	
21.6	31.6	40.5	48.8	59.2	22.0	32.0	41.3	49.0	59.3	21.7	32.0	41.1	49.0	59.3	
21.7	31.6	40.7	48.9	59.2	22.1	32.1	41.4	49.0	59.3	21.9	32.1	41.2	49.1	59.3	
21.8	31.7	40.8	48.9	59.2	22.1	32.1	41.4	49.1	59.4	22.0	32.1	41.2	49.1	59.4	
21.8	31.8	40.8	48.9	59.2	22.1	32.1	41.4	49.1	59.4	22.1	32.1	41.2	49.2	59.4	
21.8	31.9	40.9	49.0	59.2	22.2	32.2	41.5	49.1	59.4	22.2	32.2	41.3	49.2	59.4	
21.9	31.9	40.9	49.1	59.2	22.2	32.2	41.5	49.2	59.5	22.3	32.2	41.3	49.2	59.4	
21.9	31.9	41.0	49.1	59.3	22.3	32.4	41.5	49.2	59.5	22.3	32.2	41.4	49.3	59.5	
22.0	32.0	41.1	49.1	59.3	22.3	32.4	41.5	49.2	59.5	22.3	32.2	41.4	49.3	59.5	
22.2	32.0	41.1	49.2	59.4	22.3	32.4	41.6	49.3	59.5	22.4	32.2	41.4	49.3	59.5	
22.2	32.1	41.2	49.2	59.4	22.3	32.4	41.6	49.3	59.7	22.4	32.2	41.4	49.3	59.5	
22.2	32.1	41.2	49.2	59.4	22.3	32.4	41.6	49.3	59.7	22.4	32.2	41.5	49.3	59.5	

(continued on next page)

(continued from previous page)

$E_{MC}$	1 EeV					2 EeV					3 EeV				
$\Theta_{MC}$ [°]	23	33	42	50	60	23	33	42	50	60	23	33	42	50	60
reconstructed angle $\Theta_{reco}$ [°]															
22.3	32.2	41.2	49.3	59.5	22.4	32.4	41.6	49.3	59.7	22.4	32.2	41.5	49.4	59.5	
22.4	32.2	41.2	49.3	59.5	22.4	32.4	41.6	49.4	59.7	22.4	32.3	41.5	49.4	59.5	
22.4	32.2	41.3	49.3	59.6	22.4	32.5	41.7	49.4	59.7	22.4	32.3	41.5	49.4	59.5	
22.5	32.3	41.3	49.3	59.6	22.4	32.5	41.7	49.4	59.7	22.4	32.4	41.6	49.4	59.6	
22.5	32.3	41.3	49.4	59.6	22.5	32.5	41.7	49.5	59.7	22.5	32.4	41.6	49.4	59.6	
22.5	32.3	41.3	49.4	59.6	22.5	32.6	41.7	49.5	59.7	22.5	32.4	41.6	49.4	59.6	
22.5	32.3	41.3	49.4	59.6	22.5	32.6	41.7	49.5	59.7	22.6	32.5	41.6	49.4	59.6	
22.5	32.3	41.4	49.4	59.7	22.6	32.7	41.7	49.6	59.7	22.6	32.5	41.6	49.5	59.6	
22.6	32.4	41.4	49.4	59.7	22.6	32.7	41.7	49.6	59.8	22.6	32.5	41.6	49.5	59.6	
22.6	32.5	41.5	49.5	59.7	22.6	32.7	41.7	49.7	59.8	22.6	32.5	41.7	49.5	59.7	
22.6	32.5	41.5	49.5	59.7	22.6	32.7	41.7	49.7	59.8	22.6	32.5	41.7	49.5	59.7	
22.6	32.5	41.5	49.5	59.8	22.7	32.7	41.8	49.8	59.8	22.6	32.5	41.7	49.5	59.7	
22.6	32.6	41.5	49.5	59.8	22.7	32.7	41.8	49.8	59.8	22.7	32.5	41.7	49.6	59.7	
22.6	32.6	41.5	49.5	59.8	22.7	32.7	41.8	49.8	59.9	22.7	32.6	41.7	49.6	59.7	
22.7	32.6	41.5	49.6	59.8	22.7	32.8	41.8	49.8	59.9	22.7	32.6	41.7	49.6	59.7	
22.7	32.6	41.6	49.6	59.8	22.8	32.8	41.8	49.8	59.9	22.7	32.7	41.7	49.7	59.8	
22.7	32.7	41.6	49.6	59.8	22.8	32.8	41.9	49.8	59.9	22.7	32.7	41.7	49.7	59.8	
22.7	32.7	41.6	49.6	59.9	22.8	32.8	41.9	49.9	59.9	22.7	32.7	41.7	49.7	59.8	
22.7	32.7	41.6	49.6	60.0	22.9	32.8	41.9	49.9	59.9	22.7	32.7	41.7	49.7	59.8	
22.8	32.7	41.7	49.6	60.0	22.9	32.8	41.9	49.9	59.9	22.7	32.8	41.7	49.7	59.8	
22.8	32.7	41.7	49.7	60.0	22.9	32.9	41.9	49.9	59.9	22.7	32.8	41.8	49.7	59.8	
22.8	32.7	41.7	49.7	60.0	22.9	32.9	41.9	49.9	59.9	22.8	32.8	41.8	49.7	59.9	
22.8	32.8	41.7	49.7	60.0	23.0	32.9	42.0	49.9	59.9	22.8	32.8	41.8	49.7	59.9	
22.8	32.8	41.7	49.8	60.1	23.0	32.9	42.0	49.9	59.9	22.8	32.8	41.8	49.8	59.9	

(continued on next page)

(continued from previous page)

$E_{MC}$	1 EeV					2 EeV					3 EeV				
$\Theta_{MC}$ [°]	23	33	42	50	60	23	33	42	50	60	23	33	42	50	60
reconstructed angle $\Theta_{reco}$ [°]															
	22.9	32.8	41.7	49.8	60.1	23.0	33.0	42.0	49.9	60.0	22.8	32.9	41.8	49.8	59.9
	22.9	32.9	41.7	49.9	60.1	23.0	33.0	42.0	50.0	60.0	22.8	32.9	41.8	49.8	59.9
	22.9	32.9	41.7	49.9	60.1	23.1	33.0	42.0	50.0	60.0	22.8	32.9	41.9	49.8	59.9
	22.9	32.9	41.8	49.9	60.1	23.1	33.0	42.1	50.0	60.0	22.8	32.9	41.9	49.8	59.9
	23.0	32.9	41.8	49.9	60.1	23.1	33.0	42.1	50.0	60.0	22.9	33.0	41.9	49.8	60.0
	23.0	33.0	41.8	49.9	60.1	23.1	33.0	42.1	50.0	60.0	22.9	33.0	41.9	49.8	60.0
	23.0	33.0	41.9	50.0	60.2	23.1	33.0	42.1	50.0	60.0	22.9	33.0	41.9	49.8	60.0
	23.0	33.0	41.9	50.1	60.2	23.1	33.1	42.1	50.0	60.0	22.9	33.0	41.9	49.8	60.0
	23.0	33.0	42.0	50.1	60.2	23.1	33.1	42.1	50.1	60.0	23.0	33.0	41.9	49.8	60.0
	23.1	33.0	42.0	50.1	60.2	23.2	33.1	42.1	50.1	60.1	23.0	33.0	41.9	49.8	60.0
	23.1	33.1	42.0	50.2	60.3	23.2	33.1	42.1	50.1	60.1	23.0	33.0	42.0	49.8	60.1
	23.1	33.1	42.0	50.2	60.3	23.2	33.1	42.1	50.1	60.1	23.1	33.0	42.0	49.8	60.1
	23.1	33.1	42.0	50.2	60.4	23.2	33.1	42.2	50.1	60.2	23.1	33.0	42.0	49.9	60.1
	23.1	33.1	42.1	50.2	60.4	23.3	33.2	42.2	50.1	60.2	23.1	33.0	42.1	49.9	60.1
	23.2	33.1	42.1	50.3	60.4	23.3	33.2	42.2	50.1	60.2	23.1	33.0	42.1	49.9	60.1
	23.2	33.3	42.1	50.3	60.4	23.3	33.2	42.3	50.2	60.2	23.1	33.1	42.1	49.9	60.1
	23.2	33.3	42.1	50.3	60.4	23.4	33.2	42.3	50.2	60.3	23.1	33.2	42.1	49.9	60.1
	23.2	33.3	42.1	50.3	60.4	23.4	33.2	42.3	50.2	60.3	23.2	33.2	42.1	49.9	60.2
	23.2	33.3	42.2	50.3	60.5	23.4	33.2	42.3	50.2	60.3	23.2	33.2	42.1	49.9	60.2
	23.3	33.3	42.2	50.4	60.5	23.4	33.3	42.3	50.2	60.3	23.2	33.2	42.2	49.9	60.2
	23.3	33.3	42.2	50.4	60.6	23.6	33.3	42.3	50.2	60.3	23.2	33.2	42.2	50.0	60.2
	23.3	33.3	42.2	50.4	60.6	23.6	33.3	42.3	50.2	60.4	23.3	33.2	42.2	50.0	60.2
	23.4	33.4	42.2	50.4	60.6	23.6	33.3	42.4	50.2	60.4	23.3	33.2	42.2	50.0	60.2
	23.4	33.4	42.2	50.5	60.7	23.7	33.3	42.4	50.3	60.4	23.3	33.3	42.2	50.0	60.2

(continued on next page)

(continued from previous page)

$E_{MC}$	1 EeV					2 EeV					3 EeV				
$\Theta_{MC}$ [°]	23	33	42	50	60	23	33	42	50	60	23	33	42	50	60
reconstructed angle $\Theta_{reco}$ [°]															
23.4	33.5	42.2	50.6	60.7	23.7	33.3	42.5	50.3	60.5	23.4	33.3	42.3	50.0	60.2	
23.5	33.5	42.3	50.7	60.9	23.7	33.4	42.5	50.3	60.5	23.4	33.3	42.3	50.0	60.2	
23.5	33.5	42.3	50.7	61.0	23.8	33.4	42.5	50.4	60.5	23.4	33.4	42.3	50.0	60.2	
23.5	33.6	42.3	50.7	61.0	23.8	33.4	42.5	50.4	60.5	23.4	33.4	42.3	50.1	60.2	
23.5	33.6	42.3	50.7	61.1	23.8	33.5	42.6	50.5	60.5	23.4	33.4	42.3	50.1	60.2	
23.5	33.6	42.4	50.7	61.1	23.8	33.6	42.6	50.5	60.6	23.5	33.4	42.4	50.1	60.2	
23.6	33.7	42.4	50.8	61.2	23.9	33.6	42.6	50.5	60.6	23.5	33.4	42.4	50.1	60.2	
23.8	33.7	42.4	50.8	61.2	23.9	33.6	42.7	50.6	60.7	23.6	33.5	42.5	50.1	60.3	
23.8	33.7	42.4	50.8	61.3	24.0	33.6	42.7	50.6	60.7	23.6	33.5	42.5	50.1	60.3	
23.8	33.7	42.5	50.8	61.3	24.0	33.7	42.7	50.8	60.7	23.7	33.5	42.5	50.1	60.3	
23.9	33.8	42.5	50.9	61.4	24.0	33.7	42.7	50.8	60.7	23.7	33.5	42.7	50.2	60.3	
23.9	33.8	42.6	50.9	61.5	24.0	33.8	42.7	50.9	60.8	23.7	33.6	42.7	50.2	60.3	
24.0	33.8	42.7	50.9	61.6	24.0	33.8	42.7	51.0	60.8	23.8	33.7	42.8	50.2	60.4	
24.0	33.9	42.7	51.1	61.9	24.2	33.8	42.8	51.0	60.8	23.9	33.7	42.9	50.2	60.4	
24.0	34.0	42.7	51.1	61.9	24.2	34.0	42.8	51.1	60.8	24.0	33.7	42.9	50.2	60.4	
24.0	34.0	42.7	51.1	62.1	24.2	34.0	42.8	51.1	60.9	24.0	33.7	42.9	50.2	60.4	
24.1	34.1	42.7	51.1	67.6	24.2	34.1	42.9	51.2	60.9	24.1	33.7	43.0	50.3	60.4	
24.1	34.2	42.8	51.2		24.2	34.1	42.9	51.2	60.9	24.1	33.7	43.0	50.3	60.4	
24.2	34.2	42.8	51.2		24.3	34.2	42.9	52.9	61.1	24.1	33.8	43.0	50.4	60.4	
24.3	34.3	42.9	51.4		24.3	34.3	42.9	57.0	61.2	24.2	33.8	43.1	50.4	60.4	
24.5	34.9	43.0	51.5		24.3	34.3	42.9	70.1	61.4	24.2	33.8	43.6	50.4	60.4	
24.6	34.9	43.0	51.6		24.4	34.4	43.2		61.4	24.4	33.8		50.4	60.6	
24.7	35.0	43.1	51.6		24.5	34.4	43.2		61.5	24.7	33.9		50.5	60.6	
24.8	35.0	43.2	52.0		24.6	34.5	43.3		61.7	25.9	33.9		50.5	60.6	

(continued on next page)

(continued from previous page)

$E_{MC}$	1 EeV					2 EeV					3 EeV				
$\Theta_{MC}$ [°]	23	33	42	50	60	23	33	42	50	60	23	33	42	50	60
	reconstructed angle $\Theta_{reco}$ [°]														
	24.9	35.1	43.2	52.1		24.7	34.9	43.3		61.9	26.8	34.1		50.7	60.7
	24.9	35.4	43.3	52.6		24.7	35.1	43.4		62.5		34.2		50.9	60.7
	24.9	36.0	43.3			25.0	35.7	43.5				34.3		50.9	60.7
	24.9	36.8	43.4			25.0	36.4	43.9				34.3		51.0	60.7
	25.0	45.7	43.5			25.1	36.5	44.2				34.3		51.4	61.1
	25.9		43.9			26.2	37.2	44.3				35.1		51.8	61.2
	27.0		44.4			27.9	40.4	47.4				35.3		54.8	62.3

**Table D.3.:** Reconstructed zenith angles for simulated extensive air showers at  $E_{MC} = 1\text{EeV}$ ,  $E_{MC} = 2\text{EeV}$ , and  $E_{MC} = 3\text{EeV}$ , respectively. The reconstructed angles are rounded according to their mean uncertainty reported by the reconstruction procedure ( $\mathcal{O}(\sigma_{\Theta}) \approx 0.5^\circ$ ). Empty cells indicate, that either the simulated extensive air shower did not fulfill the trigger requirement of the simulated surface detector or its reconstruction was not possible.

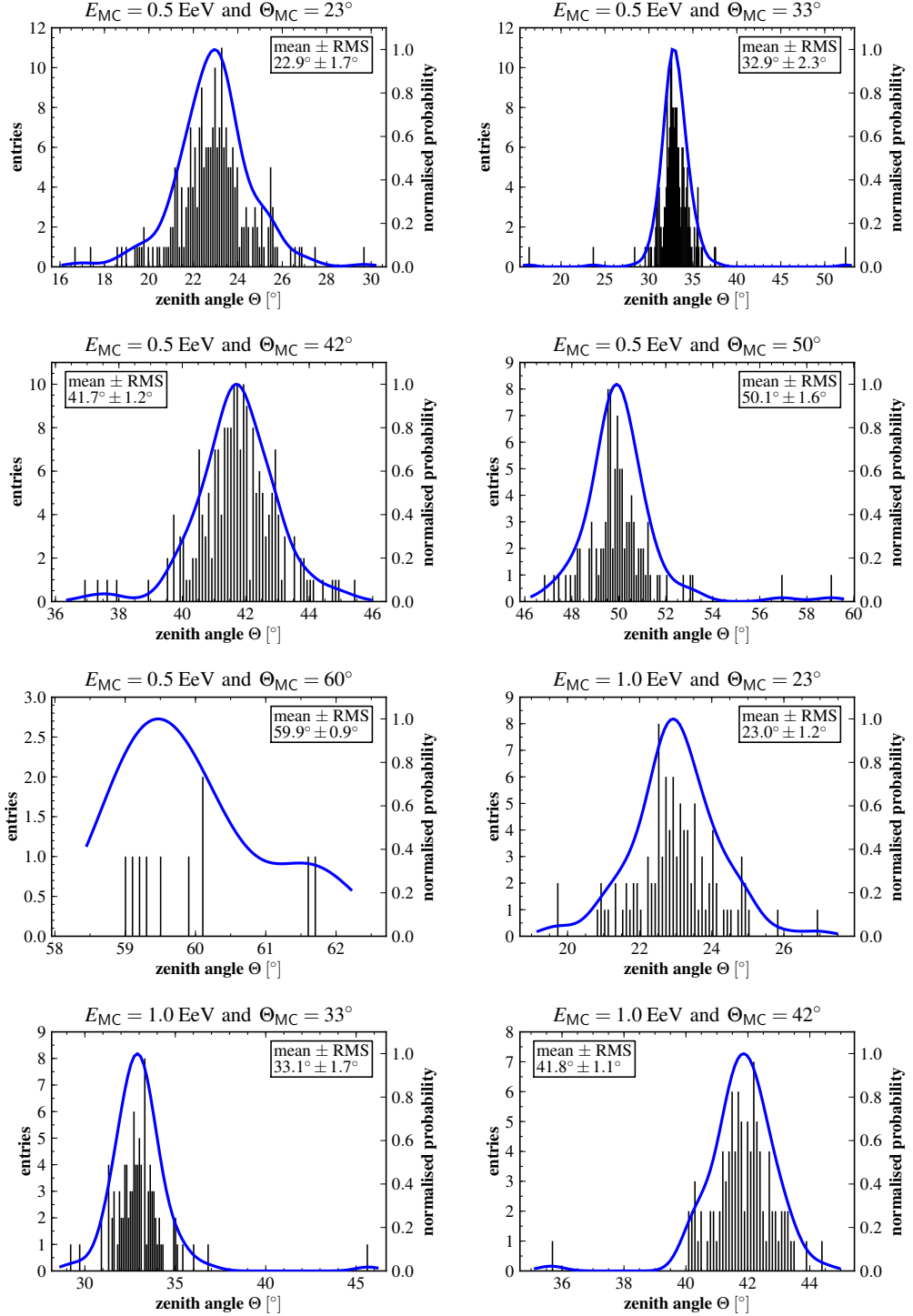


**Figure D.1.:** Reconstructed zenith angles for various energies  $E_{MC}$  and various zenith angles  $\Theta_{MC}$  of the simulated extensive air showers. The frequencies of air shower events reconstructed at a certain angle are shown as histograms (left axes). An estimate of the underlying probability density is indicated by a blue, solid line (right axes).



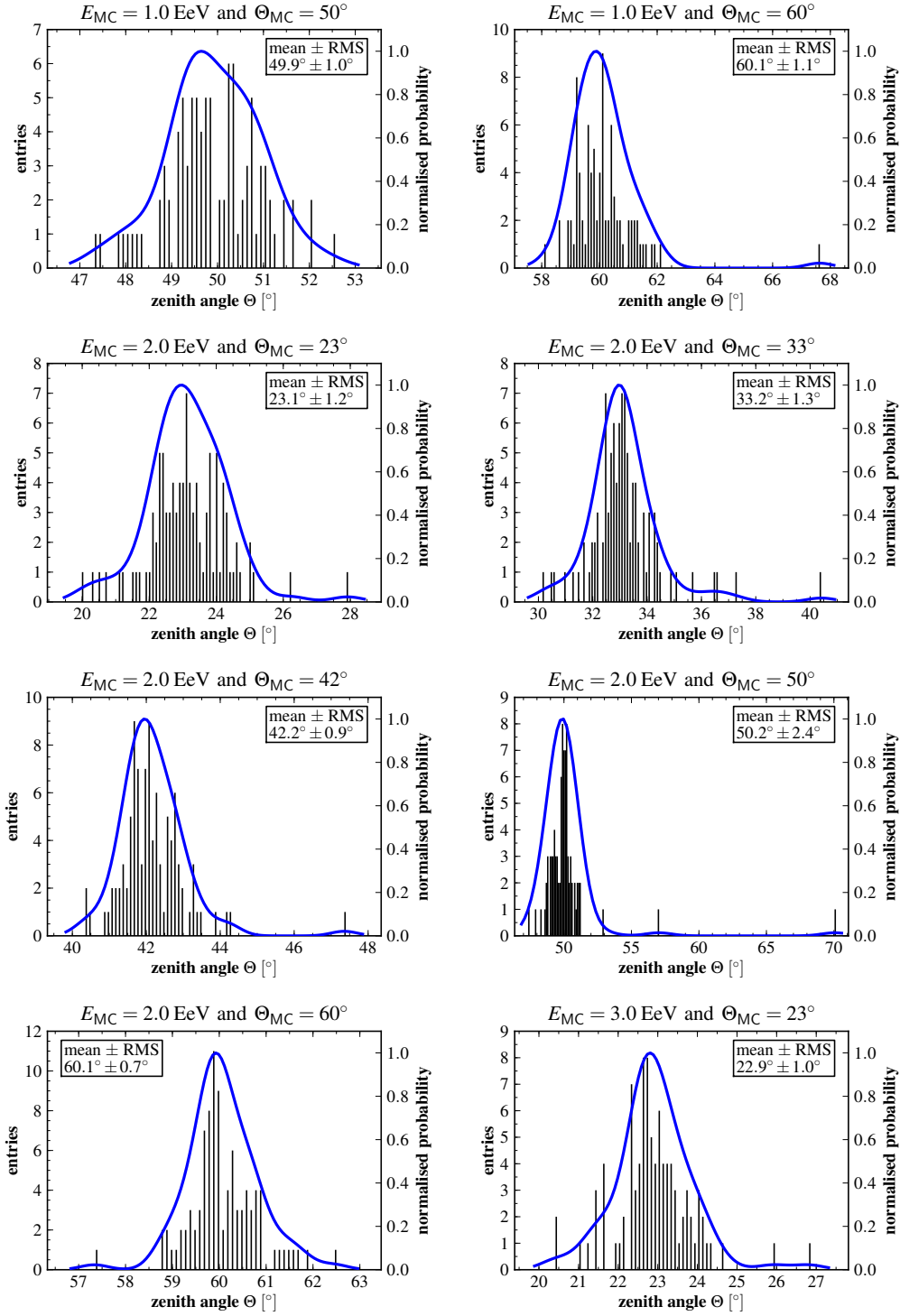


**Figure D.2.:** Reconstructed zenith angles for various energies  $E_{MC}$  and various zenith angles  $\Theta_{MC}$  of the simulated extensive air showers (continued). The frequencies of air shower events reconstructed at a certain angle are shown as histograms (left axes). An estimate of the underlying probability density is indicated by a blue, solid line (right axes).

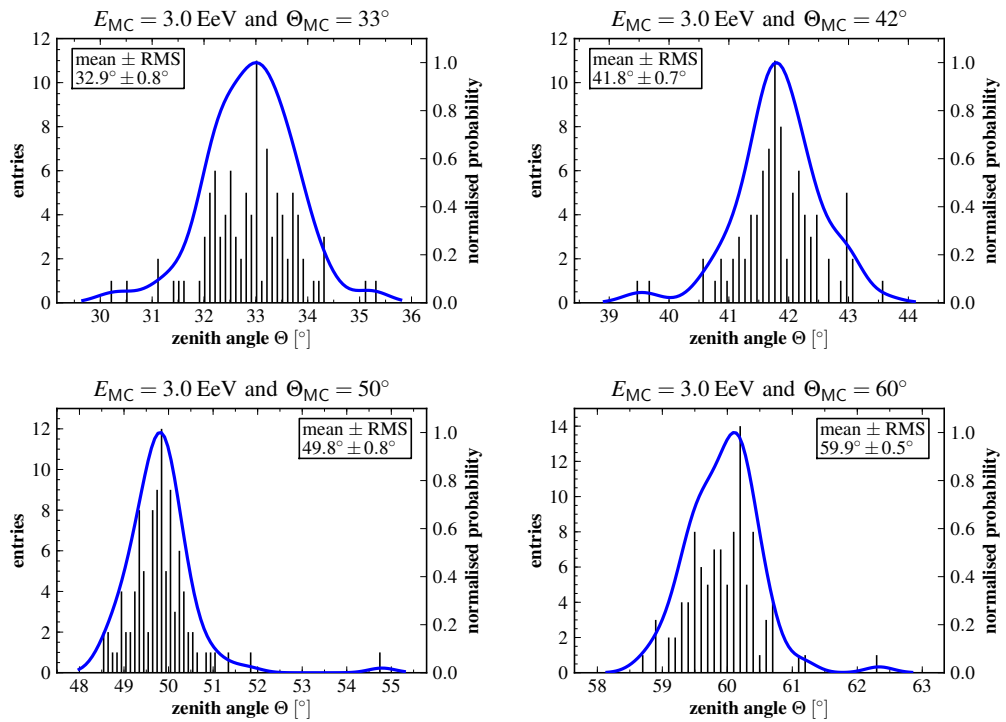


**Figure D.3.:** Reconstructed zenith angles for various energies  $E_{MC}$  and various zenith angles  $\Theta_{MC}$  of the simulated extensive air showers (continued). The frequencies of air shower events reconstructed at a certain angle are shown as histograms (left axes). An estimate of the underlying probability density is indicated by a blue, solid line (right axes).

# Appendix E

## Zenith Angle Distributions

This appendix contains the comparisons of the zenith angle distributions of events at temperatures below and above the median temperature. These are the results after applying the corrections described in Section 5.2 to datasets corresponding to a lower energy cut of 1.0 EeV, 2.0 EeV, and 3.0 EeV, respectively.

In Tab. E.1, the parameter results of the correction procedure, described in Section 5.2, are listed. The table also contains the results of tests for side effects of the correction procedure.

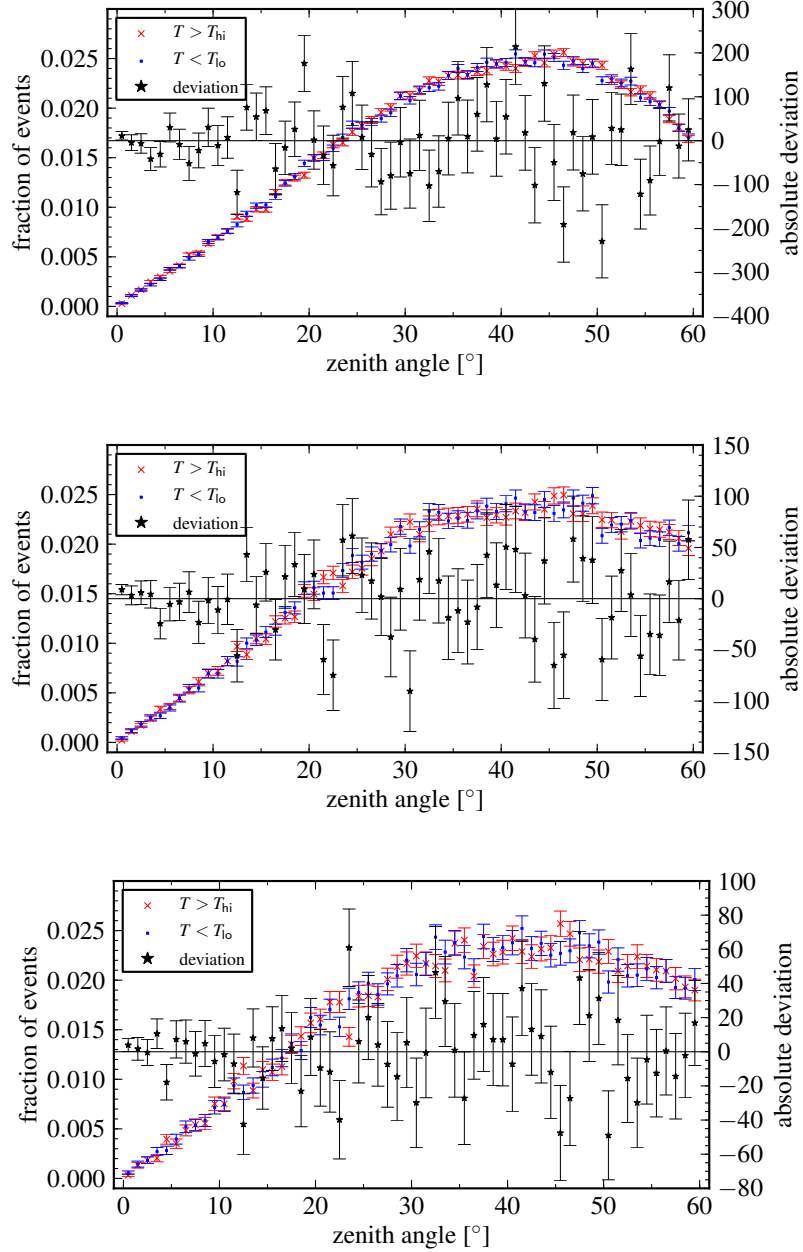


**Figure E.1.:** Zenith angle distributions for high temperatures ( $T > T_{hi}$ ) and low temperatures ( $T < T_{lo}$ ), respectively, with  $T_{hi} = T_{lo} = T_{med}$ ;  $T_{med} \approx 285.3\text{K}$  denotes the median temperature of the surface detector events. The fraction of events in the corresponding zenith angle bin is plotted, using cross and dot markers, for both subsamples (ordinate on the left-hand side). The star shaped markers indicate the absolute deviation of the numbers of events in both subsamples for each zenith angle bin (ordinate on the right-hand side). These plots contain the results after applying the corrections, described in Section 5.2. *From top to bottom:* Results for  $E > 1.0\text{EeV}$ ,  $E > 2.0\text{EeV}$ , and  $E > 3.0\text{EeV}$ , respectively.

E [EeV]	$p_E$	$\Delta N_{p_E}$ [%]	$\chi_\phi^2$	$\chi_{\phi,\text{crit}}^2$	$\Delta E^{(\text{max})}$	$\Delta E^{(\text{mean})}$	$\Delta E^{(25\%)}$	$\Delta E^{(50\%)}$	$\Delta E^{(75\%)}$
0.50	$0.795 \pm 0.006$	$1.654^{+0.002}_{-0.005}$	108.25	244.22	0.10	$0.0191^{+0.0001}_{-0.0001}$	0.01	0.02	0.02
0.55	$0.857 \pm 0.009$	$1.642^{+0.005}_{-0.008}$	95.71	244.22	0.11	$0.0205^{+0.0002}_{-0.0001}$	0.01	0.02	0.03
0.60	$0.869 \pm 0.009$	$1.594^{+0.003}_{-0.007}$	81.89	244.22	0.11	$0.0209^{+0.0001}_{-0.0001}$	0.01	0.02	0.03
0.65	$0.909 \pm 0.009$	$1.570^{+0.008}_{-0.010}$	72.94	244.22	0.11	$0.0217^{+0.0002}_{-0.0002}$	0.01	0.02	0.03
0.70	$0.970 \pm 0.010$	$1.591^{+0.004}_{-0.006}$	68.50	244.22	0.12	$0.0227^{+0.0002}_{-0.0001}$	0.01	0.02	0.03
0.75	$0.985 \pm 0.010$	$1.547^{+0.011}_{-0.008}$	59.51	244.22	0.12	$0.0231^{+0.0002}_{-0.0002}$	0.01	0.02	0.03
0.80	$0.947 \pm 0.010$	$1.500^{+0.003}_{-0.007}$	51.55	244.22	0.12	$0.0222^{+0.0002}_{-0.0002}$	0.01	0.02	0.03
0.85	$1.00 \pm 0.01$	$1.546^{+0.001}_{-0.007}$	50.15	244.22	0.13	$0.0230^{+0.0002}_{-0.0002}$	0.01	0.02	0.03
0.90	$1.10 \pm 0.02$	$1.54^{+0.01}_{-0.01}$	45.78	244.22	$0.14_{-0.02}$	$0.0248^{+0.0003}_{-0.0003}$	0.01	0.02	0.03
0.95	$1.21 \pm 0.02$	$1.532^{+0.010}_{-0.008}$	42.50	244.22	0.15	$0.0272^{+0.0003}_{-0.0002}$	0.01	0.02	0.04
1.00	$1.27 \pm 0.02$	$1.486^{+0.008}_{-0.006}$	36.88	244.22	0.16	$0.0283^{+0.0003}_{-0.0004}$	0.01	0.02	0.04
1.05	$1.27 \pm 0.02$	$1.47^{+0.02}_{-0.01}$	34.30	244.22	0.16	$0.0277^{+0.0004}_{-0.0002}$	0.01	0.02	0.04
1.10	$1.32 \pm 0.02$	$1.424^{+0.014}_{-0.006}$	31.20	244.22	0.16	$0.0291^{+0.0004}_{-0.0002}$	0.01	0.02	0.04
1.15	$1.28 \pm 0.02$	$1.362^{+0.011}_{-0.009}$	26.19	244.22	0.17	$0.0286^{+0.0003}_{-0.0003}$	0.01	0.02	0.04
1.20	$1.25 \pm 0.02$	$1.363^{+0.009}_{-0.013}$	24.96	244.22	0.15	$0.0273^{+0.0004}_{-0.0004}$	0.01	0.02	0.04
1.25	$1.12 \pm 0.03$	$1.26^{+0.02}_{-0.02}$	20.02	244.22	0.13	$0.0254^{+0.0006}_{-0.0004}$	0.01	0.02	0.03
1.30	$1.14 \pm 0.02$	$1.1973^{+0.0068}_{-0.0006}$	17.42	244.22	$0.12^{+0.02}$	$0.0258^{+0.0004}_{-0.0002}$	0.01	0.02	0.03
1.35	$1.18 \pm 0.03$	$1.27^{+0.01}_{-0.03}$	17.71	244.22	$0.12^{+0.04}$	$0.0260^{+0.0004}_{-0.0009}$	0.01	0.02	$0.03^{+0.01}$
1.40	$1.19 \pm 0.02$	$1.1303^{+0.0007}_{-0.0092}$	13.80	244.22	0.14	$0.0272^{+0.0003}_{-0.0004}$	0.01	0.02	0.04

(continued on next page)

*(continued from previous page)*

E [EeV]	$p_E$	$\Delta N_{pE}$ [%]	$\chi_\phi^2$	$\chi_{\phi,\text{crit}}^2$	$\Delta E^{(\text{max})}$	$\Delta E^{(\text{mean})}$	$\Delta E^{(25\%)}$	$\Delta E^{(50\%)}$	$\Delta E^{(75\%)}$
1.45	$1.16 \pm 0.03$	$1.180^{+0.006}_{-0.010}$	14.48	244.22	0.14	$0.0267^{+0.0005}_{-0.0004}$	0.01	0.02	$0.040_{-0.010}$
1.50	$1.26 \pm 0.02$	$1.049^{+0.004}_{-0.002}$	11.91	244.22	$0.140^{+0.020}_{-0.010}$	$0.0286^{+0.0005}_{-0.0003}$	0.01	0.02	0.04
1.55	$1.30 \pm 0.02$	$1.12^{+0.02}_{-0.01}$	12.41	244.22	$0.150^{+0.010}$	$0.0282^{+0.0006}_{-0.0004}$	0.01	0.02	0.04
1.60	$1.32 \pm 0.03$	$1.246^{+0.015}_{-0.007}$	13.71	244.22	0.15	$0.0294^{+0.0006}_{-0.0004}$	0.01	0.02	0.04
1.65	$1.31 \pm 0.03$	$1.007^{+0.018}_{-0.005}$	10.26	244.22	0.12	$0.0299^{+0.0005}_{-0.0005}$	0.01	0.02	0.04
1.70	$1.24 \pm 0.02$	$1.005^{+0.005}_{-0.006}$	9.55	244.22	0.14	$0.0272^{+0.0003}_{-0.0006}$	0.01	0.02	0.04
1.75	$1.33 \pm 0.03$	$1.00^{+0.02}_{-0.01}$	9.79	244.22	$0.14_{-0.02}$	$0.0293^{+0.0008}_{-0.0007}$	0.01	0.02	0.04
1.80	$1.39 \pm 0.04$	$0.977^{+0.005}_{-0.001}$	8.99	244.22	0.15	$0.0304^{+0.0005}_{-0.0004}$	0.01	0.02	0.04
1.85	$1.37 \pm 0.03$	$1.005^{+0.021}_{-0.007}$	8.32	244.22	$0.15^{+0.03}$	$0.0300^{+0.0008}_{-0.0007}$	0.01	$0.020^{+0.010}$	0.04
1.90	$1.52 \pm 0.03$	$0.979^{+0.001}_{-0.016}$	8.09	244.22	0.16	$0.0337^{+0.0002}_{-0.0010}$	0.01	0.03	0.05
1.95	$1.35 \pm 0.04$	$0.960^{+0.022}_{-0.003}$	7.14	244.22	0.16	$0.0290^{+0.0009}_{-0.0008}$	0.01	0.02	0.04
2.00	$1.25 \pm 0.04$	$0.974^{+0.003}_{-0.003}$	6.83	244.22	0.15	$0.0274^{+0.0008}_{-0.0008}$	0.01	0.02	0.04
2.05	$1.31 \pm 0.04$	$0.770^{+0.029}_{-0.001}$	5.99	244.22	0.14	$0.0295^{+0.0005}_{-0.0009}$	0.01	0.02	0.04
2.10	$1.37 \pm 0.07$	$0.92^{+0.03}_{-0.03}$	6.62	244.22	$0.15_{-0.03}$	$0.031^{+0.001}_{-0.001}$	0.01	$0.030_{-0.010}$	0.04
2.15	$1.32 \pm 0.04$	$0.814^{+0.011}_{-0.010}$	5.86	244.22	$0.170_{-0.010}$	$0.029^{+0.001}_{-0.001}$	0.01	0.02	0.04
2.20	$1.18 \pm 0.05$	$0.82_{-0.01}$	5.30	244.22	$0.13_{-0.03}$	$0.0269^{+0.0010}_{-0.0011}$	0.01	0.02	$0.037^{+0.002}_{-0.007}$
2.25	$1.20 \pm 0.08$	$0.75^{+0.04}_{-0.03}$	4.51	244.22	$0.110^{+0.040}_{-0.010}$	$0.027^{+0.001}_{-0.001}$	0.01	0.02	$0.040_{-0.010}$
2.30	$1.40 \pm 0.05$	$0.877^{+0.006}_{-0.028}$	5.47	244.22	$0.140^{+0.010}$	$0.0301^{+0.0010}_{-0.0008}$	0.01	$0.020^{+0.010}$	0.04
2.35	$1.25 \pm 0.08$	$0.686^{+0.025}_{-0.002}$	4.29	244.22	$0.11^{+0.03}$	$0.0292^{+0.0017}_{-0.0007}$	0.01	0.02	0.04
2.40	$1.46 \pm 0.07$	$0.74^{+0.03}$	4.77	244.22	0.16	$0.031^{+0.001}_{-0.001}$	0.01	$0.02^{+0.01}$	0.04
2.45	$1.57 \pm 0.08$	$0.67^{+0.05}_{-0.02}$	5.57	244.22	$0.15^{+0.05}$	$0.033^{+0.002}_{-0.001}$	0.01	$0.030_{-0.010}$	0.05
2.50	$1.62 \pm 0.08$	$0.756^{+0.009}_{-0.031}$	4.99	244.22	$0.20_{-0.04}$	$0.036^{+0.001}_{-0.002}$	$0.020_{-0.010}$	0.03	0.05
2.55	$1.59 \pm 0.09$	$0.692^{+0.016}_{-0.009}$	4.63	244.22	$0.160^{+0.050}_{-0.010}$	$0.034^{+0.002}_{-0.002}$	0.01	$0.030_{-0.010}$	$0.050_{-0.010}$

*(continued on next page)*

(continued from previous page)

E [EeV]	$p_E$	$\Delta N_{p_E}$ [%]	$\chi_\phi^2$	$\chi_{\phi,\text{crit}}^2$	$\Delta E^{(\text{max})}$	$\Delta E^{(\text{mean})}$	$\Delta E^{(25\%)}$	$\Delta E^{(50\%)}$	$\Delta E^{(75\%)}$
2.60	$1.78 \pm 0.03$	$0.742^{+0.007}$	5.40	244.22	0.20	$0.0365^{+0.0009}_{-0.0007}$	0.01	0.03	0.05
2.65	$1.88 \pm 0.08$	$0.81^{+0.02}_{-0.03}$	5.55	244.22	$0.18^{+0.07}$	$0.040^{+0.002}_{-0.002}$	0.02	0.03	$0.060_{-0.010}$
2.95	$1.99 \pm 0.10$	$0.63^{+0.07}_{-0.05}$	4.62	244.22	0.18	$0.044^{+0.003}_{-0.002}$	0.02	$0.030^{+0.010}$	$0.060^{+0.010}$
3.00	$1.94 \pm 0.04$	$0.785^{+0.009}_{-0.016}$	4.50	244.22	$0.170^{+0.010}$	$0.0403^{+0.0015}_{-0.0009}$	0.02	0.03	$0.055^{+0.005}_{-0.005}$

**Table E.1.:** Results of the parameter determination for the correction procedure described in Section 5.2. For lower energy cuts E, ranging from 0.5 EeV to 3.0 EeV, the optimisation parameter  $p_E$  is determined such that the zenith angle distributions for two subsamples of the surface detector event set are compatible within the bounds of statistical uncertainty. For each value of the energy, the fraction of the events,  $\Delta N_{p_E}$ , lost due to the modulation of the lower energy cut, is calculated. In addition, the results of tests for side effects of the correction procedure are listed. The test statistic  $\chi_\phi^2$  characterises the compatibility of the azimuth angle distributions prior to and after applying the correction procedure; the corresponding critical region is defined by  $\chi_{\phi,\text{crit}}^2$ . The maximum energy undershoot caused by the correction procedure is denoted by  $\Delta E^{(\text{max})}$ , the mean undershoot by  $\Delta E^{(\text{mean})}$ . The quantities  $\Delta E^{(25\%)}$ ,  $\Delta E^{(50\%)}$  and  $\Delta E^{(75\%)}$  stand for the 25%, 50% and 75% quantiles of the energy undershoot, respectively. The values of the energy undershoot are in units of EeV. The uncertainties of the quantities are calculated by evaluating their values for  $p_E + \sigma_{p_E}$  and  $p_E - \sigma_{p_E}$ , respectively. If the value of a quantity for  $p_E + \sigma_{p_E}$  and  $p_E - \sigma_{p_E}$ , respectively, equals the one for  $p_E$ , then no error is given.





# Appendix F

## Li–Ma Significance

The *Li–Ma significance* is a measure for estimating positive observations of signals against a background [Gil04, Li83]. In case the background is estimated from measurements, the following expression yields a realistic estimation of the significance:

$$|S_{\text{LiMa}}| = \sqrt{2N_{\text{on}} \ln \frac{(1 + \alpha)N_{\text{on}}}{\alpha(N_{\text{on}} + N_{\text{off}})} + 2N_{\text{off}} \ln \frac{(1 + \alpha)N_{\text{off}}}{N_{\text{on}} + N_{\text{off}}}}. \quad (\text{F.1})$$

with

$$\alpha = \frac{\kappa_{\text{on}} \cdot t_{\text{on}} \cdot A_{\text{on}}}{\kappa_{\text{off}} \cdot t_{\text{off}} \cdot A_{\text{off}}}, \quad (\text{F.2})$$

where

- $\kappa_{\text{on}}, \kappa_{\text{off}}$  acceptance in *on* region and *off* region, respectively
- $t_{\text{on}}, t_{\text{off}}$  observation times
- $A_{\text{on}}, A_{\text{off}}$  size of the *on* region and *off* region, respectively
- $N_{\text{on}}, N_{\text{off}}$  number of events encountered in the *on* region and *off* region, respectively

Values for the Li–Ma significance and their associated uncertainties are listed in Tab. F.1 for different combinations of the numbers of events in the *on* and *off* cells, values of  $\alpha$  and the excess of events in the *on*.

$\alpha$	$N_{\text{on}}$	$N_{\text{off}}$	$\Delta N/N[\%]$	$S[\sigma]$	$\sigma_S[\sigma]$
1.0	20	20	1	0.0	1.0
1.0	21	20	5	0.2	1.0
1.0	22	20	10	0.3	1.0
1.0	202	200	1	0.1	1.0
1.0	210	200	5	0.5	1.0
1.0	220	200	10	1.0	1.0
1.0	2020	2000	1	0.3	1.0
1.0	2100	2000	5	1.6	1.0
1.0	2200	2000	10	3.1	1.0
0.2	20	100	1	0.0	0.9
0.2	21	100	5	0.2	0.9
0.2	22	100	10	0.4	0.9
0.2	202	1000	1	0.1	0.9
0.2	210	1000	5	0.6	0.9
0.2	220	1000	10	1.3	0.9
0.2	2020	10000	1	0.4	0.9
0.2	2100	10000	5	2.0	0.9
0.2	2200	10000	10	4.0	0.9
0.1	20	200	1	0.0	1.0
0.1	21	200	5	0.2	1.0
0.1	22	200	10	0.4	1.0
0.1	202	2000	1	0.1	1.0
0.1	210	2000	5	0.7	1.0
0.1	220	2000	10	1.3	1.0
0.1	2020	20000	1	0.4	1.0
0.1	2100	20000	5	2.1	1.0
0.1	2200	20000	10	4.2	1.0

**Table F.1.:** Values of the Li–Ma significance  $S$  for different values of the numbers of events in the *on* region, the *off* region, and the value of  $\alpha$ . The excess of events is denoted by  $\Delta N/N$ , the uncertainty of  $S$  is  $\sigma_S$ .

# List of Figures

2.1. Elemental composition of the cosmic radiation . . . . .	5
2.2. Sketch of an extensive air shower. . . . .	6
2.3. Hillas plot . . . . .	12
2.4. All-particle spectrum . . . . .	13
2.5. GZK horizon for protons . . . . .	16
3.1. Map of the southern observatory site . . . . .	20
3.2. Schematic view of an SD station . . . . .	21
3.3. Hierarchy of the SD trigger system . . . . .	22
3.4. T3 trigger configurations . . . . .	23
3.5. Charge and pulse height . . . . .	24
3.6. Schematic view of a typical FD building . . . . .	25
3.7. Schematic view of an FD telescope . . . . .	26
3.8. HEAT enhancement . . . . .	28
3.9. Layout of a typical AMIGA muon counter . . . . .	29
4.1. Climatic characteristics of the site . . . . .	33
4.2. Variation of density and temperature on a seasonal scale . . . . .	34
4.3. Weather stations on the Pierre Auger Observatory site . . . . .	35
4.4. Duty cycles of the weather stations . . . . .	36
4.5. Ambient temperatures recorded by Los Leones and the CLF . . . . .	37
4.6. Deviations of the air pressure recorded by Los Leones and the CLF . . . . .	38
4.7. Temperature vs. altitude, monthly profiles . . . . .	39
4.8. Air pressure vs. altitude, monthly profiles . . . . .	41
4.9. Validation of the ideal gas law approximation . . . . .	42
4.10. Correlation and deviation of SD PMT temperatures . . . . .	43
4.11. Residual uncertainty of the deconvoluted station temperature . . . . .	47
5.1. Aperture of the SD (Surface Detector) . . . . .	50
5.2. Air density vs. event rate . . . . .	51
5.3. Typical longitudinal air shower profile . . . . .	52
5.4. Typical lateral air shower profile . . . . .	54
5.5. Electromagnetic signal fraction . . . . .	55
5.6. First derivative of the energy spectrum . . . . .	59
5.7. Results of the $\chi^2$ maximisation . . . . .	60

*LIST OF FIGURES*

---

5.8. Zenith angle distributions for high and low temperatures . . . . .	61
5.9. Zenith angles vs. cumulative probability . . . . .	62
5.10. Parameter optimisation for $p_E$ . . . . .	66
5.11. Zenith angle distributions for high and low temperatures at $E = 0.5 \text{ EeV}$ , corrected . . . . .	67
5.12. Event loss and parameter $p_E$ versus lower energy limit . . . . .	68
5.13. Energy undershoot due to the correction . . . . .	68
5.14. Compatibility of azimuth angle distributions prior to and after compensation . . . . .	69
6.1. Magnetic field in the Milky Way, neutron decay . . . . .	72
6.2. Field of view vs. time of the day . . . . .	73
6.3. Variations of $\sec\Theta$ . . . . .	74
6.4. On–Off method . . . . .	75
6.5. Diurnal aperture variations . . . . .	76
6.6. Li–Ma significance distribution for isotropic data . . . . .	78
6.7. Isotropic datasets, corrections applied . . . . .	79
6.8. Anisotropic datasets . . . . .	80
6.9. Li–Ma significances around the GC . . . . .	81
6.10. Sky map of Li–Ma significances . . . . .	82
6.11. Results of a parameter scan around the Galactic Centre . . . . .	83
A.1. Energy loss due to the GZK suppression . . . . .	89
C.1. Pressure deviations between weather stations . . . . .	94
C.2. Correlation of pressure recorded by the weather stations . . . . .	95
C.3. Temperature deviations between weather stations . . . . .	96
C.4. Correlation of temperatures recorded by the weather stations . . . . .	97
C.5. Correlation of temperatures as recorded by the SD stations . . . . .	98
C.6. Correlation of temperatures as recorded by the SD stations (continued) . . . . .	99
C.7. Correlation of temperatures as recorded by the SD stations (continued) . . . . .	100
C.8. Temperature deviations between SD stations . . . . .	100
C.9. Temperature deviations between SD stations (continued) . . . . .	101
C.10. Temperature deviations between SD stations (continued) . . . . .	102
D.1. Reconstructed zenith angles for simulated air showers . . . . .	112
D.2. Reconstructed zenith angles for simulated air showers (continued) . . . . .	113
D.3. Reconstructed zenith angles for simulated air showers (continued) . . . . .	114
E.1. Zenith angle distributions for high and low temperatures, corrected . . . . .	116

# List of Tables

4.1. Coordinates of the weather stations . . . . .	37
4.2. Temperature gradients, fit results . . . . .	39
4.3. Air pressure gradients, fit results . . . . .	41
5.1. Results of the parameter fit of the expected event rate to the measured rate	57
5.2. Zenith angles and associated cumulative probabilities . . . . .	63
5.3. Energy ranges and mean zenith angle uncertainties . . . . .	64
5.4. Results of the parameter scan . . . . .	64
D.1. Zenith angle uncertainties for various energies and zenith angles . . . . .	104
D.2. Reconstructed zenith angles at $E_{MC} = 0.5 \text{ EeV}$ . . . . .	106
D.3. Reconstructed zenith angles at $1 \text{ EeV} \leq E_{MC} \leq 3 \text{ EeV}$ . . . . .	111
E.1. Results of the parameter determination . . . . .	119
F.1. Values of the Li–Ma significance . . . . .	122



# List of Acronyms

<b>AERA</b>	Auger Engineering Radio Array
<b>AGASA</b>	Akeno Giant Air Shower Array
<b>AGN</b>	Active Galactic Nucleus
<b>AIRES</b>	AIR-shower Extended Simulations
<b>AMIGA</b>	Auger Muon detectors and Infill for the Ground Array
<b>AST</b>	Argentina Standard Time
<b>ATIC</b>	Advanced Thin Ionization Calorimeter
<b>BLS</b>	Balloon Launch Station
<b>BSS</b>	Bi-Symmetric Spiral
<b>CDAS</b>	Central Data Acquisition System
<b>CIC</b>	Constant Intensity Cut
<b>CLF</b>	Central LASER Facility
<b>CMB</b>	Cosmic Microwave Background
<b>CNO</b>	Carbon–Nitrogen–Oxygen
<b>COBE</b>	Cosmic Background Explorer
<b>DFT</b>	Discrete Fourier Transform
<b>DLF</b>	Direct LASER Facility
<b>EAS</b>	Extensive Air Shower
<b>FADC</b>	Flash Analogue to Digital Converter
<b>FD</b>	Fluorescence Detector
<b>FFT</b>	Fast Fourier Transform

*LIST OF ACRONYMS*

---

<b>GAP</b>	Giant Array Project
<b>GPS</b>	Global Positioning System
<b>GRB</b>	Gamma Ray Burst
<b>GZK</b>	Greisen–Zatsepin–Kuz'min
<b>HEAT</b>	High Elevation Auger Telescopes
<b>HESS</b>	High Energy Stereoscopic System
<b>HiRes</b>	High Resolution Fly's Eye
<b>KASCADE</b>	Karlsruhe Shower Core and Array Detector
<b>KDE</b>	Kernel Density Estimate
<b>LASER</b>	Light Amplification by Stimulated Emission of Radiation
<b>LDF</b>	Lateral Distribution Function
<b>LHC</b>	Large Hadron Collider
<b>LIDAR</b>	Light Detection And Ranging
<b>LsId</b>	Local station Identification number
<b>MIA</b>	Michigan muon Array
<b>MC</b>	Monte Carlo
<b>NKG</b>	Nishimura–Kamata–Greisen
<b>PMT</b>	Photo Multiplier Tube
<b>PPF</b>	Percent Point Function
<b>QGSJET</b>	Quark–Gluon–String–Jet
<b>SD</b>	Surface Detector
<b>SUGAR</b>	Sydney University Giant Air shower Recorder
<b>TOT</b>	Time–Over–Threshold
<b>UHECR</b>	Ultra–High Energy Cosmic Rays
<b>UTC</b>	Coordinated Universal Time



*LIST OF ACRONYMS*

---

<b>UTM</b>	Universal Transverse Mercator
<b>VEM</b>	Vertical Equivalent Muon
<b>WMAP</b>	Wilkinson Microwave Anisotropy Probe
<b>XLF</b>	eXtreme LASER Facility



# Bibliography

- [Abb08] R. U. Abbasi et al., *First observation of the Greisen-Zatsepin-Kuzmin suppression*, Physical Review Letters **100** (2008), no. 10, 101101.
- [Abr08] J. Abraham et al. (Pierre Auger Collaboration), *Observation of the suppression of the flux of cosmic rays above  $4 \times 10^{19}$  eV*, Phys. Rev. Lett. **101** (2008), 061101, 0806.4302.
- [Abr09a] J. Abraham, P. Abreu, M. Aglietta, C. Aguirre, E. Ahn, D. Allard, I. Allekotte, J. Allen, J. Alvarez-Muñiz, M. Ambrosio, et al., *Trigger and Aperture of the Surface Detector Array of the Pierre Auger Observatory*, Nuclear Instruments and Methods in Physics Research Section A: Accelerators, Spectrometers, Detectors and Associated Equipment **613** (2009), no. 1.
- [Abr09b] J. Abraham et al. (The Pierre Auger Collaboration), *Atmospheric effects on extensive air showers observed with the Surface Detector of the Pierre Auger Observatory*, Astropart. Phys. **32** (2009), 89–99, 0906.5497.
- [Abr10a] J. Abraham, P. Abreu, M. Aglietta, C. Aguirre, E. J. Ahn, D. Allard, I. Allekotte, J. Allen, P. Allison, J. Alvarez-Muñiz, et al., *The fluorescence detector of the Pierre Auger Observatory*, submitted to Nuclear Instruments and Methods in Physics Research Section A: Accelerators, Spectrometers, Detectors and Associated Equipment (2010).
- [Abr10b] J. Abraham, P. Abreu, M. Aglietta, E. Ahn, D. Allard, I. Allekotte, J. Allen, J. Alvarez-Muñiz, M. Ambrosio, L. Anchordoqui, et al., *Measurement of the Depth of Maximum of Extensive Air Showers above  $10^{18}$  eV*, Physical review letters **104** (2010), no. 9.
- [Aha04] F. Aharonian, A. G. Akhperjanian, K. M. Aye, A. R. Bazer-Bachi, M. Beilicke, W. Benbow, D. Berge, P. Berghaus, K. Bernlöhr, O. Bolz, et al., *Very high energy gamma rays from the direction of Sagittarius A*, Astronomy and Astrophysics **425** (2004), no. 1, 13–17.
- [All88] I. Allekotte and H. Asorey, *Towards a complete set of weather data*, GAP-note 2007–088.

## BIBLIOGRAPHY

---

- [All08a] I. Allekotte, A. F. Barbosa, P. Bauleo, C. Bonifazi, B. Civit, C. O. Escobar, B. Garcia, G. Guedes, M. Gomez Berisso, J. L. Harton, et al., *The surface detector system of the Pierre Auger Observatory*, Nuclear Instruments and Methods in Physics Research Section A: Accelerators, Spectrometers, Detectors and Associated Equipment **586** (2008), no. 3, 409–420.
- [All08b] J. Allen et al., *The Pierre Auger Observatory Offline Software*, J. Phys. Conf. Ser. **119** (2008), 032002.
- [Ame08] M. Amenomori et al. (TIBET III Collaboration), *The all-particle spectrum of primary cosmic rays in the wide energy range from  $10^{14}$  eV to  $10^{17}$  eV observed with the Tibet-III air-shower array*, Astrophys. J. **678** (2008), 1165–1179, 0801.1803.
- [Ams08] C. Amsler et al. (Particle Data Group Collaboration), *Review of particle physics*, Phys. Lett. **B667** (2008), 1.
- [Ant05] T. Antoni et al. (The KASCADE Collaboration), *KASCADE measurements of energy spectra for elemental groups of cosmic rays: Results and open problems*, Astropart. Phys. **24** (2005), 1–25, astro-ph/0505413.
- [Arg07] S. Argiro, S. L. C. Barroso, J. Gonzalez, L. Nellen, T. Paul, T. A. Porter, L. Prado Jr., M. Roth, R. Ulrich, and D. Veberic, *The offline software framework of the Pierre Auger Observatory*, Nuclear Instruments and Methods in Physics Research Section A: Accelerators, Spectrometers, Detectors and Associated Equipment **580** (2007), no. 3, 1485–1496.
- [Arm74] M. L. Armitage, P. R. Blake, and W. F. Nash, *The mean lateral density distribution of muons in extensive air showers detected at Haverah Park*, Journal of Physics A: Mathematical, Nuclear and General **7** (1974), 2041–2051.
- [Ask65] G. A. Askaryan, *Coherent Radioemission from Cosmic Showers in the Air and Dense Media*, Zh. Eksperim. i Teor. Fiz **48** (1965).
- [Aug] *Search for First Harmonic Modulations in the Arrival Directions of Cosmic Rays Detected at the Pierre Auger Observatory*, preprint submitted to Elsevier.
- [Aug39] P. Auger, P. Ehrenfest, R. Maze, J. Daudin, and R. A. Fréon, *Extensive Cosmic-Ray Showers*, Rev. Mod. Phys. **11** (1939), 288–291.
- [AV09] J. Arteaga-Velázquez et al., *The Constant Intensity Cut Method applied to the KASCADE-Grande muon data*, Nuclear Physics B - Proceedings Supplements **196** (2009), 183–186.

## BIBLIOGRAPHY

---

- [AZ01] T. Abu-Zayyad et al. (HiRes-MIA Collaboration), *Measurement of the cosmic ray energy spectrum and composition from  $10^{17}$  eV to  $10^{18.3}$  eV using a hybrid fluorescence technique*, *Astrophys. J.* **557** (2001), 686–699, astro-ph/0010652.
- [Bar] *Bariloche weather files*,  
<http://particulas.cnea.gov.ar/experiments/auger/private/monit>.
- [Bel01] J. A. Bellido, R. W. Clay, B. R. Dawson, and M. Johnston-Hollitt, *Southern hemisphere observations of a  $10^{18}$  eV cosmic ray source near the direction of the Galactic Centre*, *Astroparticle Physics* **15** (2001), no. 2, 167–175.
- [Ben03] C. L. Bennett, M. Halpern, G. Hinshaw, N. Jarosik, A. Kogut, M. Limon, S. S. Meyer, L. Page, D. N. Spergel, G. S. Tucker, et al., *First-year Wilkinson Microwave Anisotropy Probe (WMAP) observations: preliminary maps and basic results*, *The Astrophysical Journal Supplement Series* **148** (2003), 1.
- [Ber99] E. G. Berezhko and L. T. Ksenofontov, *Composition of cosmic rays accelerated in supernova remnants*, *J. Exp. Theor. Phys.* **89** (1999), 391–403.
- [Ber06] X. Bertou, P. S. Allison, C. Bonifazi, P. Bauleo, C. M. Grunfeld, M. Aglietta, F. Arneodo, D. Barnhill, J. J. Beatty, et al., *Calibration of the Surface Array of the Pierre Auger Observatory*, *Nuclear Instruments and Methods in Physics Research Section A: Accelerators, Spectrometers, Detectors and Associated Equipment* **568** (2006), no. 2, 839–846.
- [Ber07] V. Berezhinsky, *Transition from galactic to extragalactic cosmic rays*, *Proceedings of 30th International Cosmic Ray Conference, Merida, Yucatan, Mexico* (2007), 0710.2750.
- [Bir94] D. J. Bird et al. (HIRES Collaboration), *The Cosmic ray energy spectrum observed by the Fly’s Eye*, *Astrophys. J.* **424** (1994), 491–502.
- [Bla59] R. B. Blackman and J. W. Tukey, *The Measurement of Power Spectra: From the Point of View of Communications Engineering*, Dover Publications New York, 1959.
- [Ble09] C. Bleve, *private communication*, 2009.
- [Blü09] J. Blümer, R. Engel, and J. R. Hörandel, *Cosmic rays from the knee to the highest energies*, *Progress in Particle and Nuclear Physics* **63** (2009), 293–338, 0904.0725.
- [Blü10] J. Blümer (Pierre Auger Collaboration), *The northern site of the Pierre Auger Observatory*, *New J. Phys.* **12** (2010), 035001.
- [Bon09] R. Bonino, *private communication*, 2009.

## BIBLIOGRAPHY

---

- [Can02] J. Candia, E. Roulet, and L. N. Epele, *Turbulent diffusion and drift in galactic magnetic fields and the explanation of the knee in the cosmic ray spectrum*, JHEP **12** (2002), 033, astro-ph/0206336.
- [Che86] K. S. Cheng, C. Ho, and M. Ruderman, *Energetic radiation from rapidly spinning pulsars. I- Outer magnetosphere gaps. II- VELA and Crab*, The Astrophysical Journal **300** (1986), 500.
- [Coo65] J. W. Cooley and J. W. Tukey, *An algorithm for the machine calculation of complex Fourier series*, Mathematics of computation **19** (1965), no. 90, 297–301.
- [Cro96] J. Cronin et al., *The Pierre Auger Project design report 2nd ed*, 1996, <http://www.auger.org>.
- [Dar08] A. Dar and A. De Rujula, *A theory of cosmic rays*, Phys. Rept. **466** (2008), 179–241, hep-ph/0606199.
- [Der05] V. A. Derbina et al. (RUNJOB Collaboration), *Cosmic-ray spectra and composition in the energy range of 10 TeV - 1000 TeV per particle obtained by the RUNJOB experiment*, Astrophys. J. **628** (2005), L41–L44.
- [Dru83] L. O. Drury, *An introduction to the theory of diffusive shock acceleration of energetic particles in tenuous plasmas*, Rept. Prog. Phys. **46** (1983), 973–1027.
- [Erl97] A. D. Erlykin and A. W. Wolfendale, *A single source of cosmic rays in the range  $10^{15}$  eV to  $10^{16}$  eV*, J. Phys. **G23** (1997), 979–989.
- [Fer49] E. Fermi, *On the Origin of the Cosmic Radiation*, Phys. Rev. **75** (1949), 1169–1174.
- [Fix96] D. J. Fixsen, E. S. Cheng, J. M. Gales, J. C. Mather, R. A. Shafer, and E. L. Wright, *The cosmic microwave background spectrum from the full COBE FIRAS data set*, The Astrophysical Journal **473** (1996), no. 2, 576–587.
- [Frö09] U. Fröhlich, *Charakterisierung der Szintillatoren und der Ausleseelektronik des AMIGA-Myonsystems*, Master’s thesis, University of Siegen, 2009.
- [Gai78] T. K. Gaisser and A. Hillas, *Reliability of the method of constant intensity cuts for reconstructing the average development of vertical showers (of cosmic rays)*, International Cosmic Ray Conference, 15th, Plovdiv, Bulgaria, 1978, pp. 353–357.
- [Gai91] T. K. Gaisser, *Cosmic Rays and Particle Physics*, Cambridge University Press, 1991.

## BIBLIOGRAPHY

---

- [Gai95] T. K. Gaisser, F. Halzen, and T. Stanev, *Particle astrophysics with high-energy neutrinos*, Phys. Rept. **258** (1995), 173–236, hep-ph/9410384.
- [GCG78] *A Prescription for A Search for An Excess of Cosmic Rays at EeV Energies towards the Galactic Center with the Pierre Auger Observatory*, The Galactic Center Group - Point Sources task, GAP-note 2008–178.
- [Gil04] S. Gillessen and H. L. Harney, *Significance in gamma-ray astronomy - the Li & Ma problem in Bayesian statistics*, Tech. Report astro-ph/0411660, MPG, Nov 2004.
- [Gre56] K. Greisen, *The extensive air showers*, Progress in Elementary Particle and Cosmic Ray Physics **3** (1956), 1–141.
- [Gre66] K. Greisen, *End to the Cosmic-Ray Spectrum?*, Phys. Rev. **16** (1966), 748–750.
- [Gri70] N.L. Grigorov, V. E. Nesterov, I. D. Rapoport, I. A. Savenko, and G. A. Skuridin, *Investigation of energy spectrum of primary cosmic particles with high and superhigh energies of space stations \*Proton\**, Yad. Fiz. **11** (1970), 1058–1069.
- [Gru05] C. Grupen, *Astroparticle physics*, Springer Verlag, 2005.
- [Hau04] A. Haungs et al. (KASCADE Collaboration), *Astrophysics of the knee in the cosmic ray energy spectrum*, Acta Phys. Polon. **B35** (2004), 331–339.
- [Hay99] N. Hayashida, M. Nagano, D. Nishikawa, H. Ohoka, N. Sakaki, M. Sasaki, M. Takeda, M. Teshima, R. Torii, T. Yamamoto, et al., *The anisotropy of cosmic ray arrival directions around  $10^{18}$  eV*, Astroparticle Physics **10** (1999), no. 4, 303–311.
- [Hec03] N. A. Heckert and J. Filliben, *NIST Handbook 148: DATAPLOT Reference Manual*, National Institute of Standards and Technology Handbook Series (2003).
- [Hes12] V. F. Hess, *Über Beobachtungen der durchdringenden Strahlung bei sieben Freiballonfahrten*, Phys. Z. **13** (1912), 1084–1091.
- [Hör03] J. R. Hörandel, *On the knee in the energy spectrum of cosmic rays*, Astropart. Phys. **19** (2003), 193–220, astro-ph/0210453.
- [ICR03] ICRC, *ATIC experiment: Preliminary results from the flight in 2002*, 2003, prepared for 28th International Cosmic Ray Conferences (ICRC 2003), Tsukuba, Japan, 31 Jul - 7 Aug 2003.

## BIBLIOGRAPHY

---

- [ICR07] ICRC, *Test of hadronic interaction models with data from the Pierre Auger Observatory*, 2007, presented at 30th International Cosmic Ray Conference (ICRC 2007), Merida, Yucatan, Mexico, 3-11 Jul 2007.
- [ICR09a] ICRC, *Calibration and Monitoring of the Pierre Auger Observatory*, 2009.
- [ICR09b] ICRC, *The Cosmic Ray Energy Spectrum and Related Measurements with the Pierre Auger Observatory*, 2009.
- [Jam98] F. James, *MINUIT-Function Minimization and Error Analysis-Reference Manual Version 94.1*, CERN Program Library Long Writeup D **506** (1998).
- [Kam58] K. Kamata and J. Nishimura, *The lateral and the angular structure functions of electron showers*, Prog. Theoret. Phys. Suppl **6** (1958), 93–155.
- [Kam04] K. H. Kampert et al. (KASCADE-Grande Collaboration), *Cosmic rays in the 'knee'-region: Recent results from KASCADE*, Acta Phys. Polon. **B35** (2004), 1799–1812, astro-ph/0405608.
- [Kan81] E. R. Kanasewich, *Time Sequence Analysis in Geophysics*, University of Alberta Press, 1981.
- [Kaz01] D. Kazanas and A. Nicolaidis, *Cosmic Ray "Knee": A Herald of New Physics?*, International Cosmic Ray Conference, International Cosmic Ray Conference, vol. 5, 2001, pp. 1760–+.
- [Kei09] B. G. Keilhauer, H. O. Klages, and M. Risse, *Results of the first balloon measurements above the Pampa Amarilla*, GAP-note 2003–009.
- [Kei21] B. G. Keilhauer, B. Wilczynska, and H. Wilczynski, *Molecular Atmosphere Profiles for Malargüe*, GAP-note 2005–021.
- [Kei37] B. G. Keilhauer, B. Wilczynska, H. Wilczynski, R. Engel, and M. Will, *New Malargüe Monthly Models*, GAP-note 2009–037.
- [Kei03] B. G. Keilhauer, *Investigation of Atmospheric Effects on the Development of Extensive Air Showers and their Detection with the Pierre Auger Observatory*, Ph.D. thesis, University of Karlsruhe, 2003.
- [Kob02] K. Kobayakawa, Y. Sato, and T. Samura, *Acceleration of particles by oblique shocks and cosmic ray spectra around the knee region*, Phys. Rev. **D66** (2002), 083004, astro-ph/0008209.
- [Law91] M. Lawrence, R. Reid, and A. Watson, *The cosmic ray energy spectrum above  $4 \cdot 10^{17}$  eV as measured by the Haverah Park array*, Journal of Physics G: Nuclear and Particle Physics **17** (1991), 733.



## BIBLIOGRAPHY

---

- [Li83] T. Li and Y. Ma, *Analysis methods for results in gamma-ray astronomy*, *ApJ* **272** (1983), 317.
- [Lin63a] J. Linsley, *Evidence for a Primary Cosmic-Ray Particle with Energy  $10^{20}$  eV*, *Phys. Rev. Lett.* **10** (1963), no. 4, 146–148.
- [Lin63b] J. Linsley, *Primary cosmic rays of energy  $10^{17}$  to  $10^{20}$  eV, the energy spectrum and arrival directions*, International Cosmic Ray Conference, International Cosmic Ray Conference, vol. 4, 1963, pp. 77–+.
- [Lod03] K. Lodder, *Solar System Abundances and Condensation Temperatures of the Elements*, *Astrophys. J.* **591** (2003), 1220–1247.
- [Mil07] M. Milgrom and V. Usov, *Possible association of ultra-high-energy cosmic-ray events with strong gamma-ray bursts*, *Astrophys. J.* (2007).
- [Müc99] A. Mücke, J. P. Rachen, R. Engel, R. J. Protheroe, and T. Stanev, *Photohadronic processes in astrophysical environments*, *PUBLICATIONS-ASTRONOMICAL SOCIETY OF AUSTRALIA* **16** (1999), 160–166.
- [Ost06] S. Ostapchenko, *QGSJET-II: towards reliable description of very high energy hadronic interactions*, *Nuclear Physics B-Proceedings Supplements* **151** (2006), no. 1, 143–146.
- [Pre07] W. H. Press, S. A. Teukolsky, W. T. Vetterling, and B. P. Flannery, *Numerical Recipes: The Art of Scientific Computing*, third ed., Cambridge Univ. Press, 2007.
- [Ptu93] V. S. Ptuskin, S. I. Rogovaya, V. N. Zirakashvili, L. G. Chuvilgin, G. B. Khristiansen, E. G. Klepach, and G. V. Kulikov, *Diffusion and drift of very high energy cosmic rays in galactic magnetic fields*, *aap* **268** (1993), 726–735.
- [Ptu09] V. S. Ptuskin, S. I. Rogovaya, and V. N. Zirakashvili, *Acceleration of ultra-high energy cosmic rays by galaxy cluster accretion shocks*, *Bulletin of the Russian Academy of Sciences: Physics* **73** (2009), no. 5, 552–554.
- [Rac93] J. P. Rachen and P. L. Biermann, *Extragalactic ultrahigh-energy cosmic rays. 1. Contribution from hot spots in FR-II radio galaxies*, *Astron. Astrophys.* **272** (1993), 161–175, astro-ph/9301010.
- [Rac96] J. Rachen, *Interaction processes and statistical properties of the propagation of cosmic rays in photon backgrounds*, Ph.D. thesis, Universität Bonn, 1996.
- [Rap02] C. Rappaport, *A color map for effective black-and-white rendering of color-scale images*, *IEEE Antennas and Propagation Magazine* **44** (2002), no. 3, 94–96.

## BIBLIOGRAPHY

---

- [San08] E. M. Santos, C. Bonifazi, and A. Letessier-Selvon, *Estimating a cosmic ray detector exposure sky map under the hypothesis of seasonal and diurnal effects factorization*, *Astroparticle Physics* **30** (2008), no. 1, 39–44.
- [Sch28] V. Scherini, *Study of the performance of the Pierre Auger Observatory and search for primary cosmic ray photons*, GAP-note 2007–128.
- [Sci99] S. J. Sciutto, *AIRES: A system for air shower simulations*, Universidad Nacional de la Plata, La Plata (1999).
- [Sig03] G. Sigl, *The enigma of the highest energy particles of nature*, *Ann. Phys.* **303** (2003), 117–141, astro-ph/0210049.
- [Sil98] B. W. Silverman, *Density estimation for statistics and data analysis*, Chapman & Hall/CRC, 1998.
- [Sim83] J. A. Simpson, *Elemental and Isotopic Composition of the Galactic Cosmic Rays*, *Annual Review of Nuclear and Particle Science* **33** (1983), 323–382.
- [Smi97] S. W. Smith et al., *The scientist and engineer’s guide to digital signal processing*, second ed., California Technical Pub, 1997.
- [Sny97] J. Snyder, *Flattening the Earth: two thousand years of map projections*, University of Chicago Press, 1997.
- [Sof86] Y. Sofue, M. Fujimoto, and R. Wielebinski, *Global structure of magnetic fields in spiral galaxies*, *Annual Review of Astronomy and Astrophysics* **24** (1986), no. 1, 459–497.
- [Sta93] T. Stanev, P. L. Biermann, and T. K. Gaisser, *Cosmic rays. 4. The Spectrum and chemical composition above  $10^4$  GeV*, astro-ph/9303006.
- [Ste73] F. W. Stecker, *Ultrahigh energy photons, electrons and neutrinos, the microwave background, and the universal cosmic ray hypothesis*, *Astrophys. Space Sci.* **20** (1973), 47–57.
- [Ste99] F. W. Stecker and M. H. Salamon, *Photodisintegration of Ultra-High-Energy Cosmic Rays: A New Determination*, *The Astrophysical Journal* **512** (1999), 521–526.
- [Sup08] A. D. Supanitsky et al., *Underground Muon Counters as a Tool for Composition Analyses*, *Astropart. Phys.* **29** (2008), 461–470, 0804.1068.
- [vdB65] A. M. van den Berg, J. Coppens, S. Harmsma, S. de Jong, M. Leuthold, and C. Timmermans, *First detection of radio signals from cosmic rays at the Pierre Auger Observatory*, GAP-note 2007–065.

## BIBLIOGRAPHY

---

- [Wie09] L. Wiencke and for the Pierre Auger Collaboration, *Atmospheric Calorimetry above  $10^{19}$  eV: Shooting Lasers at the Pierre Auger Cosmic-Ray Observatory*, J. Phys. Conf. Ser. **160** (2009), 012037, 0807.2884.
- [Wig00] R. Wigmans, *On big bang relics, the neutrino mass and the spectrum of cosmic rays*, Nucl. Phys. Proc. Suppl. **85** (2000), 305–310, hep-ph/0107263.
- [Wil81] M. Will, *Influence of Humidity on the Development and Reconstruction of Extensive Air Showers at the Pierre Auger Observatory*, GAP-note 2009–081.
- [Wil08] B. Wilczynska, R. Engel, P. Homola, et al., *Variation of the shower lateral spread with air temperature at the ground*, International Cosmic Ray Conference, vol. 4, 2008, pp. 369–372.
- [Zat66] G. T. Zatsepin and V. A. Kuz'min, *Upper Limit of the Spectrum of Cosmic Rays*, Soviet Journal of Experimental and Theoretical Physics Letters **4** (1966), 78–+.
- [Zey06] C. Zey et al., *e-Handbook of Statistical Methods*, NIST/SEMATECH, <http://www.itl.nist.gov/div898/handbook>, 2006.
- [Zha09] J. Zhang, *Nonparametric Density Estimation*, 2009.





